

## Durham E-Theses

---

### *Seismic penetration problem in the Wadi field, Sirte basin, Libya*

Uheida, Ibrahim Mabrok

#### How to cite:

---

Uheida, Ibrahim Mabrok (1999) *Seismic penetration problem in the Wadi field, Sirte basin, Libya*, Durham theses, Durham University. Available at Durham E-Theses Online:  
<http://etheses.dur.ac.uk/4551/>

#### Use policy

---

The full-text may be used and/or reproduced, and given to third parties in any format or medium, without prior permission or charge, for personal research or study, educational, or not-for-profit purposes provided that:

- a full bibliographic reference is made to the original source
- a [link](#) is made to the metadata record in Durham E-Theses
- the full-text is not changed in any way

The full-text must not be sold in any format or medium without the formal permission of the copyright holders.

Please consult the [full Durham E-Theses policy](#) for further details.

**Seismic Penetration Problem in the Wadi  
Field, Sirte Basin, Libya**

by

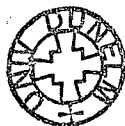
**Ibrahim Mabrok Uheida**

**Department of Geological Sciences**

**University of Durham**

The copyright of this thesis rests with the author. No quotation from it should be published without the written consent of the author and information derived from it should be acknowledged.

A thesis submitted in partial fulfilment of the requirements for  
the degree of Master of Science



11 MAY 1999

January 1999

## Abstract

The Wadi Field is located within the north central part of the Sirte basin, Libya. Over the past few years, Sirte Oil Company of Libya has acquired several seismic surveys in this area. The latest survey was an experimental line shot in 1995, with five heavy vibrators sweeping over the bandwidth 8-40 Hz and 720 recording channels. The objective was to obtain interpretable information beneath the top Upper Cretaceous horizon (top Kalash) which is generally the lowest horizon visible on the processed seismic sections. The primary exploration target is the Nubian formation within the Lower Cretaceous.

The acquired dataset was processed by CGG in 1996, and subsequently reprocessed by me as part of this project. Some improvement in the static corrections is evident in the reprocessed data, but neither processing sequence was successful in delineating the oil-bearing structure within the Lower Cretaceous. The rest of the project was an investigation into the reasons for the lack of signal penetration beneath the top Kalash horizon.

Synthetic seismograms were generated using sonic log data from well D7-NC149 to understand the effects of the primary reflectivity, transmissivity, and multiples on the primary reflection events in general, and on signal returns from the target horizon in particular. The behaviour of the reflectivity at the top Kalash and the top Nubian horizons and the transmission losses within the geological sequence overlying these horizons were examined in both time and frequency domains. Spectral analysis was conducted for 64-sample windows around the two-way travel times of both horizons in order to understand the effect of each factor separately.



The results indicate that the lack of clear signal from the top Nubian is partly due to the weak primary reflectivity at that horizon, and only slightly due to transmission effects. However, the primary reflectivity is relatively strong at frequencies up to 25 Hz. Since anelastic attenuation increases with frequency, use of higher frequencies in the conventional bandwidth is a waste of effort. Therefore it is necessary to use a seismic source which generates more signal energy than previously used at frequencies below 25 Hz, so I recommend the use of more vibrator sweeps over the bandwidth 5-25 Hz.

It is also shown that the relative reduction in amplitudes between top Kalash and top Nubian caused by geometric spreading and anelastic effects within the Upper Cretaceous is significant.

The combined effects of transmission losses, reflectivity at each horizon, geometric spreading and anelastic attenuation are estimated to give a relative reduction in signal amplitude of -12 dB at 25 Hz. Therefore at least four times as much source effort is required than previously used, and should be applied over the recommended bandwidth of 5-25 Hz.

# Contents

|                                                               |           |
|---------------------------------------------------------------|-----------|
| <b>Abstract</b>                                               | <b>1</b>  |
| <b>Acknowledgements</b>                                       | <b>9</b>  |
| <b>Chapter 1 Introduction</b>                                 | <b>10</b> |
| 1.1 Project background                                        | 10        |
| 1.2 Acquisition parameters for the Vibroseis data sets        | 12        |
| 1.3 Aims of the project                                       | 14        |
| <b>Chapter 2 Geology of the Wadi field</b>                    | <b>17</b> |
| 2.1 Introduction                                              | 17        |
| 2.2 Wadi palaeo-high structure evolution                      | 18        |
| 2.3 Lithologic summary of the Wadi Field sedimentary sequence | 18        |
| <b>Chapter 3 Reprocessing of the 1995 experimental line</b>   | <b>23</b> |
| 3.1 Introduction                                              | 23        |
| 3.2 Geometry information                                      | 25        |
| 3.3 Downloading of field data                                 | 25        |
| 3.3.1 SE G-Y input                                            | 25        |
| 3.3.2 Trace renumbering                                       | 26        |
| 3.3.3 Geometry assignment                                     | 26        |
| 3.3.4 Database header transfer                                | 26        |
| 3.3.5 Trace editing                                           | 26        |
| 3.4 True amplitude recovery, statics, and trace muting        | 28        |
| 3.4.1 True amplitude recovery                                 | 28        |
| 3.4.2 Static corrections                                      | 28        |
| 3.4.3 Trace muting                                            | 31        |

|                                                                  |                                                                                |           |
|------------------------------------------------------------------|--------------------------------------------------------------------------------|-----------|
| 3.5                                                              | <i>F-K</i> Filtering .....                                                     | 32        |
| 3.6                                                              | Prestack deconvolution .....                                                   | 36        |
| 3.7                                                              | Common midpoint sorting .....                                                  | 37        |
| 3.8                                                              | Constant velocity stack .....                                                  | 37        |
| 3.9                                                              | Residual statics .....                                                         | 40        |
| 3.10                                                             | Normal moveout corrections, trace muting, and stacking .....                   | 44        |
| 3.11                                                             | Summary .....                                                                  | 47        |
| <br><b>Chapter 4 One-dimensional synthetic seismograms .....</b> |                                                                                | <b>51</b> |
| 4.1                                                              | Introduction .....                                                             | 51        |
| 4.2                                                              | Derivation of the polynomial equations using the layer-matrix .....            | 53        |
| 4.3                                                              | Well data available .....                                                      | 63        |
| 4.4                                                              | Computing reflection coefficients from sonic log .....                         | 64        |
| 4.5                                                              | Seismic source wavelet .....                                                   | 67        |
| 4.6                                                              | Synthetic seismograms .....                                                    | 67        |
| 4.6.1                                                            | Synthetic seismogram without multiples and transmission losses ..              | 67        |
| 4.6.2                                                            | Synthetic seismogram with primaries and transmission losses .....              | 69        |
| 4.6.3                                                            | Synthetic seismogram with multiples and transmission losses .....              | 69        |
| 4.6.4                                                            | Synthetic seismograms with near-surface included .....                         | 71        |
| 4.7                                                              | Results and discussion .....                                                   | 74        |
| 4.7.1                                                            | Effects of transmission losses and multiples .....                             | 74        |
| 4.7.2                                                            | Investigations using the conventional seismic bandwidth .....                  | 77        |
| 4.7.3                                                            | Investigations using lower frequencies .....                                   | 82        |
| 4.7.4                                                            | Analysis in the frequency domain .....                                         | 82        |
| 4.7.5                                                            | Geometric spreading and absorption losses within the Upper<br>Cretaceous ..... | 92        |

|                   |                                                                     |            |
|-------------------|---------------------------------------------------------------------|------------|
| 4.7.6             | Effect of free-surface on the reflected data .....                  | 93         |
| 4.7.7             | Comparison of the real data with the primaries-only synthetic ..... | 98         |
| 4.8               | Summary .....                                                       | 102        |
| <b>Chapter 5</b>  | <b>Conclusions and suggestions for further work .....</b>           | <b>104</b> |
| <b>Chapter 6</b>  | <b>References .....</b>                                             | <b>107</b> |
| <b>Appendix A</b> | <b>Fortran program listings .....</b>                               | <b>110</b> |
| A1                | Synthetic seismograms without free-surface program .....            | 111        |
| A2                | Complete synthetic seismograms with free-surface program .....      | 117        |
| A3                | Program to convert ASCII data into binary data .....                | 120        |
| A4                | Program to convert binary data into SEG-Y format data .....         | 120        |
| A5                | Fourier analysis program .....                                      | 121        |

## Figures and Tables

- Figure 1.1 Location map
- Figure 1.2 Raw common-shot gather
- Figure 1.3 Shooting geometry
- 
- Figure 2.1 Lithologic log
- 
- Figure 3.1 Number of recording channels and fold of cover
- Figure 3.2 Common-shot gather with edited noisy traces
- Figure 3.3 Up-holes cross-section
- Figure 3.4 Common-shot gather with true amplitude recovery
- Figure 3.5a  $F$ - $K$  amplitude spectra
- Figure 3.5b Common-shot gather with velocity filtering
- Figure 3.6 Common-shot gather with velocity filtering and predictive deconvolution
- Figure 3.7 Common midpoint gather sorted after application of velocity filtering and predictive deconvolution
- Figure 3.8 Constant velocity stacks
- Figure 3.9 Summary of residual statics
- Figure 3.10 Correlation coefficient values
- Figure 3.11 Processing flow-chart
- Figure 3.12 Common midpoint gather sorted before application of velocity filtering and predictive deconvolution
- 
- Figure 4.1 Common midpoint stack from the experimental line
- Figure 4.2 Primary reflection coefficient series

- Figure 4.3 Primary reflection coefficients with two-way transmission losses
- Figure 4.4 Earth's impulse response
- Figure 4.5 The amplitude spectrum of the sweep (8-40 Hz) and its auto-correlation
- Figure 4.6 Reflection and transmission across interface  $k$
- Figure 4.7 Downgoing and upgoing wavefields in a layered medium
- Figure 4.8 Reflection and transmission seismic waves in a layered medium  
confined between two half spaces
- Figure 4.9 Sonic log
- Figure 4.10 Primaries-only synthetic seismogram
- Figure 4.11 Synthetic seismogram with primaries and transmission losses
- Figure 4.12 First-order multiple reflections
- Figure 4.13 Complete synthetic seismogram
- Figure 4.14 Simple depth model of the weathering zone
- Figure 4.15 Composite plot shows effect of multiples on the primaries
- Figure 4.16 Primaries from top Kalash with the associated peg-leg multiples
- Figure 4.17 Composite plot shows the effect of the long-period multiples on the  
primaries from top Kalash
- Figure 4.18 Primaries from top Nubian with the associated peg-leg multiples
- Figure 4.19 Composite plot shows the effect of the long-period multiples of the  
primary from top Nubian
- Figure 4.20 Primaries from top Nubian with the associated multiples (low  
Frequency bandwidth)
- Figure 4.21 The amplitude spectrum of the sweep (5-20 Hz) and its auto-correlation
- Figure 4.22 Primary reflections from top Kalash and top Nubian
- Figure 4.23 Composite reflection impulse responses from top Kalash and top  
Nubian with transmission losses included

Figure 4.24 Amplitude spectra of the reflection events in Figure 4.23

Figure 4.25 Reflection complexes from the isolated reflector at 3200 ms

Figure 4.26 Amplitude spectra of the reflection complexes in Figure 4.25

Figure 4.27 Amplitude reduction due to absorption losses

Figure 4.28 Primaries alone and complete seismograms with near-surface included

Figure 4.29 Truncated seismograms showing effect of near-surface

Figure 4.30 Comparison of real data with synthetic data

Figure 4.31 Comparison of low and high frequency seismograms

Table 3.1 Weathering and subweathering information used in computing the static corrections

## **Acknowledgements**

I am most grateful to my supervisor, Dr Neil Gouly, for his helpful guidance and endless patience throughout the course of this project and for improving my knowledge of the English language.

I wish to thank all the academic staff, support staff and postgraduates in the department, in particular Mr Dave Stevenson, Mr Ian Turner, Mr Duncan Stock and Mrs Karen Atkinson, for their help with computing and plotting the results.

I am particularly grateful to the Sirte Oil Company Committee for Production and Manufacturing of Oil and Gas, especially the exploration management, for their sponsorship and for kindly releasing the data which forms the foundation of this work.

Thanks also to the staff in the training department of Sirte Oil Company and the training department of Al-Jawaby Oil Services for their undiminished support.

I would like to express my sincere thanks to Mr Fathi Ghrouda, Mr Abdalbasset Rafee, Mr Ron Harbinson and Mr Hazim Al-Dabagh in the exploration department of Sirte Oil Company for providing the data that I needed.

Finally, and above all, I am very grateful to my parents, my wife and our two daughters, and my brothers and sisters for helping me to overcome the inevitable homesickness, and for their encouragement and generous support through a difficult time for me.

# CHAPTER ONE

## Introduction

### 1.1 Project Background

Development of the Wadi Field began in the early 1980s, and has been hampered from the outset by the lack of interpretable seismic data beneath the top Kalash (top Upper Cretaceous) horizon. The primary exploration target (Nubian formation) lies within the Lower Cretaceous. As a result, several attempts have been made in recent years by Sirte Oil Company of Libya to enhance the data quality from the top Nubian horizon by conducting different seismic surveys with substantially different acquisition parameters and equipment. The latest of these surveys was an experimental line (149V1211-95) acquired in 1995. In addition to the acquisition, a considerable amount of effort has also been given to the processing of the various data vintages.

The initial objective of the 1995 experimental line was to improve the signal to noise ratio of the seismic reflection data from the Lower Cretaceous, particularly the top Nubian. The line is 20 km long, is orientated east-west in a direction almost perpendicular to the major fault trend (Figure 1.1), and passes 55 m to the south of well D7-NC149. It was recorded with 720 channels, a symmetrical spread with 20 m source and receiver group intervals, and five heavy vibrators. The data were originally processed by CGG, and subsequently reprocessed by me using the ProMAX workstation at Durham University. Unfortunately, after all the efforts including the high costs of acquisition, the processing outcomes have still failed to image the structure below the Upper Cretaceous. It should be borne in mind that this result is no worse than what was achieved from the previous surveys, with the top Kalash horizon effectively

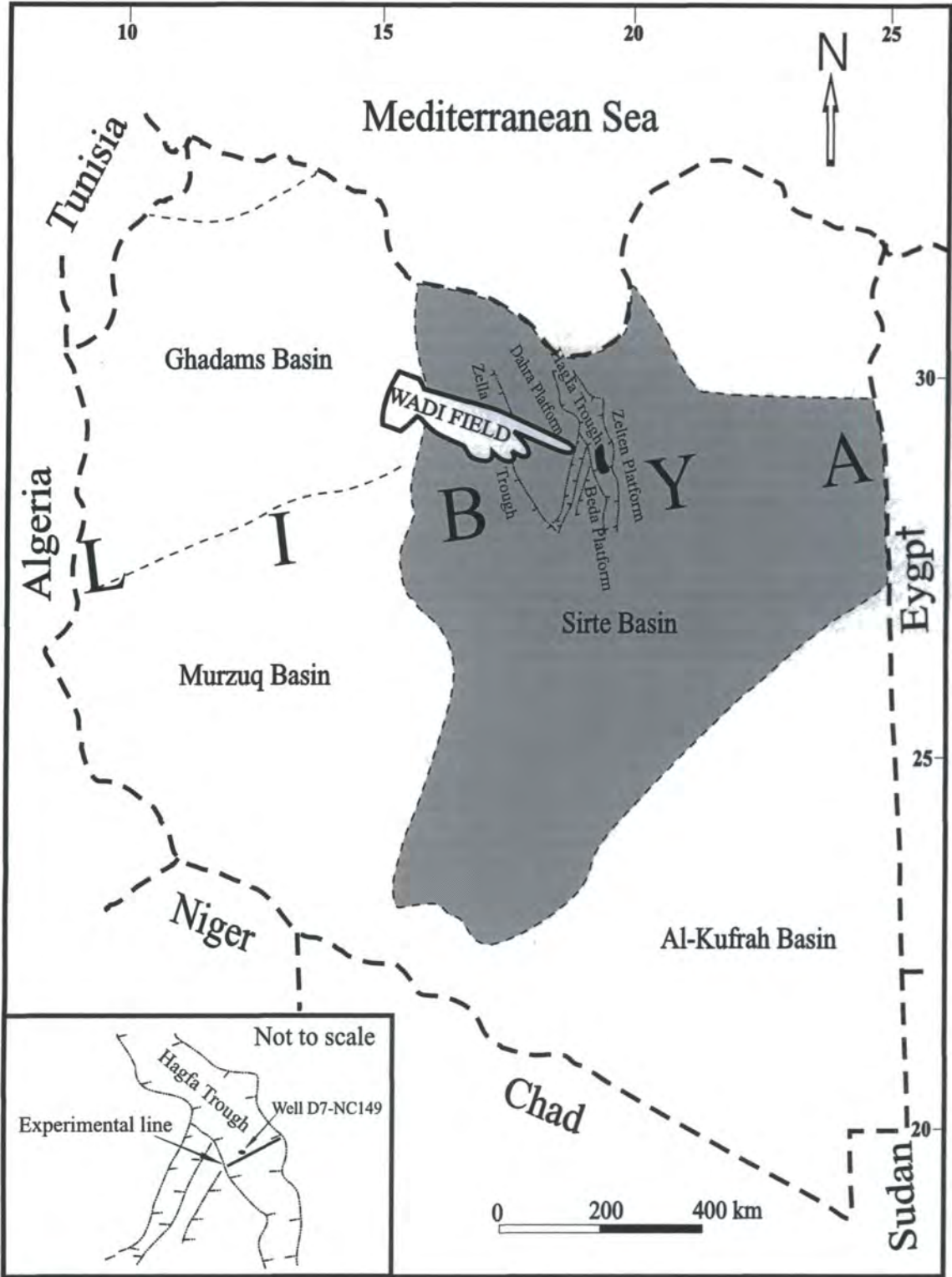


**Figure 1.1.** A map of Libya showing the location of the Wadi Field and the major faults at the top Cretaceous horizon in that part of the Sirte Basin. The location of the experimental line is shown in the left bottom corner.

being the seismic basement.

Figure 1.2 is a common source gather from the experimental line which shows how badly the raw data are dominated by reverberant refracted arrivals, dispersed ground roll and some air waves, with an absence of clear reflection events at all levels.

## **1.2 Acquisition parameters for the Vibroseis data sets**

In 1985, Sirte Oil acquired a total of 234 km Vibroseis data in the Wadi area. As a matter of fact, the history of seismic acquisition in this area stretches further back to the early days of 1971, when a total of 85 km Dinoseis data with 24-fold coverage were acquired in the same region by a different client.

A split-spread geometry comprising 96 receiver stations was used, with 50 m source and receiver group intervals. Each receiver group consisted of 48 geophones with a regular geophone spacing of 6.8 m between the individual 10 Hz geophones. The data were recorded for 14 s record length (uncorrelated) with a sampling interval of 4 ms. An anti-alias filter was applied at 62.5 Hz. The source was four vibrators; each emitting eight linear upsweeps of 10 s length and a frequency bandwidth of 8–48 Hz with a cosine taper of 250 ms applied at both ends of the sweep. A 10 Hz low-cut filter was applied later in the processing.

During 1988, a different approach was tried: the subsurface coverage per common mid point (CMP) was increased to 120-fold by using an off-end spread of 240 recording channels, with source and receiver group intervals of 16.7 m and 12 geophones per group. The source power was also increased by using six vibrators with 27,240 pounds theoretical peak force per vibrator. A total of 85 km, 4 s correlated data were recorded on nine track ½ inch magnetic tapes. The recording filter settings were 10 Hz and 62.5

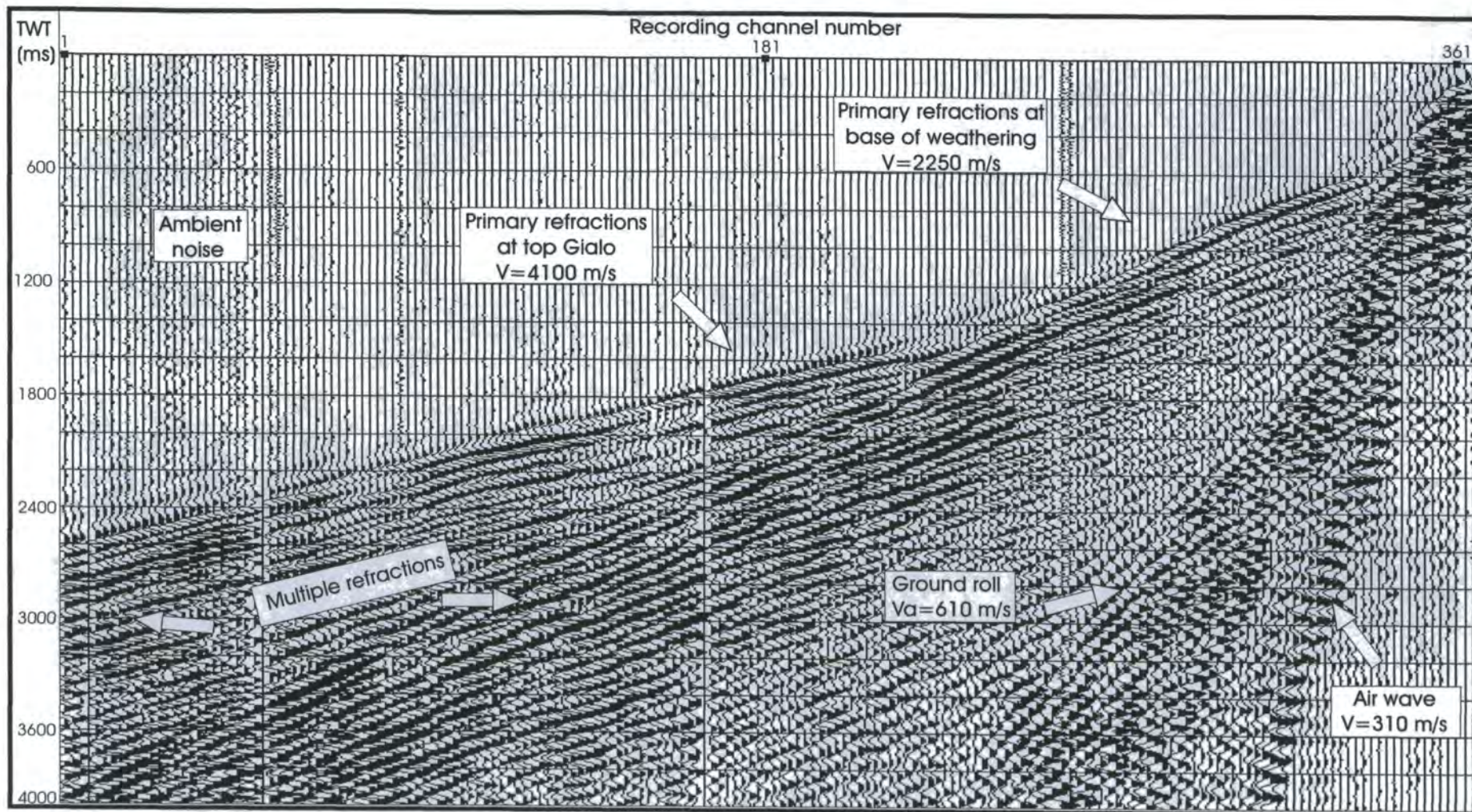


**Figure 1.2.** A raw shot gather dominated with reverberant refracted arrivals which characterized by its strong amplitude, and dispersive ground roll. Additionally, the record contains some high frequency air waves. For display purposes, only half of the record with every second trace and 4.0 s two-way travel time is shown.

Hz for the low-cut and the high-cut filters, respectively. The six source units were shaking simultaneously; each generated 3 linear upsweeps per station over a period of 12 s and a frequency band of 10 – 65 Hz.

With the advent of large vibrators and the advanced vibrator electronics with Sercel 368 recording instruments, Sirte deemed it worthwhile in 1995 to carry out a test line in the same region with some control from the previous surveys. The test line was recorded with five vibrators of 60,000 pounds theoretical peak force; each vibrator emitting 2 low-dwell sweeps (logarithmic) of 10 s length and 250 ms taper at the start and the end of the sweep. 80% of the sweep time was spent on frequencies from 8 -35 Hz and the rest on 35–60 Hz. The other alteration involved was the fold of cover, which was increased by 300% compared to the previous survey. A split-spread of 720 recording channels was used in this test with 24 geophones (10 Hz) per receiver group and 20 m group interval. The source interval was also 20 m with vibrator points being placed half-way between the receiver groups in order to emphasis the stack-array approach of Anstey (1986). Figure 1.3 shows the shooting spread configuration, the source array and the receiver array. The data were correlated and recorded on ½ inch magnetic tapes in SEG-D format. The listening time was 6 s which, by definition, is equal to the correlated record length.

### **1.3 Aims of the project**

Since all the surveys undertaken have failed to provide adequate results from the target horizon, it would appear that the problem is not acquisition-related but possibly something which involves the intrinsic properties of the ground. An initial hypothesis which I set out to test was that the lack of penetration was caused by the large variations in the acoustic impedance of thin layers within the Sirte formation. The cyclic layering of the Sirte formation is clearly revealed by the completion log of well D7-NC149.

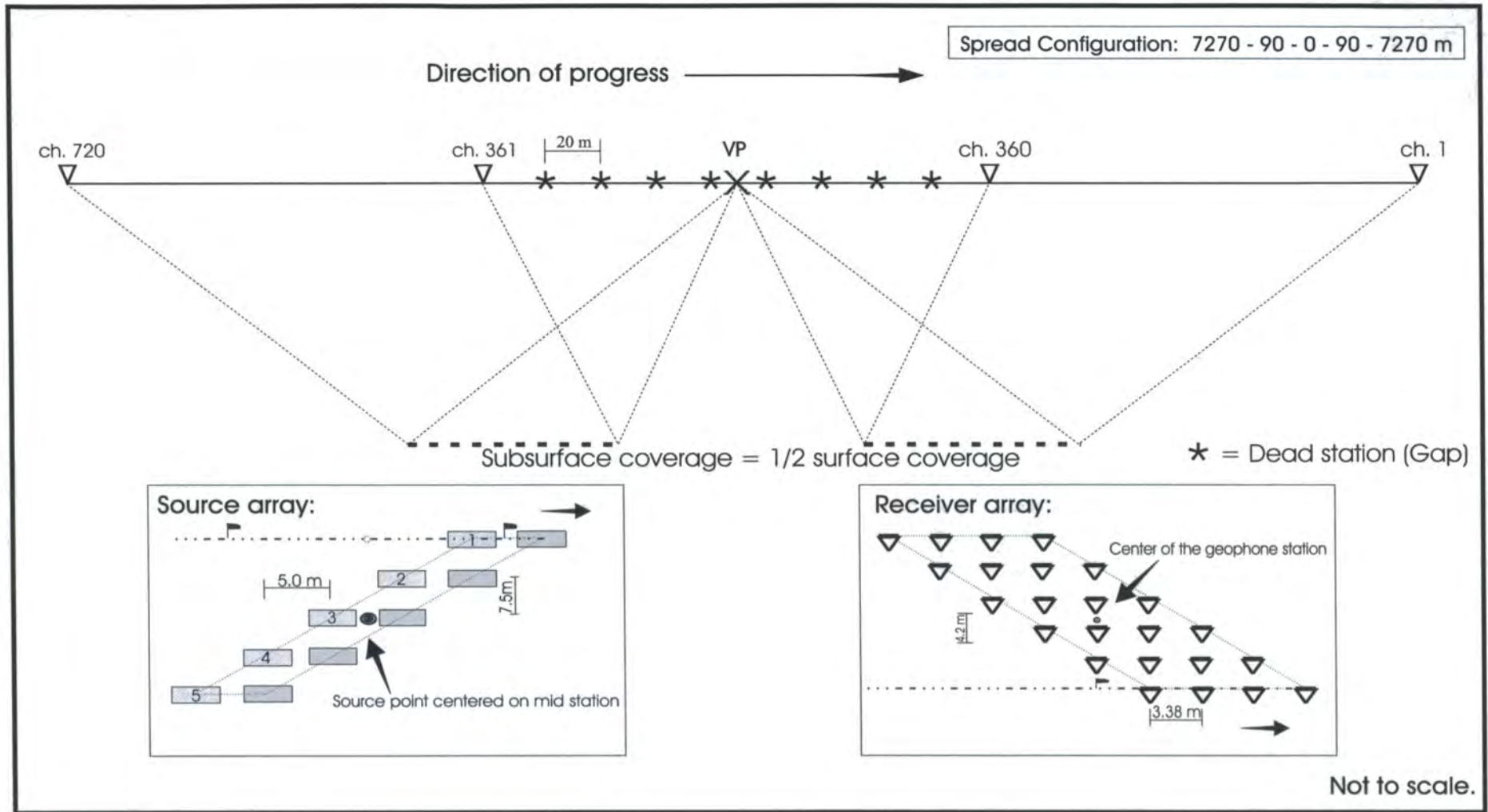


**Figure 1.3.** A schematic diagram illustrates the experimental line shooting geometry.

Therefore, it was suggested that the reprocessing of the 1995 experimental line should form a preliminary part of this study, whereas the principal aim of the project was to investigate the cause of the problem that limits the signal penetration below the top Kalash. To accomplish this principal aim, some 1-D synthetic seismograms were generated, using well log data and a variety of frequency bandwidths, in order to understand the combined effects of the transmission losses and the multiples on the primary reflections. The main purpose of the reprocessing was to study closely the changes in the data quality throughout the processing steps, and to see if the final result is consistent with the primaries-only 1-D synthetic data generated by using a frequency bandwidth similar to that of the source signal employed in collecting the experimental data.

# CHAPTER TWO

## Geology of the Wadi Field

### 2.1 Introduction

The Wadi Field (the area of study) is located within the south central part of the Hagfa Trough in the Sirte Basin (Figure 1.1). Development of the Sirte Basin was associated with normal faulting which created horst and graben structures, subsidence and tilting in response to widespread crustal extension of older Precambrian basement and Palaeozoic rocks. This basin remained a positive element until near the end of the Cretaceous, at which time the Sirte area was gradually submerged, probably for the first time since the early Palaeozoic. Conant and Goudarzi (1967) and Selley (1968) mentioned that the faulting in the Sirte Basin began to develop in the Late Cretaceous period and continued through the Miocene, and most likely into the Holocene. Gumati and Kanés (1985) concluded that the tectonic activity in the Sirte Basin was relatively slow during the Late Cretaceous compared to the Tertiary period, during which the rate of subsidence reached a maximum level. Clifford et al. (1980) stated that the present onshore Sirte Basin developed near the end of the Middle Miocene, succeeding the tectonic instability that peaked during the Oligocene and Early Miocene, and resulted in regional uplift and clastic infill of the Sirte depression. Faults are thought to have been periodically reactivated throughout Tertiary time.

The Sirte Basin is a major contributor to hydrocarbon production in the Mediterranean and Africa. Large quantities of recoverable oil and gas accumulations have been discovered, mainly in sedimentary rocks of Cretaceous and Tertiary ages, although fractured granites are also oil-bearing rocks.

## **2.2 Wadi palaeo-high structure evolution**

The Wadi Field structure is a tilted horst block developed from a series of step away fault blocks during the differential subsidence of the Hagfa Trough, which started shortly after the Turonian. The Sirte Basin comprises several troughs. Each trough has its own minor structural framework of faults, and the framework of each individual trough is a part of the entire structural framework of the Sirte Basin (Conybeare, 1979). The regional tectonic evolution in the basin is therefore responsible for the provenance and deposition of the sediments that built the sedimentary section in the study area. In addition, the structural activity has played a key role in developing the tectonic fractures, which provide the effective porosity in the Nubian quartzitic sandstone reservoir of the Wadi Field, as seen in core and by borehole imaging. Structurally, the Lower Cretaceous reservoir lies within a province of NNW-SSE trending faults, and is bounded by two major sub-parallel faults with this strike which are connected by small faults that merge together to form the Wadi faulted anticline (El-Jard 1988).

## **2.3 Lithologic summary of the Wadi Field sedimentary sequence**

The total thickness of the sedimentary section in the study area ranges from 12000 feet to more than 15000 feet. This section is formed by the Lower Palaeozoic clastic non-reservoir red siltstone (Gargaf group) which unconformably overlies the Precambrian igneous rocks, the Lower Cretaceous continental and lacustrine sediments of the Nubian formation, and the post mid-Cretaceous unconformity marine deposits of Upper Cretaceous and Tertiary ages, as illustrated by the lithologic log (Figure 2.1). Locally more than 11200 feet of marine carbonates and shales are preserved in the Wadi Field with evident changes in facies relationships both vertically and horizontally.

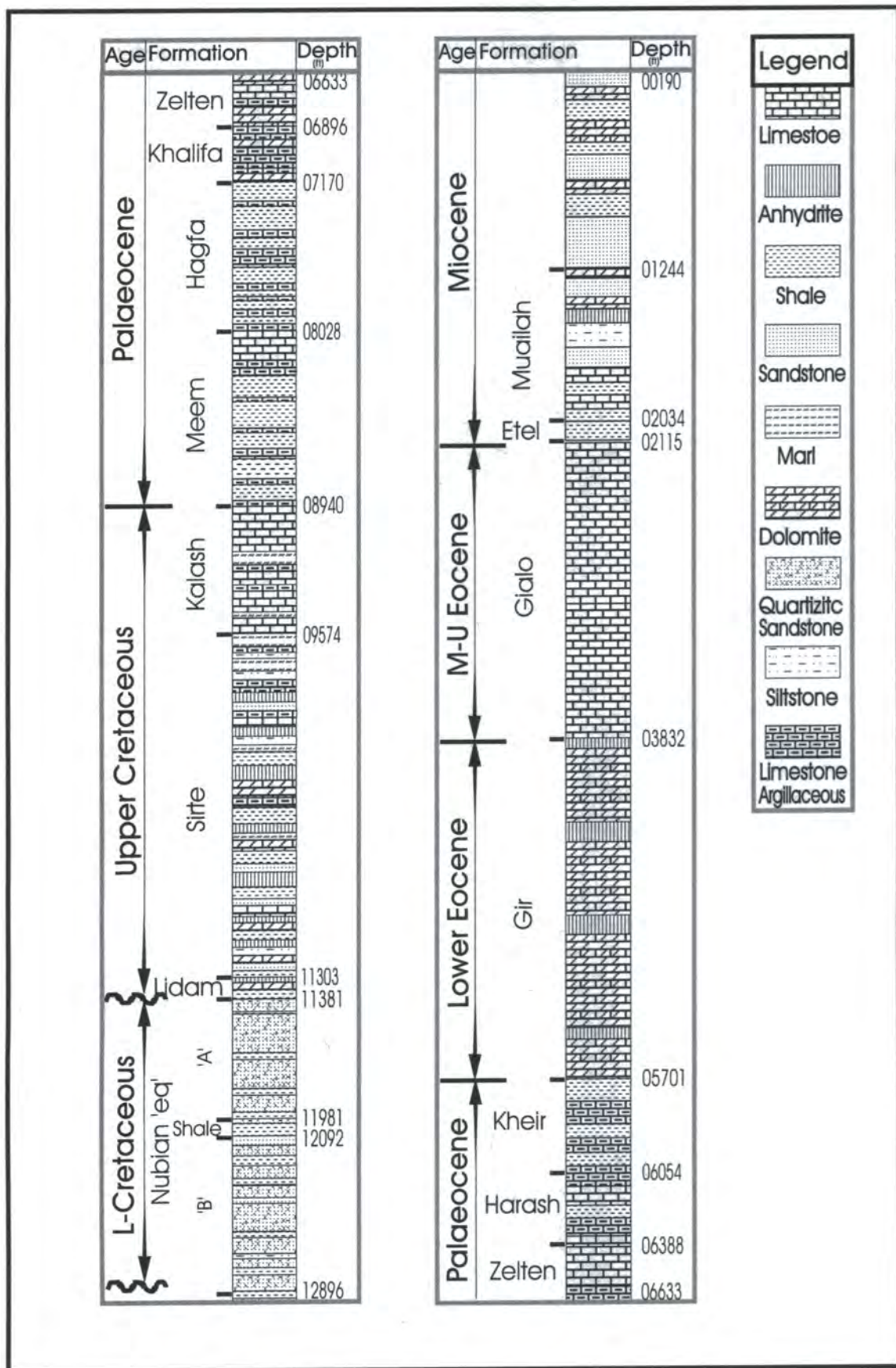


Figure 2.1. Lithologic log of Well D7-NC149. Depths were measured from the Kelly Bushing.

### Cambro-Ordovician deposits

As the deepest wells in the area have not penetrated the basement rocks, the actual thickness of the Palaeozoic sediments in the area is not yet known. Clifford et al. (1980) mentioned that most of the section was probably eroded during the development of a broad tectonic arch during the Palaeozoic at the site of the Sirte Basin. Evidence from deep wells in the Wadi Field indicates that the remaining Palaeozoic non-reservoir section is of Cambro-Ordovician age, and consists of pigmented red siltstone intercalated with dark grey silty shale.

### Cretaceous deposits

The Cretaceous deposits are divided by the intra-Cretaceous unconformity at the base of the marine Upper Cretaceous sequence into two major depositional periods. The surface of the unconformity reflects cessation of non-marine sedimentation, and is of profound stratigraphic importance to the entrapment of the hydrocarbon accumulations in the underlying Cretaceous sandstone. The pre-unconformity deposits act as well defined reservoir rock for the primary exploration target which is comprised of two stratigraphic units (Nubian 'A' and 'B'), separated by a highly radioactive thin shale bed (Figure 2.1). They consist of quartzitic sands and quartzites, with clean quartzarenites containing 95% quartz grains (McBride and Jonas, 1963). Depositional environment changes from aeolian to lagoonal or lacustrine conditions have introduced some shale stringers, especially in the bottom unit. The formation has an average thickness of about 1969 feet. This section unconformably overlies the preserved section of the highly eroded Palaeozoic sediments.

The post-unconformity (Upper Cretaceous) section is considered to be made up of three formations: Lidam, Sirte, and Kalash. The Lidam beds document peripheral marine and

shallow marine depositional environments, which resulted in lithology changes from shale to dolomite and anhydrite. The Sirte Shale of Campanian age indicates a low-energy depositional environment, and comprises a thick section of alternating shale, dolomite and anhydrite beds. The intercalation becomes more predominant toward the bottom of the sequence, and provides a sensitive indicator of depth changes resulting from the block faulting that occurred during the time of sedimentation. The Sirte Shale is believed to be the source rock for all Cretaceous and possibly some younger reservoirs, not only in this particular area but also for some other fields in the basin, and acts as a regionally effective cap-rock for the Cretaceous reservoirs. The maximum thickness of this sequence is present in the south of the field, where it exceeds 4500 feet.

The Cretaceous closed with shallow marine deposition of relatively widespread Kalash carbonates, subsequently followed without any break in deposition by the deepening which marks the onset of the Palaeocene period (Barr and Weegar, 1972). In the area of study the Cretaceous-Palaeocene boundary lies between the Kalash Limestone and the Meem Shale, and is the deepest horizon that has been identified on the processed seismic sections.

### Tertiary deposits

Sediments of this age are found to be correlatable with similar sections on the adjacent Zelten platform (Figure 1.1), which suggests that during this time the sedimentation was dominated by sediment supply from the east. Extensive deposition of carbonates and subsidiary shales took place as a result of a major marine transgression throughout Palaeocene and Eocene times. The Khalifa formation, which underlies the Zelten formation, comprises calcareous, grey-green shale, and acts as a lean source rock in the Wadi area. The Late Palaeocene formations contain some of the most significant

reservoirs in the Sirte Basin, such as the Zelten Formation on the Zelten platform. The Palaeocene sediments conformably underlie the Lower Eocene strata (Gir Formation). The Gir formation consists mainly of evaporitic interbeds of dolomite and anhydrite with occasional limestone, while the overlying Gialo formation of Middle - Upper Eocene age consists largely of limestone and dolomitic limestone.

# CHAPTER THREE

## Reprocessing of 1995 experimental line

### 3.1 Introduction

The line (149V1211-95) consists of 1011 source stations of which 100 stations were omitted due to ragged terrain and pipelines. This has resulted in a total of 911 shot records with 528080 traces to be processed. Due to rolling-on and rolling-off recording spreads (maximum far offset is 7270 m), the full subsurface coverage of 360-fold does not cover the whole line. It is supposed to cover the area between source station 183 and source station 829, but due to the omitted source stations and edited noisy traces the full fold of cover has only been achieved over a short distance, between source stations 183 and 201. It decreases to 277-fold at source station 616. Figure 3.1 illustrates the location of the skipped source stations, and the fold of cover at every station. Note that the line was shot (from high surface station numbering to low) in a direction opposite to the direction it was laid out. Source station 1 corresponds to surface station 1111, and source station 1011 corresponds to the first surface station (101).

The field data (demultiplexed) were supplied on three 8 mm cartridge tapes after they were converted by CGG from the original format (SEG-D) to a standard SEG-Y format. A considerable time loss was experienced while trying to transfer the data onto a ProMAX workstation. CGG copied the sweep auto-correlation, which was originally recorded on an auxiliary channel, to a trace labelled channel 1 in the header.

Unfortunately, they did not change the channel numbering on the shot gathers which begins with channel number one. Consequently, channel number one is duplicated: one channel has the sweep information and the other has the seismic data recorded by the

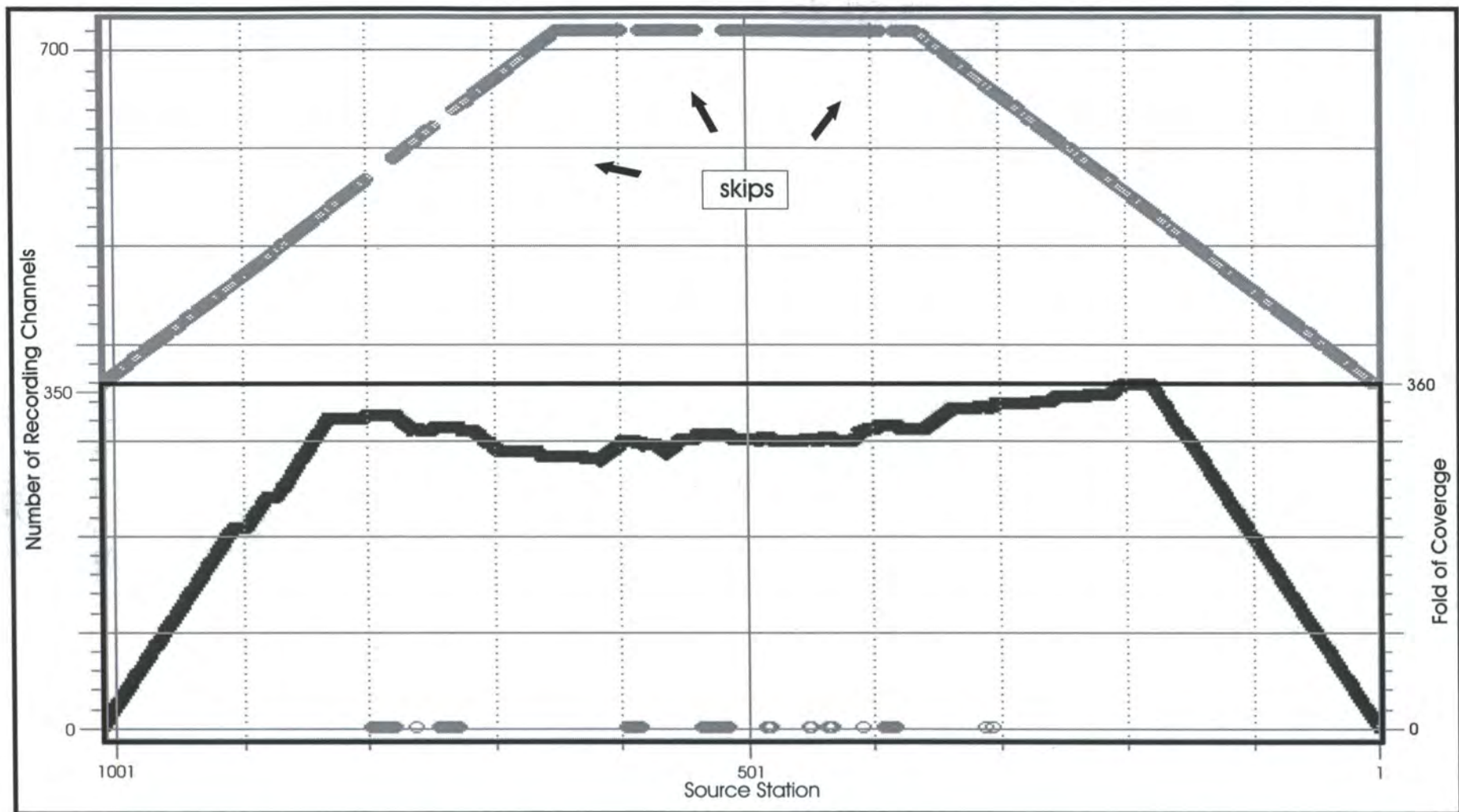


Figure 3.1. Diagram illustrates number of recording channels and fold of cover at each shot point.

first geophone group on the recording spread. As a result of this mistake, the maximum number of channels per common-shot gather (the only header key word available for traces in shot gathers at this time) was increased from 720 to 721 channels. Due to the very large shot gathers, limited disk space, and limitations in screen resolution, I had to read the data a couple of times before I realised the flaw. To get rid of the extra channel on each shot gather, channels had to be renumbered at the same time the data were imported into the system.

## **3.2 Geometry information**

The computation of geometry information requires the observer's log, source and receiver statics (supplied on floppy disk in ASCII format), and survey data (supplied on floppies in UKOOA format). Data supplied on floppy disks were transferred to the hard disk using the FTP program, available on all PCs in the computer room of the geology department. This information is sufficient to calculate source-receiver offsets, CMP coordinates and ensembles, and other database geometry information required by ProMAX. Setting up the database files and initialising it with all the necessary geometry information was done independently of the seismic data. Following a successful "Geometry Spreadsheet" execution, all essential geometry information was automatically stored in separate database files on the hard disk.

## **3.3 Downloading of field data**

### **3.3.1 SEG-Y input**

This flow transfers the input data directly from the exabyte tapes onto the hard disk ready for processing on a ProMAX workstation. Since the large amount of data and the limited disk space prevented having two large data files on the hard disk at the same time, trace renumbering, geometry assignment, source and receiver statics, and trace

editing were all combined in a single flow with the SEG-Y input process. More disk space was purchased at a later stage during the project.

### **3.3.2**      Trace renumbering

Traces on all common-shot gathers were renumbered from 0 to 720 using the “Trace Header Math” process. This step was then succeeded by the “Trace kill/Reverse” process to kill the first trace (channel 0) on each shot gather.

### **3.3.3**      Geometry assignment

The geometry information computed in section 3.2 was loaded to the trace headers using the “Inline Geometry Header Load” process. All geometry information was transferred from the database files into its appropriate locations in the trace headers; each trace was then accurately located and ready for processing applications.

### **3.3.4**      Database header transfer

The main objective of this process was to transfer the static values from the input database files to their relevant locations in the trace headers, and not to apply them. This process was run successively twice in order to transfer both the source and receiver statics.

### **3.3.5**      Trace editing

Common-shot gathers were individually viewed on the screen and examined for noisy and reverse polarity traces. Bad traces were then carefully marked after examination of the “Screen Display” and killed by reapplying the “Trace Kill/Reverse” process. Noisy traces were input using an editor. Occasionally hardcopy plots were also used.

Figure 3.2 shows a shot gather with bad traces zeroed out. Automatic gain control (AGC) has been applied (compare figure 3.2 and figure 1.2).

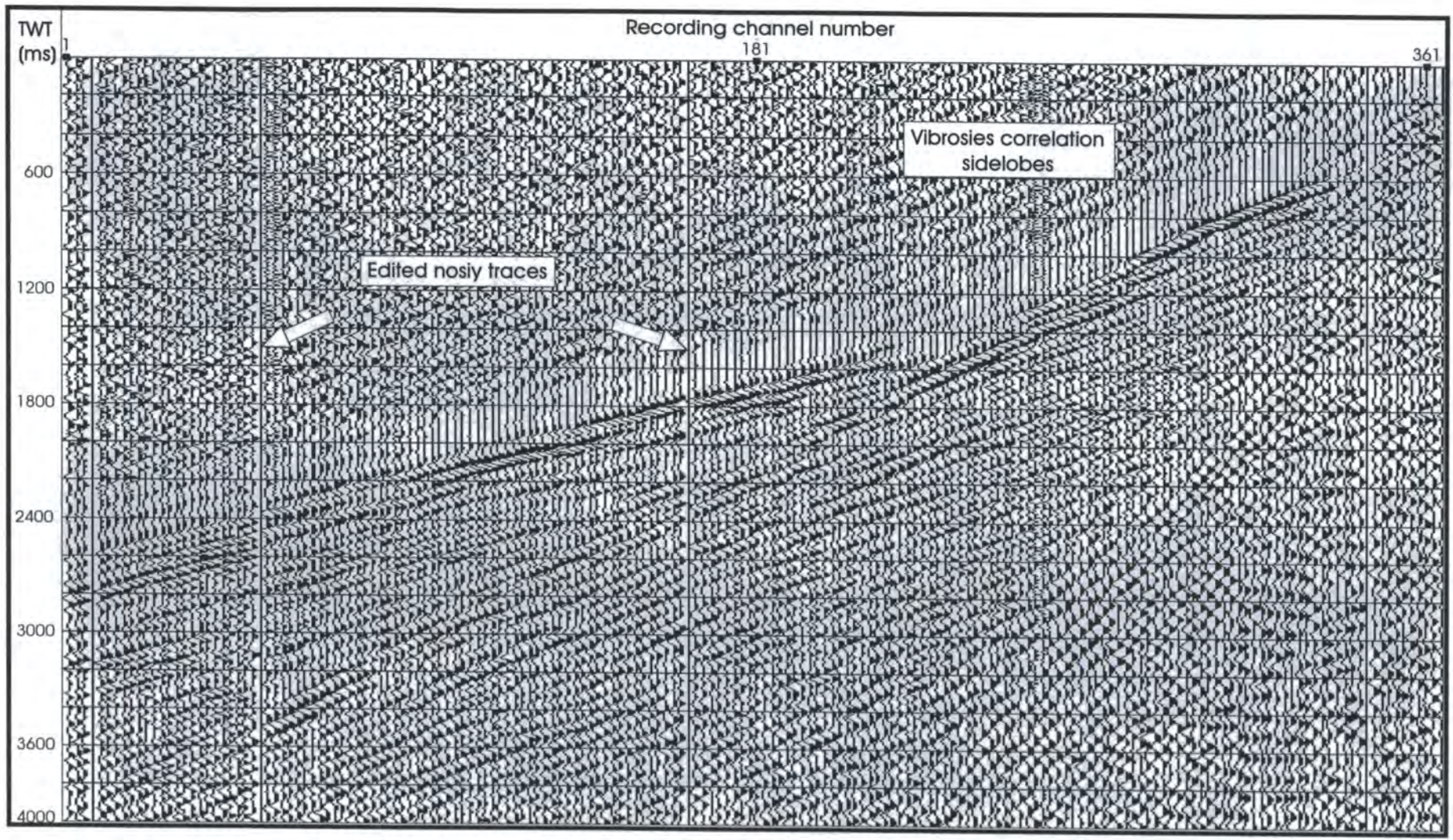


**Figure 3.2.** Common-shot gather 408 with edited noisy traces. Automatic gain control (AGC) is applied. For display purposes, only half of the record with every second trace (i.e. 40 m trace spacing) and 4.0 s two-way travel time is shown.

### **3.4 True amplitude recovery (TAR), statics, and trace muting**

#### **3.4.1 True amplitude recovery**

The spreading of seismic energy from a point source in a uniform medium causes the amplitude to decrease inversely as the distance the wave has travelled. While the seismic wave is spreading out, it is reflected and refracted at boundaries and attenuated by the rock that it is travelling through. Because of these effects, the reflected energy from a deep geological structure will arrive at the geophone array as a weak signal. To compensate for these losses, a single time-variant gain function is applied, which can either be based on the reciprocal of the distance the wave has travelled, or on a function of travel time and velocity. The actual function applied in this job is  $(\text{time} \times \text{velocity})^2$ . Velocities and travel times were adopted from previous work.

#### **3.4.2 Static corrections**

To remove travel-time differences from trace to trace due to elevation and weathering layer changes, the data must be corrected to a reference datum. This might still leave some short-period static shifts from trace to trace due to uncertainties in the near-surface velocities, which can be corrected later by using some residual static programs.

Statics computed in the field (already in trace headers, section 3.3.4) were applied to the data using the "Header Statics" process. In this step source and receiver statics were read from trace headers and applied to the individual traces in the shot gather.

The stacked section obtained using these statics showed poor stacking quality with broken up and mis-aligned reflectors, particularly in the area above the scarp. I suspected that the cause is inadequate statics computed using weathering information from an old seismic line above the scarp. Sirte Oil Company has drilled no up-holes in

this area due to logistical problems. Figure 3.3 shows the location of the scarp and the up-holes drilled below it. Because of the unsatisfactory result, I decided to recompute the statics using information from deep up-holes drilled recently above the scarp by a different client. The nearest up-hole is 6 km away from the start of the line. Based on this information, average weathering velocities and depths were computed and projected on to the surface stations 101 and 206, to be used as a static control points (Table 3.1). The weathering information assigned to the surface station 435 was quoted from the static information of an old line that intersected the experimental line at this station.

Statics were initially computed for stations at the up-hole and control point locations using the information in Table 3.1, and then interpolated for stations in between using a spread sheet program. Changes in elevation and base of weathering are taken into account.

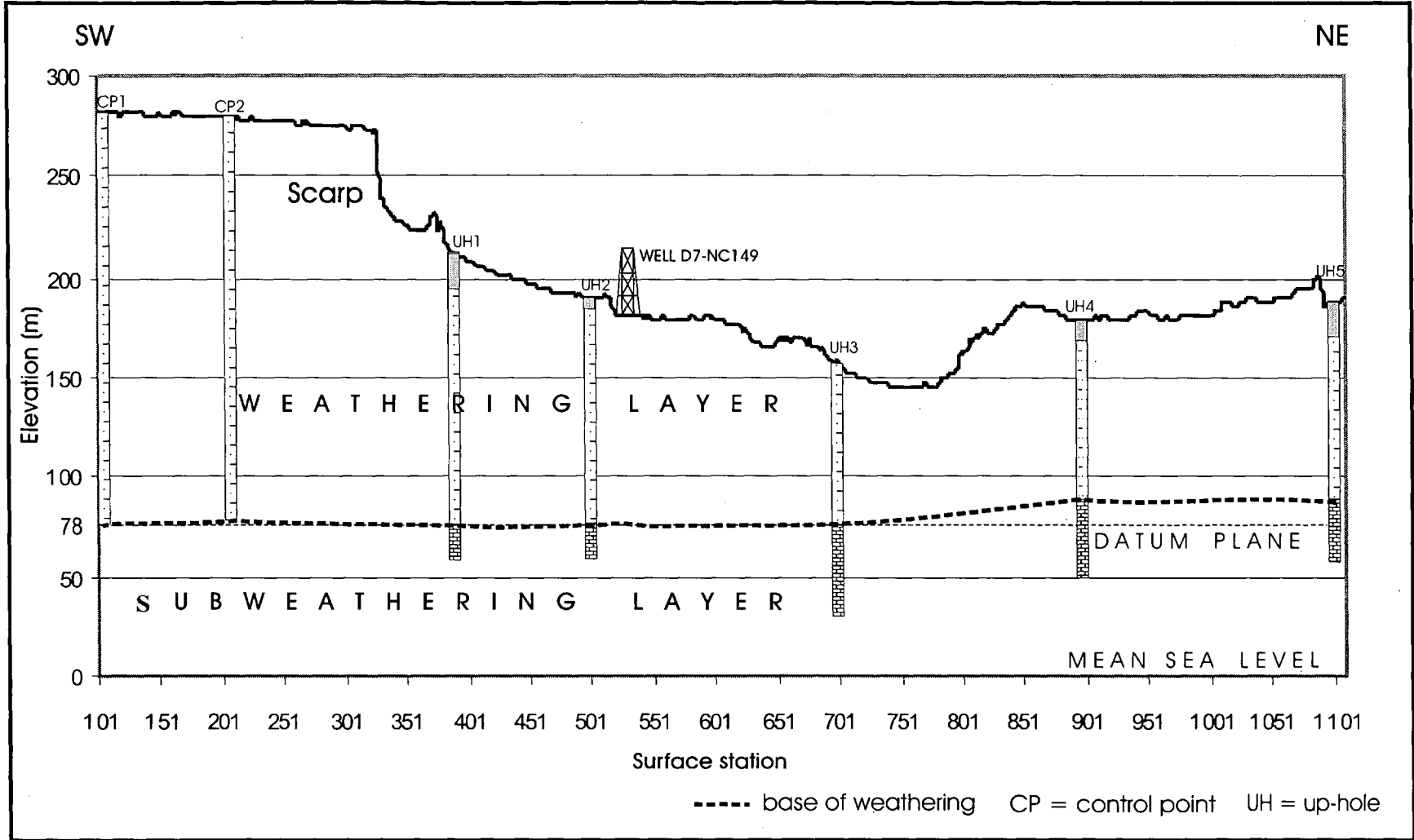


Figure 3.3. Upholes cross-section showing base of weathering.

| Surface station | Surface elevation (Es) m | Base of WX (Ew) m | Weathering (WX) velocity m/s | Sub-WX velocity m/s |
|-----------------|--------------------------|-------------------|------------------------------|---------------------|
| 101             | 283                      | 78                | 999                          | 2200                |
| 206             | 279                      | 79                | 1000                         | 2196                |
| 386             | 214                      | 78                | 1015                         | 2190                |
| 435             | 201                      | 81                | 1000                         | 2200                |
| 500             | 189                      | 78                | 888                          | 2270                |
| 696             | 158                      | 78                | 930                          | 2000                |
| 900             | 180                      | 85                | 1138                         | 2120                |
| 1100            | 188                      | 82                | 1116                         | 2400                |
| 1111            | 190                      | 82                | 1060                         | 2400                |

Table 3.1. Weathering and sub-weathering information used to recompute the source and receiver statics for the entire line.

For statics computed by the seismic crew in the field, mean sea level was chosen as the final datum. But for those I computed, the top sub-weathering horizon at an elevation of 78 m above sea level was chosen as the final datum (Figure 3.3). It is remarkably flat, as depicted by the five up-holes drilled on the low side of the scarp as well as the deep up-holes on the high side of the scarp.

### 3.4.3 Trace muting

A wide prestack mute function, to suppress the first breaks and the primary refractions, was applied using the “Trace Mute” process. A ramp to smooth amplitudes over a transition zone has also been applied, so that no misleading steps will be produced at the ends of the muted segments. The mute function is created interactively using the “Screen Display”, written to a file, and retrieved from the database when it is to be

applied to the shot gathers. The common-shot gather in Figure 3.4 shows the mute function applied at this stage.

### 3.5 *F-K* Filtering

Frequency-wavenumber filtering attacks coherent noise by discriminating between reflection events and noise on the basis of their apparent horizontal velocity. Events that dip in the  $t$ - $x$  plane can be separated in the  $f$ - $k$  plane by their dips, since events with faster horizontal velocity lie closer to the  $f$ -axis in the  $f$ - $k$  plane and vice versa. The 2-D Fourier transform is the basis of both analysis and implementation of apparent velocity filtering (multi-channel process).

Seismic noise can be coherent or random. Coherent noise is usually source-generated (groundroll, guided waves and airwaves) and moves across the spread from trace to trace in some organised fashion. Random noise is not organised and generally would not duplicate. *F-K* filtering is a very powerful tool used to attack coherent noise in processing, but it must be used carefully to avoid possible processing artefacts (Hatton et al., 1986). In particular, it is important to avoid spatial aliasing, which could result in poor filtering performance. The practical approach to avoid this problem is to apply the  $f$ - $k$  filtering on common-shot gathers rather than on CMP gathers, since the distance between CMP traces can sometimes be twice as long as the trace spacing of the shot gather (Yilmaz, 1987). This applies on the present dataset where both the source and receiver group intervals are of the same length.

Before  $f$ - $k$  filtering, the “*F-K* Analysis” tool was run to produce  $f$ - $k$  plots and allow interactive picking of  $f$ - $k$  filter (polygon) parameters. This tool transfers the data from time-space domain to frequency-wavenumber domain and displays the results on the

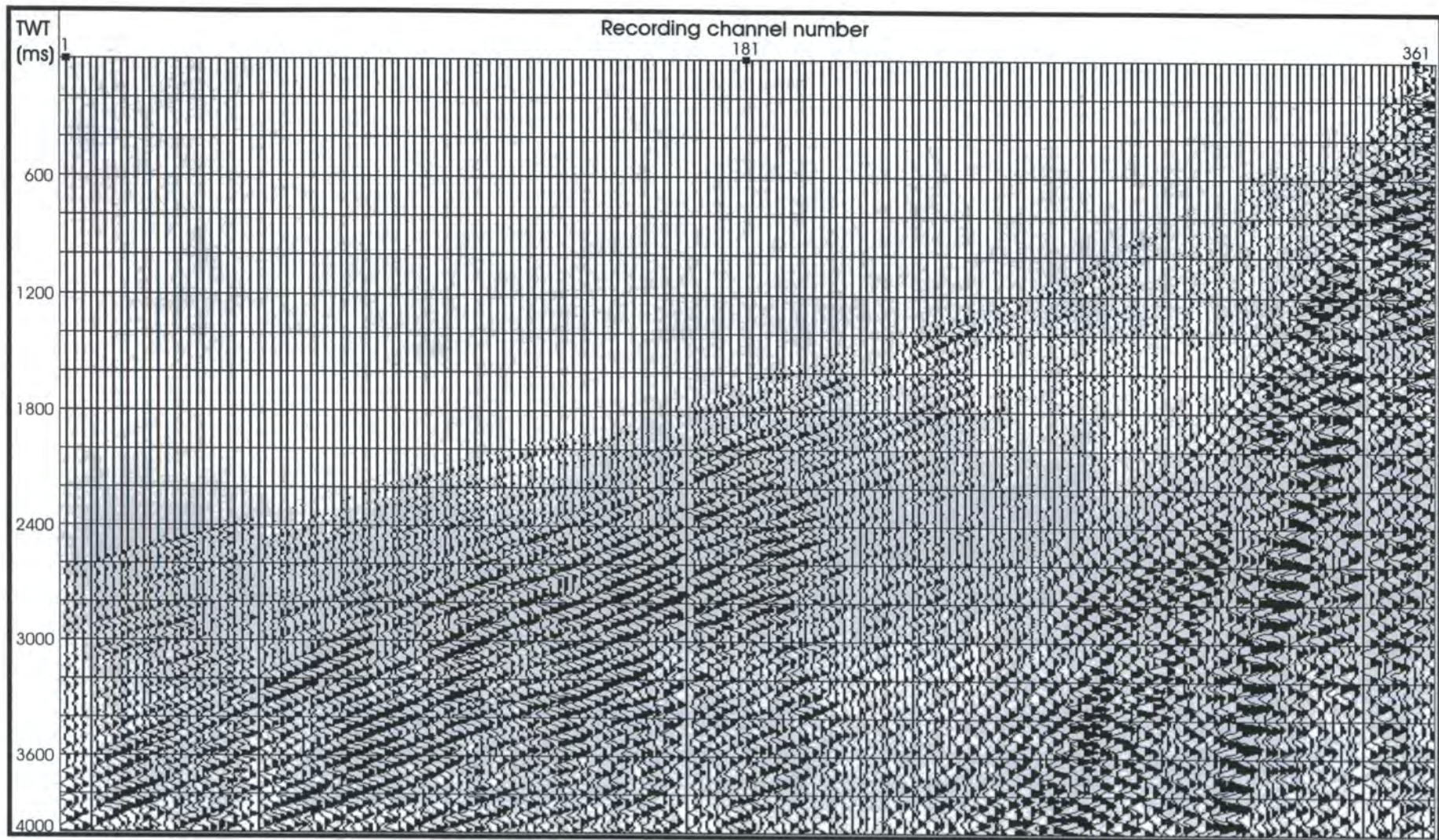


**Figure 3.4.** The common-shot gather in Figure 3.2, without AGC, after application of TAR, statics and mute.

screen to allow selection of the  $f-k$  filter parameters. The important point is that the reflection energy falls within a narrow wedge that is centred on the frequency axis, whereas noise diverges away towards the wavenumber axis, depending on its dip in the  $t-x$  plane.

The boundaries between the pass and reject zones were specified through positive and negative cut lines with a dip equal to 1/4000 s/m (Figure 3.5a), i.e., all events on shot record with horizontal velocity less than 4000 m/s are rejected, and events with higher velocity are passed. The transition between the pass and the reject zones was appropriately smoothed in order to minimise the ringing effects on the filtered data.

Automatic gain control (AGC) was applied to the input data. This is mainly to avoid the effect of the highly variable amplitudes in the data: the strong events will dominate the  $f-k$  spectrum, and filtering may cause artefacts of these events to spread to other regions in the  $t-x$  domain.

“Ensemble Redefined” is mandatory for data recorded with split-spread geometry because the positive and negative offsets need to be filtered separately in the  $f-k$  domain. The separated ensembles (split shot gathers) were then recombined after the  $f-k$  filtering using the same process. For more details the reader is referred to the ProMAX manuals.

Although the transition zone along the specified boundaries was smoothed, distortion caused by ringing effects from high-amplitude refraction events is clearly contaminating the filtered shot gathers (Figure 3.5b). The events with strong amplitude that appear on the near-offset traces are spatially aliased high-frequency airwaves and groundroll. Primary reflections begin to appear at early times on the near offset traces, but no clear

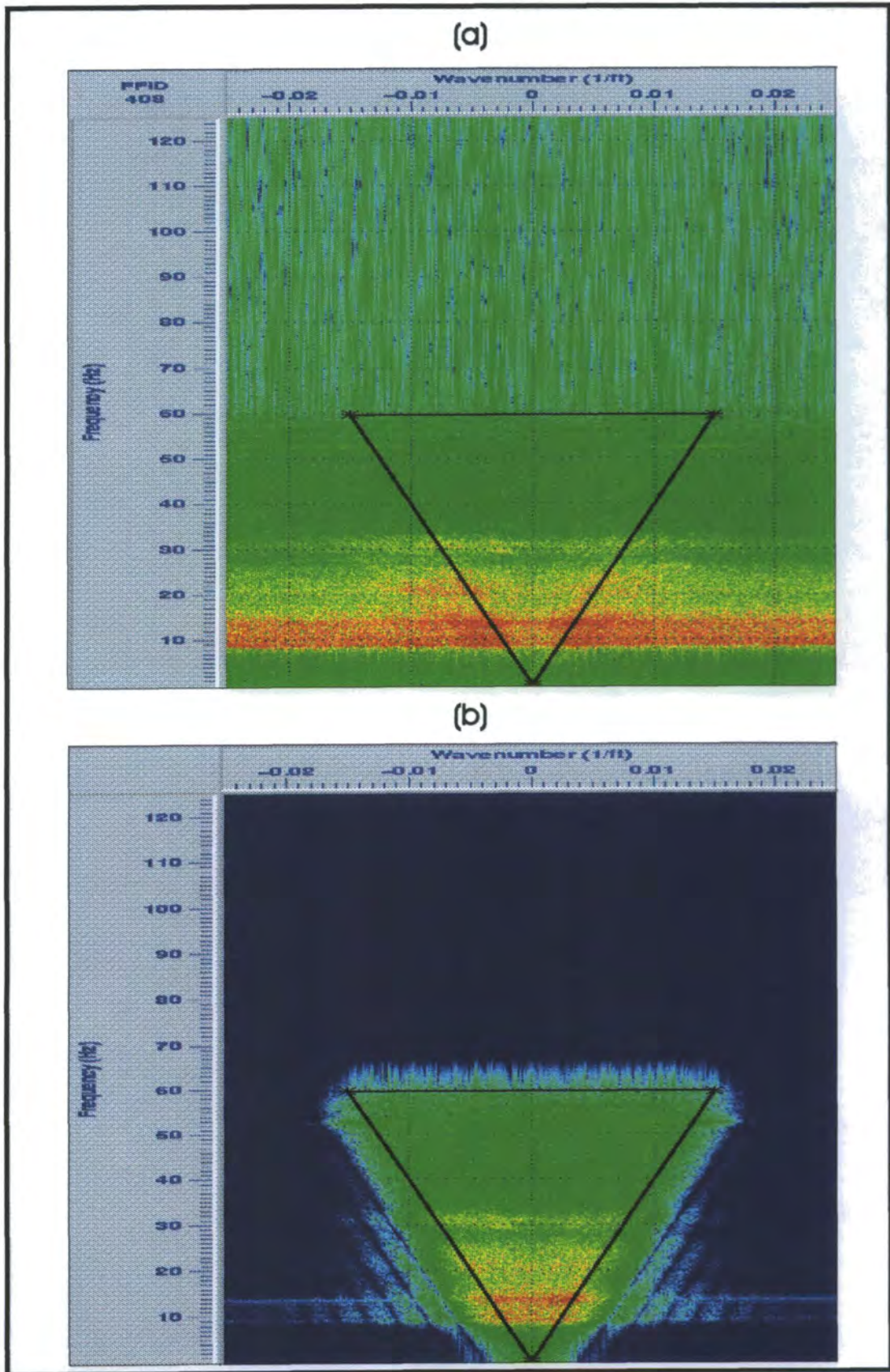


**Figure 3.5a.** The  $f-k$  amplitude spectra of the common-shot gather in Figure 3.4 (a) before and (b) after application of velocity filtering.

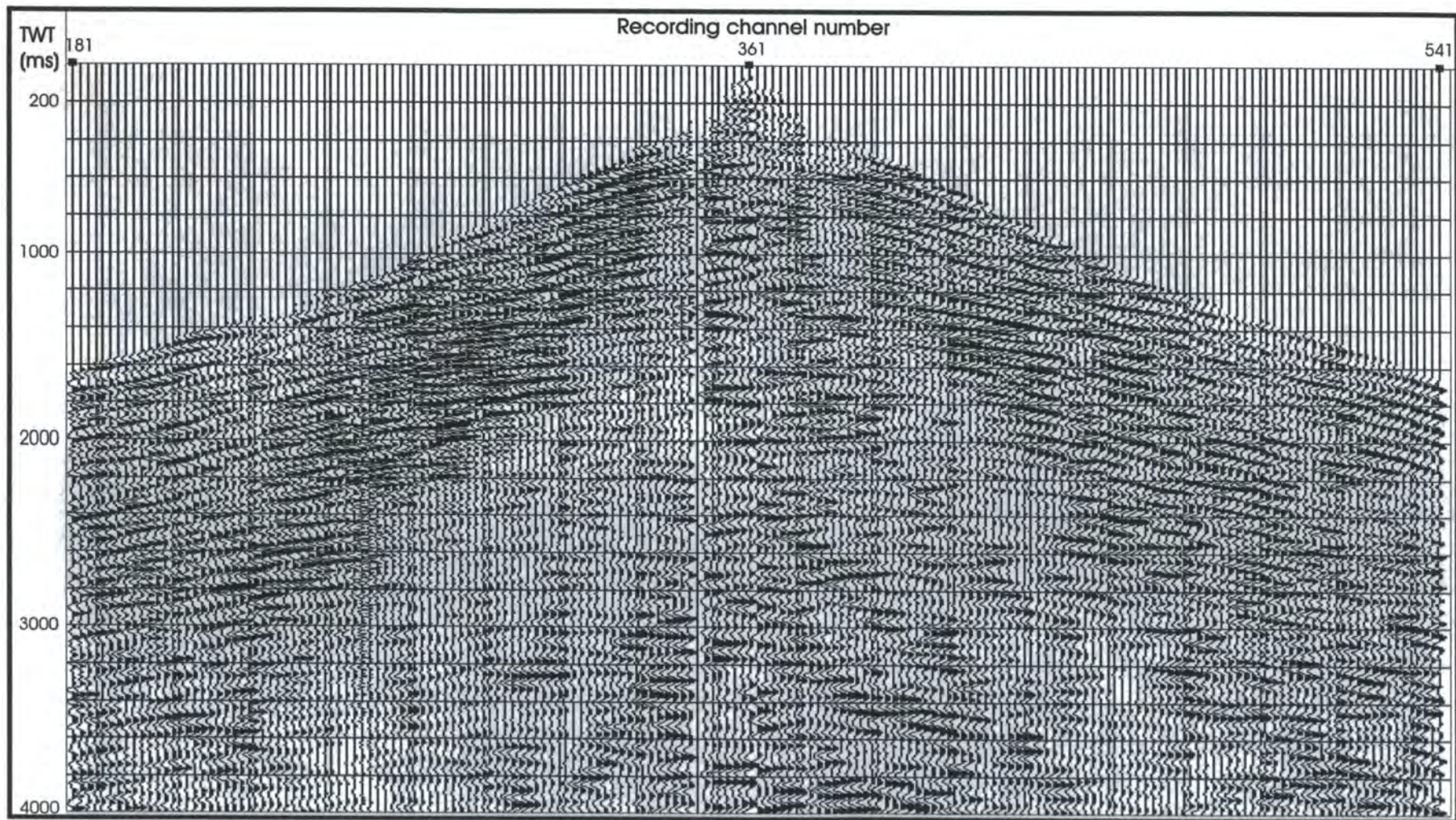


**Figure 3.5b.** The common-shot gather in Figure 3.4 after application of velocity filtering. Traces between 181 and 541 are shown.

reflections are apparent from horizons below 1200 ms two-way travel time. Liu and Gouly (1999) showed examples of shot gathers where  $f-k$  filtering failed to improve the signal to noise ratio: even where the apparent velocities of signal and noise are different, weak reflection events were still overwhelmed by the residual noise.

### **3.6 Prestack deconvolution**

The purpose of deconvolution is to increase the temporal resolution of the seismic data by compressing the effective source wavelet in the seismic trace and attempting to remove the undesirable multiple effects. In general, the deconvolution broadens the bandwidth, whereas in true amplitude recovery the objective is mainly to compensate for amplitude losses (Al-Sadi, 1982).

In order to choose the optimum deconvolution parameters (operator length, predictive distance, and white noise) several tests were conducted on different common-shot gathers selected at various locations along the line. Unfortunately, the poor quality of the seismic data has made it difficult to differentiate between the results from these tests.

The “Ensemble Deconvolution” was used to compute and apply a single deconvolution operator to all traces in the input shot gather.

Band-pass filter was applied directly after deconvolution. Its ultimate objective is to reduce the frequency spectrum to a reasonable range, because both high-frequency noise and signal are boosted. A single band-pass filter with four corner frequencies and ramps was used, the ramps being formed by cosine tapers in the frequency domain. The four corners (4-8-50-60 Hz) represent sequentially the 0% and 100% points of the low-cut

ramp, and the 100% and 0% points of the high-cut ramp. The previous mute function was reapplied to the output from this process.

Figure 3.6 shows a common-shot gather with predictive deconvolution applied.

Although the high frequency content has clearly been boosted, only a few reflection events which do not have smooth hyperbolic trajectories may be seen between 500 and 1200 ms on the near offset traces. There is still no improvement in reflections anywhere on the record at later travel times.

### **3.7 Common midpoint sorting**

The common midpoint (CMP) sorting process requires that the geometry information should already exist in the trace headers. Common midpoint gathers are numbered from 206 to 2218. CMP 206 corresponds to surface station 103, and CMP 2218 corresponds to surface station 1109.

The common midpoint gather in Figure 3.7 consists of 277 traces, each individual trace having come from a different shot gather. The steps along the mute edges are actually due to the omitted source stations, and not due to the designed mute function. Reflection events are more pronounced on the common midpoint gathers than on the common-shot gathers. This suggests that the contamination of shot gathers by edge effects as a result of  $f$ - $k$  filtering gives rise to coherent noise traces within each shot gather; but this noise is incoherent between different shot gathers, allowing coherent reflection events to be more clearly discerned on the common midpoint gathers.

### **3.8 Constant velocity stack (CVS)**

This was carried out on selected groups of 20 common midpoint gathers. Each group

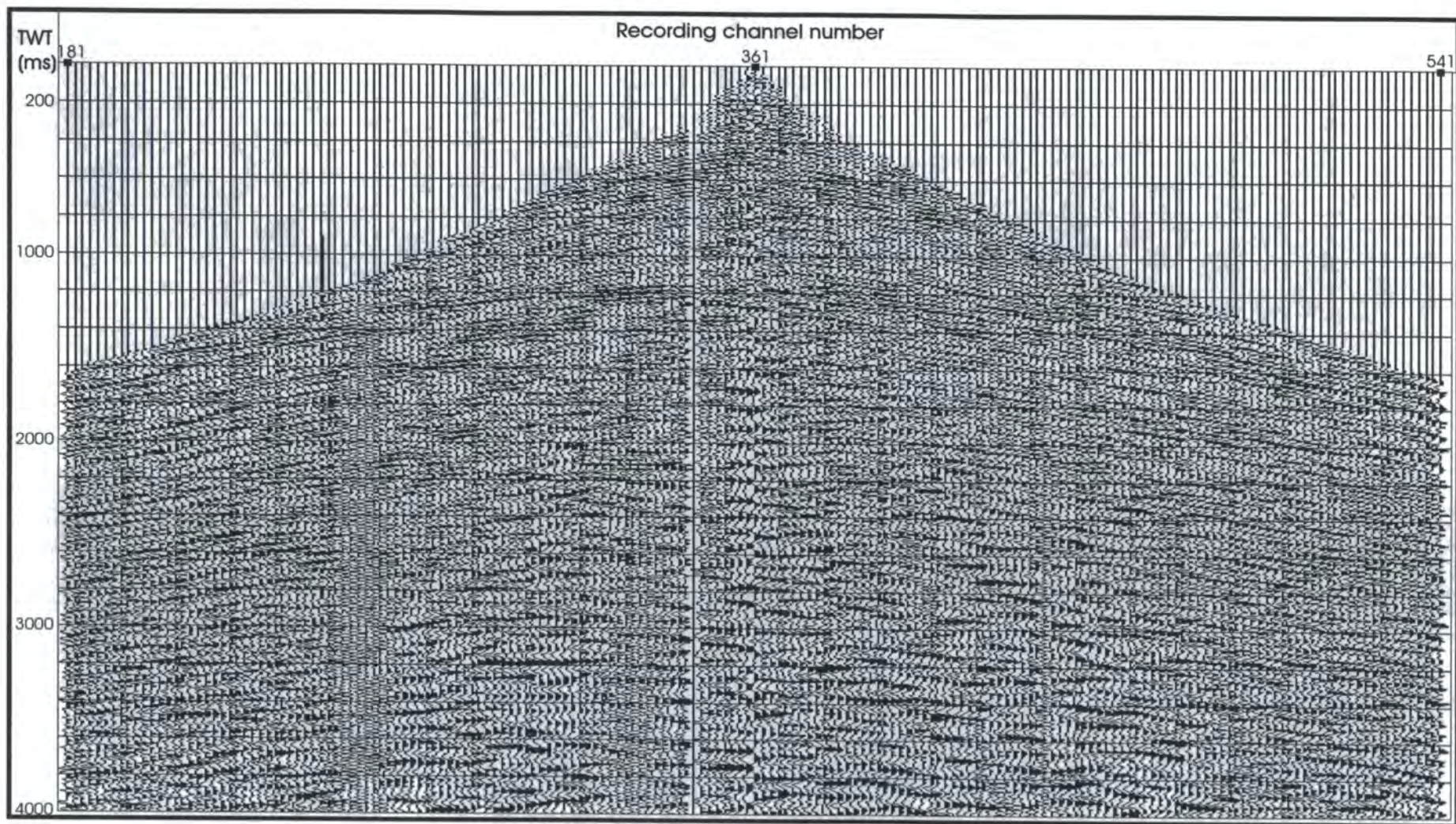


**Figure 3.6.** The common-shot gather in Figure 3.5 after application of predictive deconvolution with an operator length of 160 ms and a predictive gap of 24 ms.

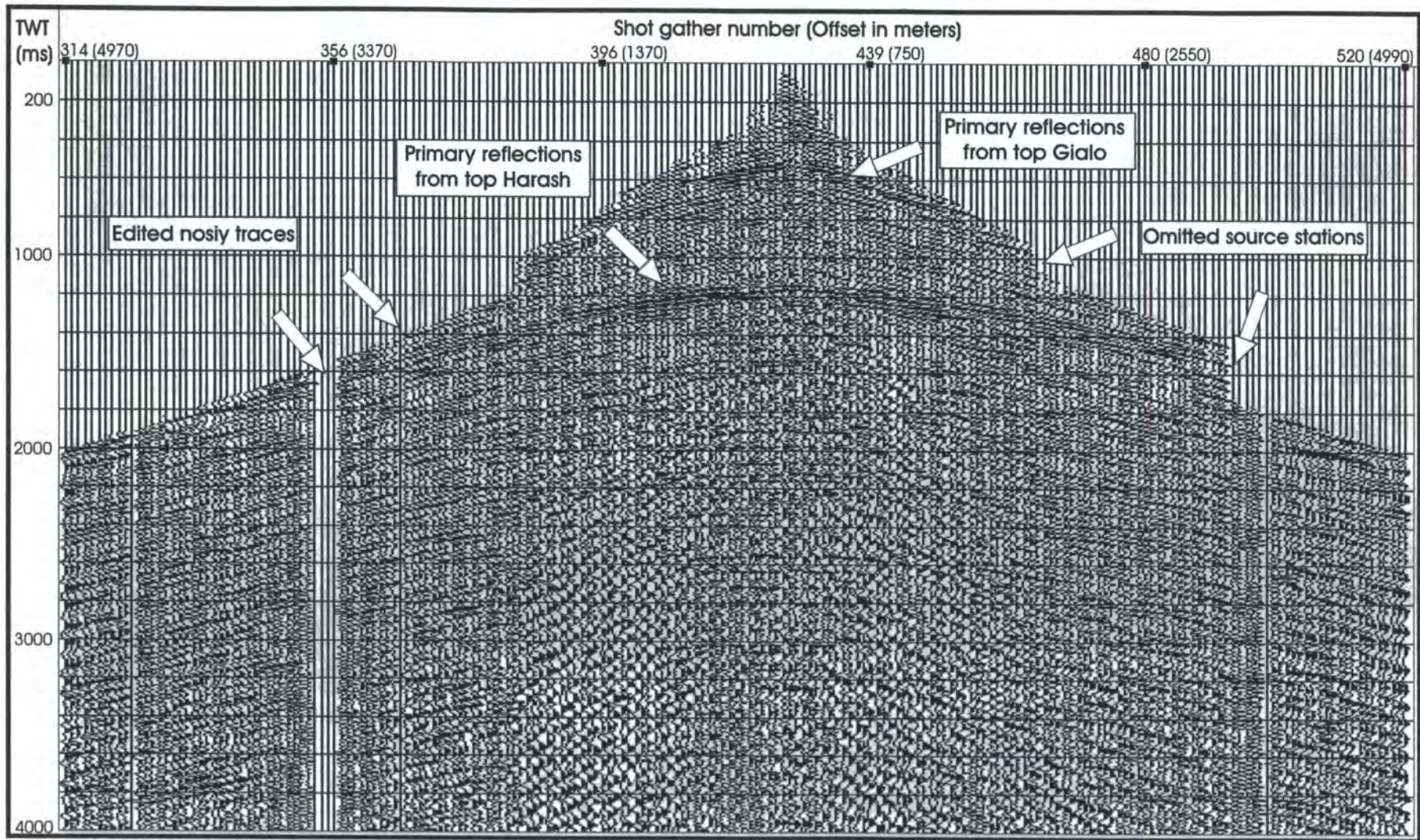


**Figure 3.7.** CMP 1346, sorted after velocity filtering and predictive deconvolution applied to the common-shot gathers. Trace spacing is 40 m.

selected for analysis was repeatedly stacked using a range of constant velocity values between 1800 and 4600 m/s. The same velocity was used for computing moveouts at all times on the gather. The stacked traces for each group were then displayed side by side (Figure 3.8) ready to pick the appropriate stacking velocities for each location. The velocity that best aligns each event horizontally within the gather, or stacks a particular event from all traces in a common midpoint at maximum amplitude, is picked as the normal moveout correction velocity. This procedure was repeated every 1 km (50 surface stations). The accuracy of the velocity picks depends on the S/N ratio, which is still inadequate at later travel times in spite of the prestack efforts to improve it.

The picked stacking velocities at each location were then assigned to the CMP in the middle of the group, and input through an editor ready for the normal moveout corrections (NMO).

### **3.9 Residual statics (autostatics)**

The residual static anomalies are static errors remaining after static corrections have been applied to the data. These errors arise from inadequate velocity information used in static corrections, and/or inadequate depth control of weathering and subweathering layers. The objective of the autostatics process is to find the additional time shifts (static errors) that optimise the CMP stack. The shifts are time-invariant, surface-consistent, and independent of frequency. The surface-consistency means that time shifts are solely dependent on source and receiver locations, and not on the raypaths from shots to receivers. A problem in resolving these errors arises when the spatial wavelengths of the static anomalies are larger than half the length of the recording spread used to record the data (Marsden, 1993).

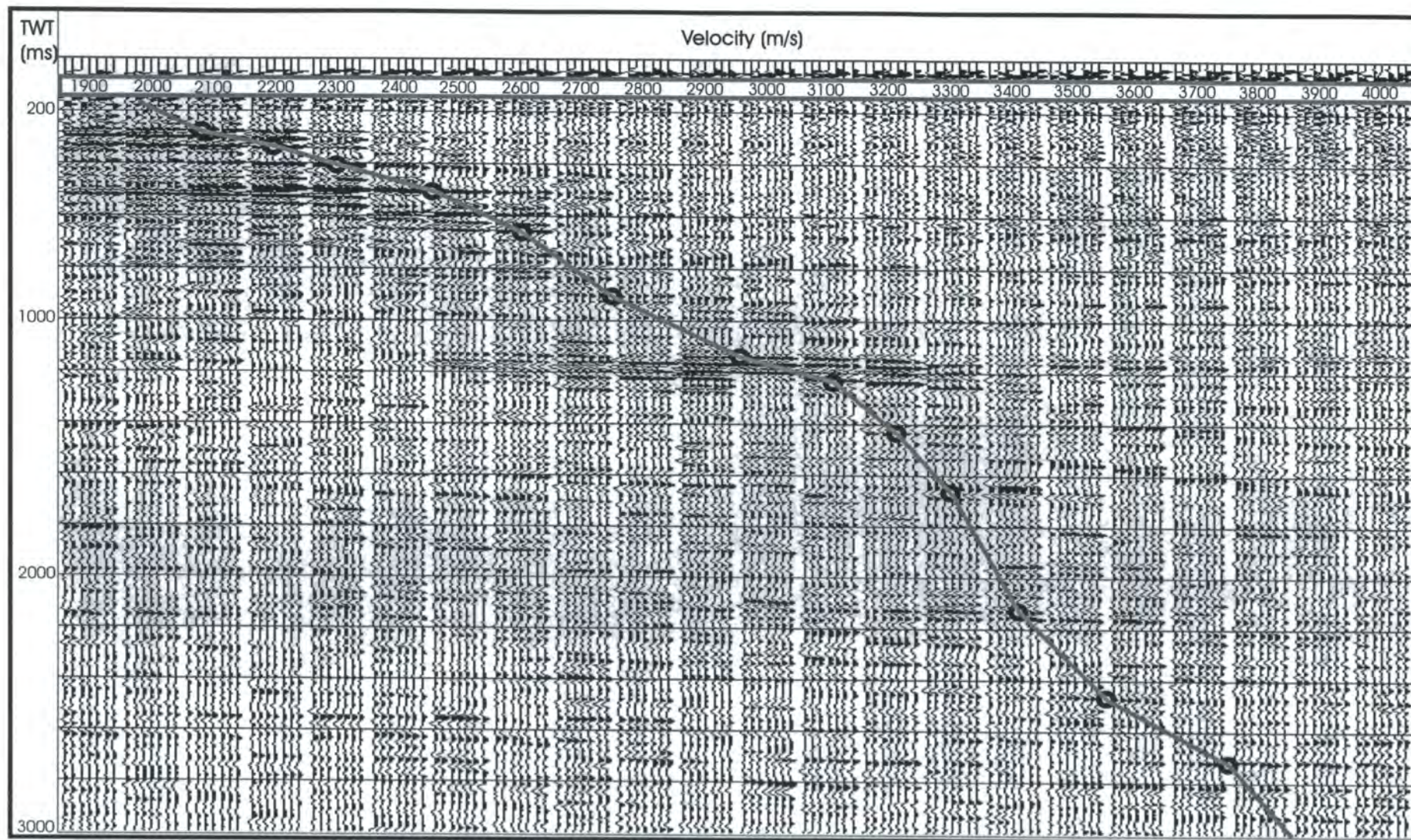
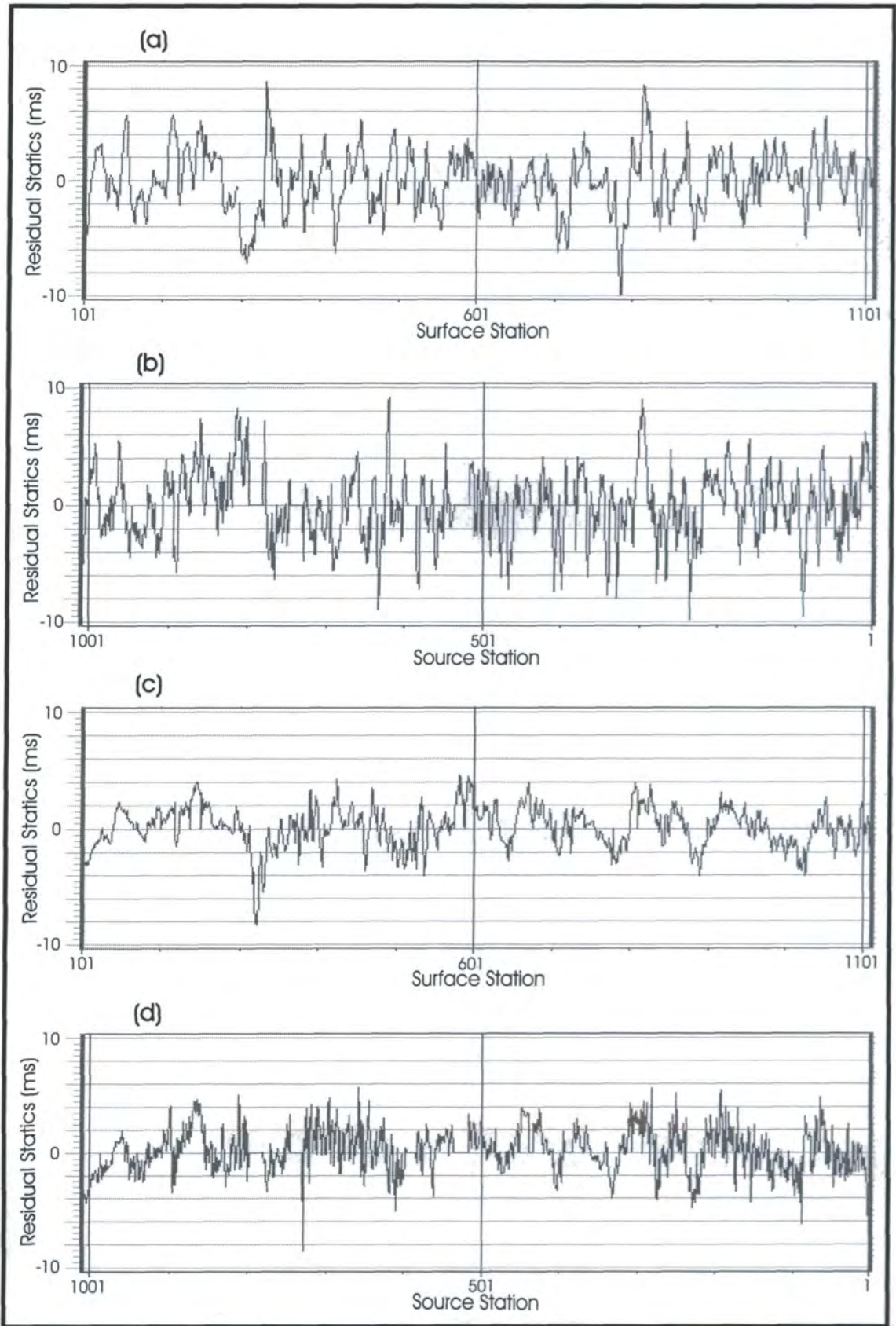


Figure 3.8. Constant velocity stacks with velocity function picked. For display purposes, only groups of seven CMPs (1343 - 1349) are shown.

There are currently ten automatic static processes available in ProMAX. All except “CDP Correlation Trim Statics” are surface-consistent solutions. The “Correlation Autostatics” process was applied in this case. This algorithm measures the relative time shifts of each of the traces from a common midpoint relative to a reference trace. When a static-shifted trace is cross-correlated with the reference trace, which is assumed to have no residual static, the location of the peak value of the correlation within the selected window gives an estimate of the time shift for that particular trace (Wiggins et al., 1976). The estimated time shift is then partitioned into source and receiver statics, a structural term and a residual moveout term using the Gauss-Seidel method. The input data required to carry out this process must be NMO-corrected CMP gathers.

In my processing, the reference trace is made up of traces from five CMP gathers, the data gate over which the ProMAX performs the correlation is from 0.60 to 1.80 s, and the maximum allowable source and receiver statics is 10 ms. This shift cannot be too large or cycle skipping may occur when cross-correlating. Four partitioning iterations were used. Before running this process, a horizon was picked on the stacked data along the centre of the specified gate. This was done interactively using the pick option within the “Trace Display”. Its aim is to remove the dip components between adjacent CMPs prior to summing CMPs together to form the reference trace.

The estimated source and receiver statics are shown in Figure 3.9. It is clear that the results from the second run with average estimates of  $\pm 2.0$  ms are much better than the first run. The general shapes of the second run profiles are quite similar with smaller residual static values compared to the first run. This emphasises the improvement in the residual statics solution. However, good consistency is sometimes missing, which I believe is due to source stations being offset from the line because of the rough



**Figure 3.9.** Summary of residual statics applied. (a) and (b) are the receiver and source residual statics from first run, respectively. (c) and (d) are the receiver and source residual statics from second run, respectively.

topography, or possibly due to poor source and receiver coupling.

In addition to autostatic solutions, the program also provides some other useful information, such as the correlation quality factors for each input trace (Figure 3.10). Quality factor of 1 corresponds to a maximum correlation between the input trace and the reference trace. Better correlation is achieved at the start and end of the line because fewer far-offset traces involved. A value of 0 indicates a low reliability in the computer estimated statics; this is clearly illustrated by the missing traces from the omitted source stations and dead geophone groups. In general, residual static estimates do change from good estimates for high signal to noise ratio data to poorer estimates as the ratio decreases.

### **3.10 Normal moveout corrections, trace muting, and stacking**

Having picked the velocity functions, the next step is to test these velocities and make sure that the best quality stack of signal is achieved. This was performed after the velocity functions obtained from the CVS (section 3.8) were spatially interpolated such that each CMP gather along the line had a stacking velocity function, and the application of “Normal Moveout Correction” to each of the individual traces in every CMP. Traces in each common midpoint are vertically stacked together via the “CDP/Ensemble Stack” process to yield one output trace per CMP. The method selected for scaling samples of equal travel time after stacking is to be divided by the square root of the number of traces involved. The square root scaling is chosen to avoid excessively strong amplitudes at early arrival times.

The normal moveout correction (NMO) is applied according to the following formula:

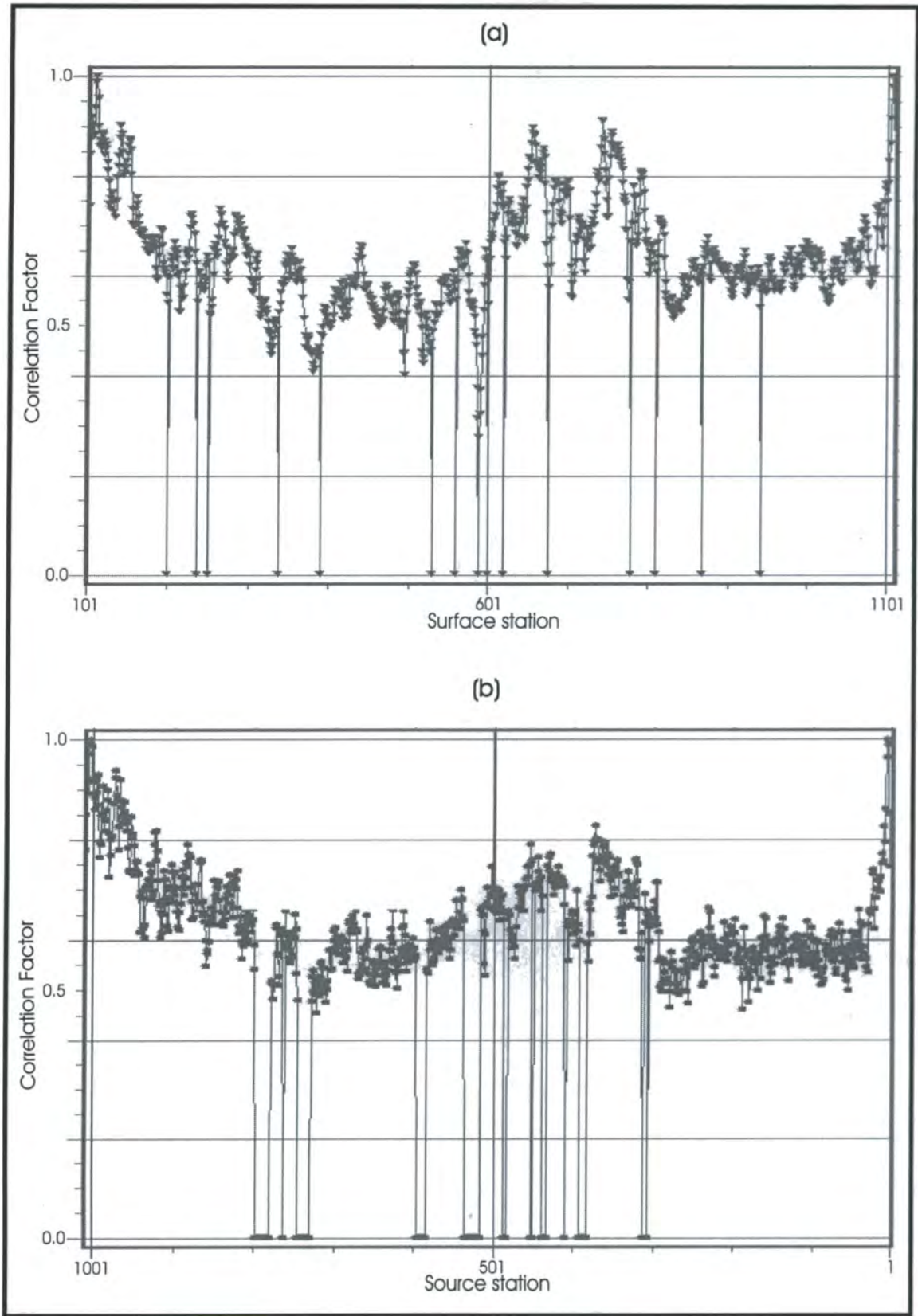


**Figure 3.10.** Correlation coefficients of input trace with the master trace.

$$T_x = \sqrt{\frac{X^2}{V^2} + T_0^2} \quad (3.1)$$

where  $T_x$  is the reflection time at offset  $X$ ,  $V$  is the stacking velocity,  $X$  is the source-receiver offset, and  $T_0$  is the reflection time at zero offset.

A mute function was picked on the “Screen Display” of the CMP gathers using the same tool used in designing the shot gather mute function in section 3.4.3. This function (top mute) was designed to suppress reflections on NMO-corrected CMP gathers from depths shallower than the offset, at all offsets.

The final stacked section with the full processing applied is enclosed in the back pocket of this thesis. According to information from well D7-NC149 near CMP 1044, the target horizon (top Nubian) is supposed to be at about 2000 ms two-way travel time. The deepest interpretable event seen on this section is the reflection event on the left-hand side at about 1800 ms two-way travel time (top Kalash). It depicts the general shape of the horst structure which forms the Wadi Field.

The second prominent event characterised by good continuity is the reflection from the Upper Eocene (top Harash formation). It runs across the section from at about 1150 ms on the left to almost the same level on the right. There is some indication of drape across the structure.

The shallow strong event is the reflection from the top of the Upper Eocene Gialo formation, at about 500 ms. The reflection response from the top of Muailah formation, which overlies the Gialo formation, is not shown by the stacked section due to the tight

mute function I have applied.

A summary of the processing and analysis sequence I carried out during this work is shown in Figure 3.11.

### **3.11 Summary**

The maximum number of traces per CMP gather included in the processing described above is 245 traces, i.e. the maximum fold of cover is only 245 fold and not 360 fold as was originally acquired in the field. The stacked sections produced with and without the far-offset traces (full fold of cover and 245 fold) using the same processing flows have shown negligible changes down to the target. This is because the mute function is cutting out reflected energy from the target at offsets greater than 4.0 km. A less severe mute would allow excessive NMO stretch at greater offsets. Also deployment of extra recording channels would involve more cost without any improvement in data quality.

Prestack attempts to enhance the signal to noise ratio have succeeded in suppressing the noise to a certain level, and in improving the reflection data quality for horizons younger than the Cretaceous strata (compare CMP gather in Figures 3.7 and 3.12).

The static corrections computed using weathering information from up-holes drilled above the scarp have resulted in a stacked section with better quality compared to the section obtained using the original field statics.

Although velocity picks were updated following the application of the residual statics corrections from the first run, residual statics have failed to improve the velocity analysis.

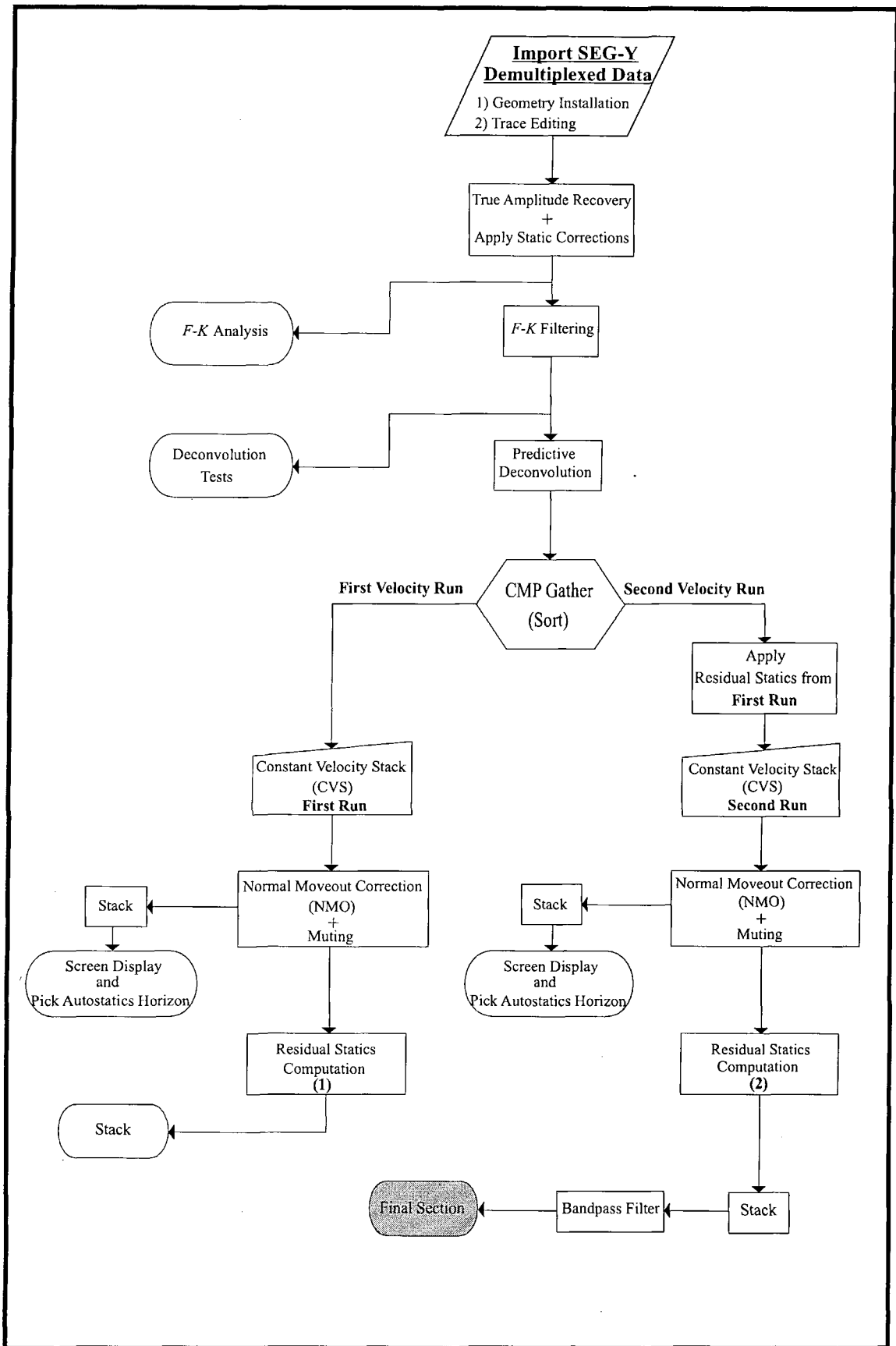
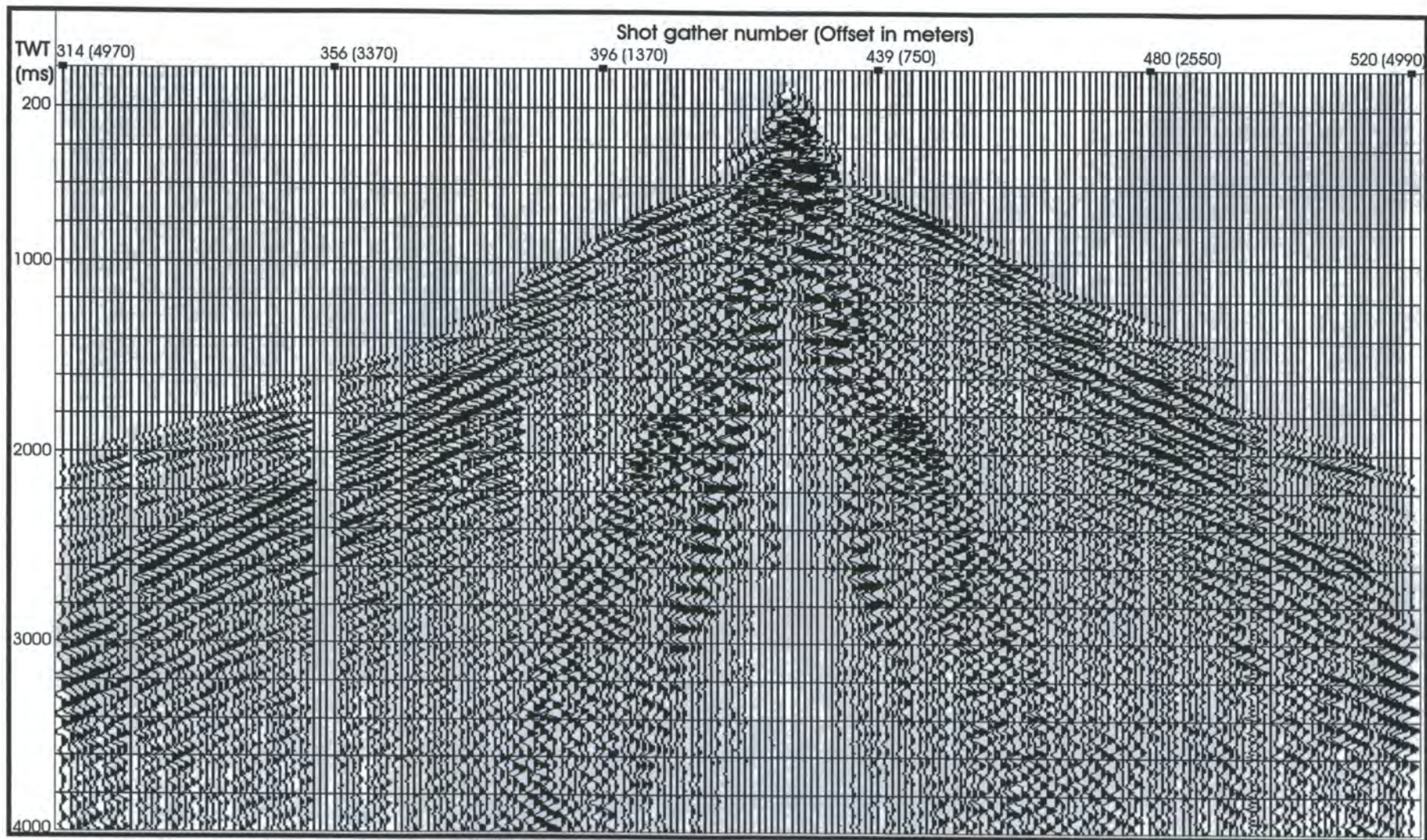


Figure 3.11. Flow-chart of the processing sequence carried out in ProMAX2D.



**Figure 3.12.** CMP 1346 (raw data), sorted before application of velocity filtering and predictive deconvolution to common-shot gathers. Static corrections and mute are applied.

The most effective process was the CMP stack. Unfortunately, this process has failed to produce any good data from reflectors beneath the Tertiary strata. The deepest reflector that can be seen on the stacked section with reasonable quality is the horizon between the Upper Cretaceous and the Tertiary (top Kalash horizon). It is obvious that processing cannot produce reflections from field data without signal. The failure of subsequent acquisition and processing trials, including the current processing, to improve the quality of the reflection data from the primary exploration target in the Wadi Field does not leave much room for more acquisition trials before understanding the actual cause of the problem. Lack of signal penetration into reflectors below the top Upper Cretaceous horizon seems to be a major contributor to the problem.

# CHAPTER FOUR

## One-dimensional synthetic seismograms

### 4.1 Introduction

The main objective of this study is to investigate the reasons for the poor signal returns from strata of Cretaceous age in seismic reflection sections from the Wadi field, Sirte Basin, Libya. The processed seismic sections are severely lacking in reflection information from reflectors beneath the top Cretaceous boundary, between the Upper Cretaceous Kalash formation and Lower Palaeocene Meem formation. The poor penetration of seismic energy makes it difficult to locate structures which could potentially contain hydrocarbon accumulations in the Nubian quartzitic sandstones, within the Lower Cretaceous. The top of the Nubian formation is at a depth of 11363 feet below the surface, 2441 feet below top Kalash. These depths are obtained from Well D7-NC149.

Over the past decade, Sirte Oil Company has acquired more seismic data in several surveys using different sets of recording parameters and advanced equipment. The latest survey was an experimental Vibroseis line acquired in early 1995, with 720 recording channels and a source point interval of 20 m. Apparently, no improvement has been achieved in the data quality over the exploration target (Figure 4.1). The suspected cause was lack of penetration due to the large variations in the acoustic impedance between the interbedded dolomites, shales and anhydrites in the Sirte formation, with most of the incident energy being reflected back to the surface and very little transmitted. In order to test the non-penetration hypothesis, I generated synthetic seismograms from well data to look at the effects of all multiples and transmission

Well D7-NC149

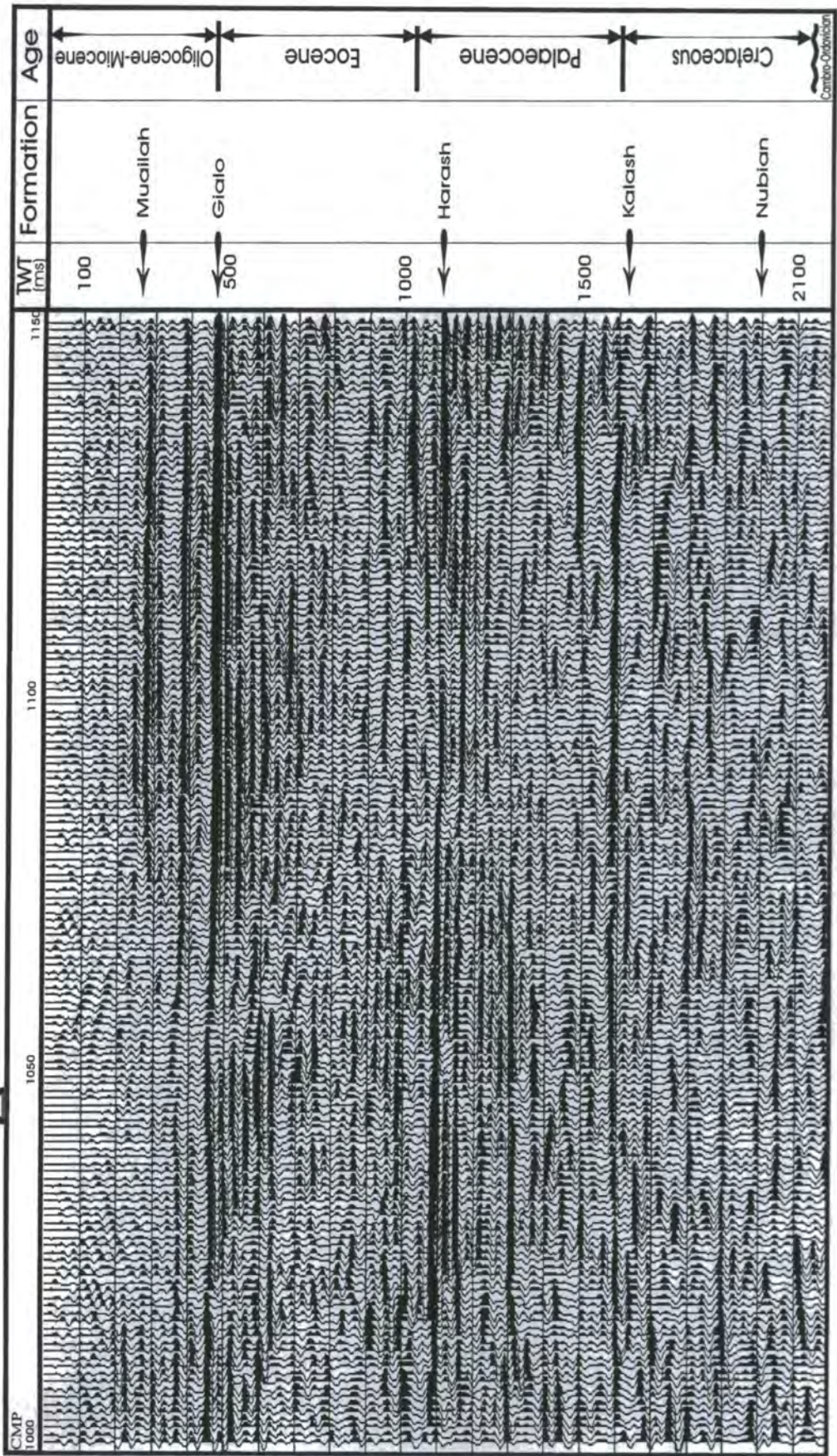


Figure 4.1. A portion of a CMP stack from the experimental line.

losses on the seismic reflection response from the sedimentary sequences above and within the target zone. For a more detailed description of factors affecting reflection amplitudes: reflection coefficients, transmission coefficients, multiple reflections, spherical divergence and absorption, see O'Doherty and Anstey (1971).

The generation of synthetic seismograms was accomplished by using Fortran programs written specifically for this purpose. Three different types of one-dimensional synthetic seismograms have been generated: primaries without transmission losses (reflection coefficient sequence) (Figure 4.2), primaries with transmission losses (Figure 4.3), and primaries with all multiples and transmission losses (Figure 4.4). The last of these is the plane-wave impulse response for a horizontally layered earth model. This was obtained by using the layer-matrix method described by Claerbout (1985) to calculate the reflection response of a layered system, as introduced by Goupillaud (1961). An impulsive plane-wave source is assumed to be normally incident on a model earth comprising a stack of horizontal layers of equal two-way travel time (2 ms in this case) sandwiched between two half-spaces. Anelastic effects (absorption) are not taken into consideration. Each of the three time sequences was convolved with the seismic wavelet shown in Figure 4.5 to obtain the respective synthetic seismograms. Later in this report, the primaries-only synthetic seismogram is compared with the processed trace on the experimental line 149V1211-95 at CMP 1044, near the well.

## **4.2 Derivation of the polynomial equations using the layer-matrix**

Consider a compressional plane wave of unit amplitude impinging at normal incidence on the boundary between layer  $k$  and layer  $k+1$  as shown in Figure 4.6.  $c_k'$  and  $t_k'$  are the reflection and transmission coefficients of interface  $k$  for the downward travelling

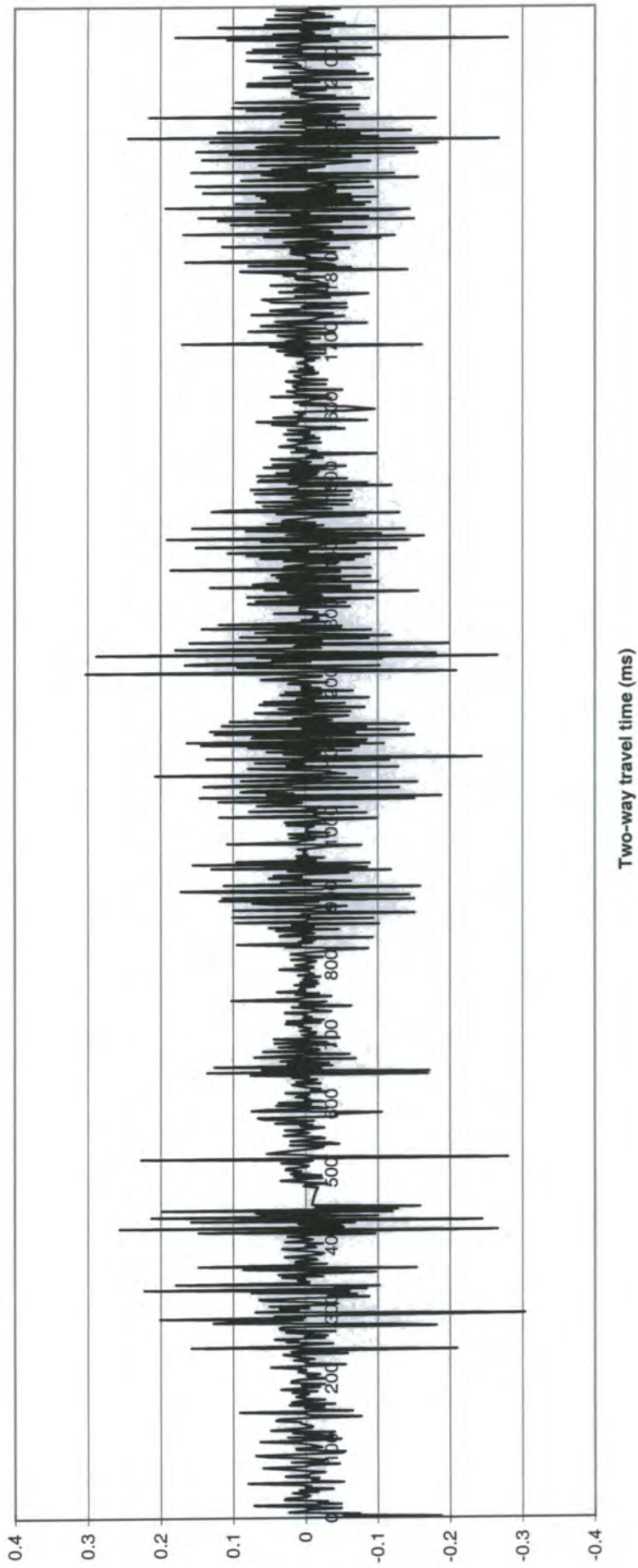
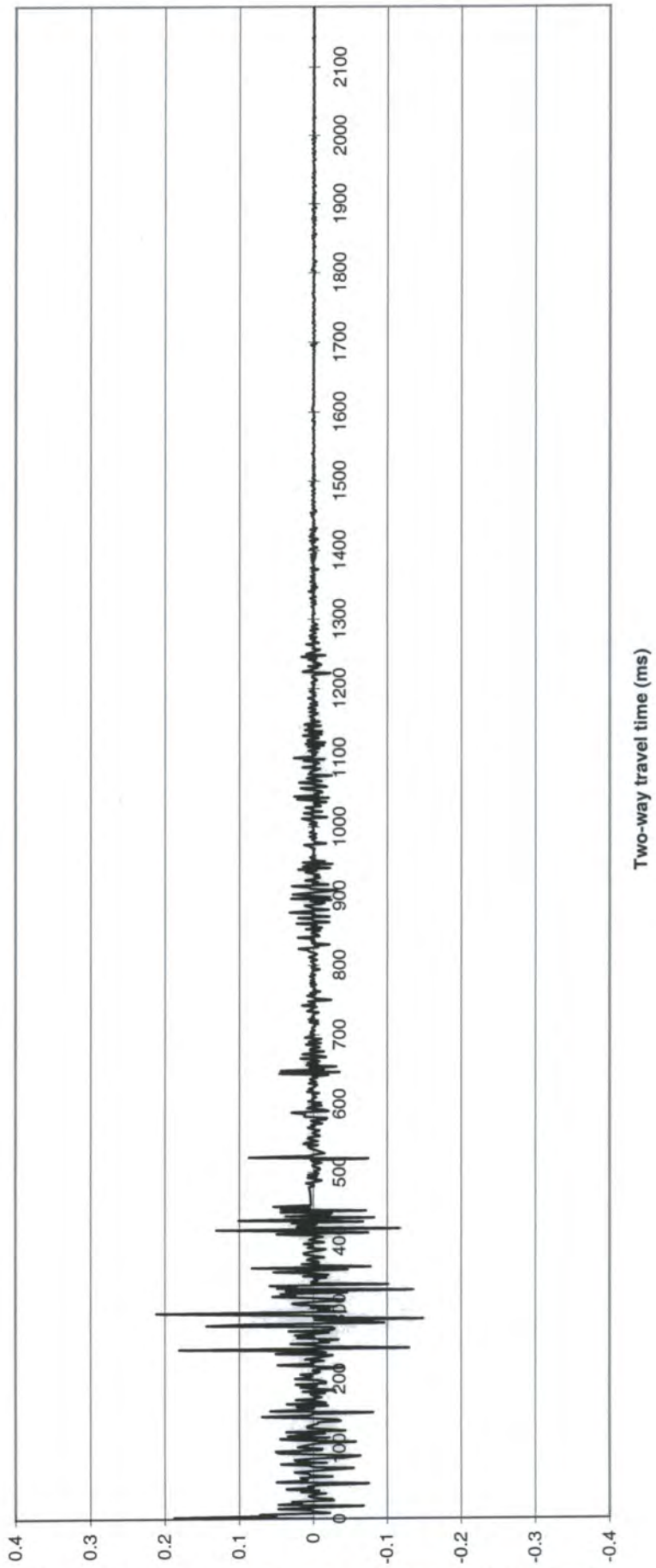
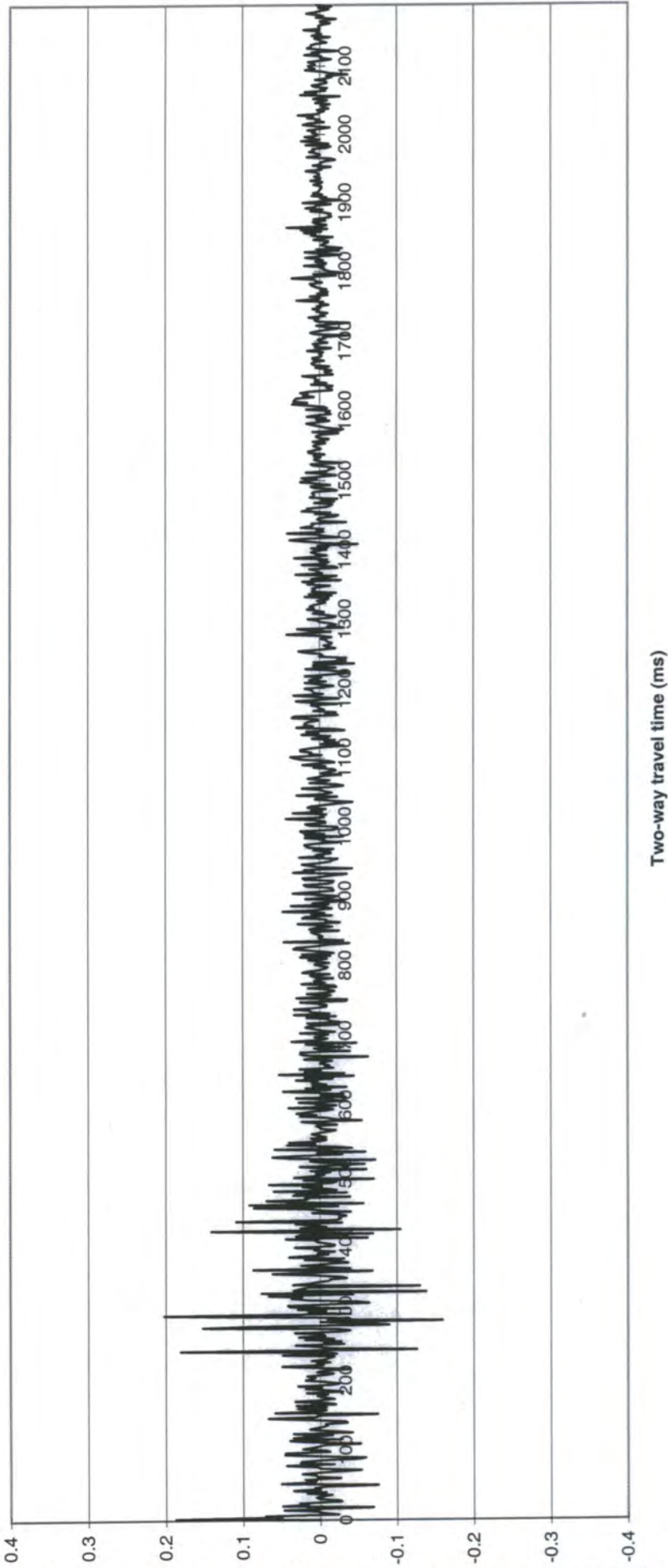


Figure 4.2. Primary reflection coefficient sequence.



**Figure 4.3.** Primary reflection response with the earth two-way transmission effects included.



**Figure 4.4.** Impulse response that includes primaries, transmission losses, and all possible multiples.

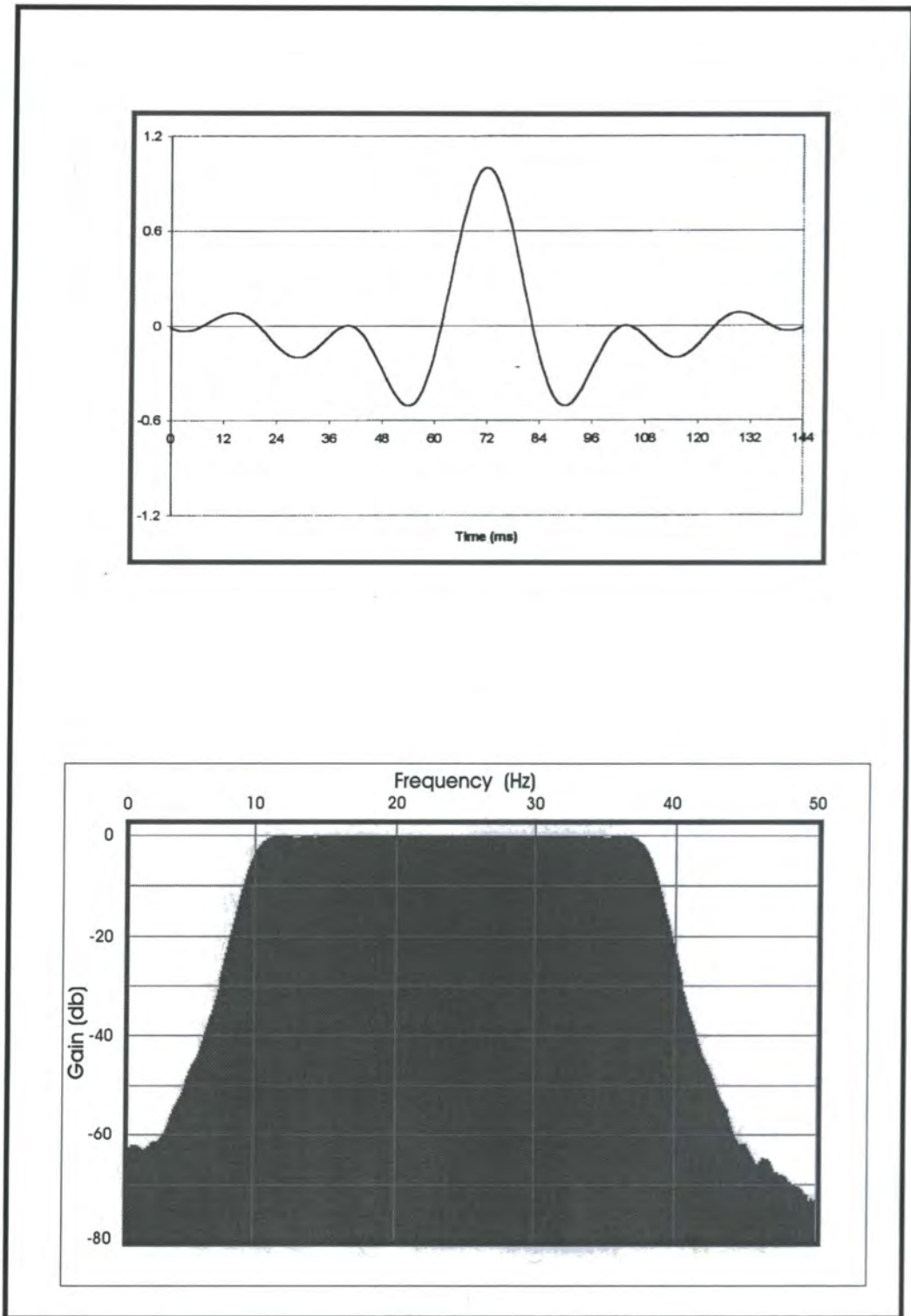


**Figure 4.5.** Klauder wavelet (8-40 Hz) and the amplitude spectrum of the sweep.

wavefields and  $c_k$  and  $t_k$  are their upward travelling counterparts, respectively.

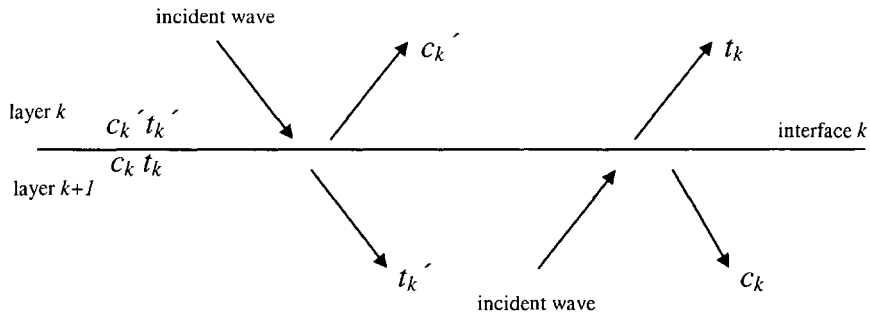


**Figure 4.6.** Reflection and transmission of a normally incident p-wave across interface  $k$ . Incident wave from above (left) and incident wave from below (right).

$$t_k' = 1 + c_k'$$

$$t_k = 1 + c_k$$

$$c_k = -c_k'$$

$D_k$  and  $U_k$  represent the Z-transforms of the downgoing and upgoing wavefields, respectively, at the top of layer  $k$  (Figure 4.7). Therefore, the downgoing wavefield  $D_k'$  at the bottom of layer  $k$  is the same wavefield as  $D_k$  delayed by a time equal to the one-way travel time in layer  $k$ . Similarly, the upgoing wavefield  $U_k'$  at the bottom of the same layer is  $U_k$  advanced by the same travel time. Thus

$$D_k' = D_k \sqrt{Z}$$

$$U_k' = \frac{1}{\sqrt{Z}} U_k$$

where  $Z$  is unit time delay operator. Each layer is assumed to have the same two-way travel time from one interface to the next, and this common two-way travel time in each layer is considered to be one unit of time. Hence, multiplying a function by  $Z$  means

delaying it by the two-way travel time across the layer, and multiplying it by  $\sqrt{Z}$  means delaying it by the one-way travel time across the layer.

These may be rearranged and written in matrix form as

$$\begin{bmatrix} U \\ D \end{bmatrix}'_k = \begin{bmatrix} 1/\sqrt{Z} & 0 \\ 0 & \sqrt{Z} \end{bmatrix} \begin{bmatrix} U \\ D \end{bmatrix}_k \quad (4.1)$$

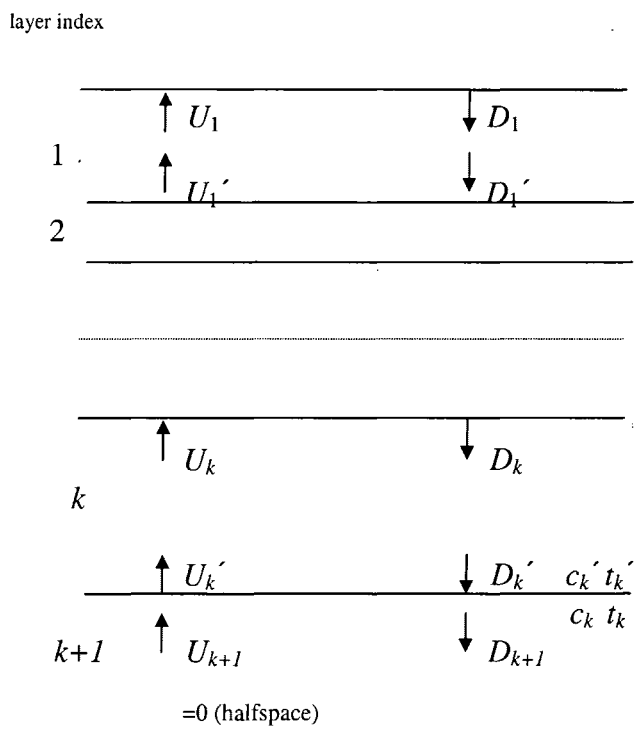


**Figure 4.7.** Downgoing ( $D$ ) and upgoing ( $U$ ) seismic wavefields in a layered medium of  $k+1$  layers and  $k$  interfaces.

Referring to the layered medium shown in Figure 4.7, which is essentially the Goupillaud layered system except that it is not necessarily being assumed here that the top of layer 1 is a free surface, the relationships between the downgoing and upgoing wavefields in terms of the reflection coefficients are obtained as follows:

$$U_k' = U_{k+1}t_k + D_k' c_k' \quad (4.2)$$

$$D_{k+1} = U_{k+1}c_k + D_k' t_k' \quad (4.3)$$

In order to get  $U_{k+1}$  and  $D_{k+1}$  on the right and  $U_k$  and  $D_k$  on the left equations 4.2 and 4.3 may be rearranged such that

$$-U_{k+1}t_k = -U_k' + D_k' c_k'$$

$$-U_{k+1}c_k + D_{k+1} = D_k' t_k'$$

and these may be written in matrix notation as

$$\begin{bmatrix} -t_k & 0 \\ -c_k & 1 \end{bmatrix} \begin{bmatrix} U \\ D \end{bmatrix}_{k+1} = \begin{bmatrix} -1 & c_k' \\ 0 & t_k' \end{bmatrix} \begin{bmatrix} U \\ D \end{bmatrix}_k'$$

Multiplying both sides by the inverse of the left-hand matrix

$$\frac{1}{-t_k} \begin{bmatrix} 1 & 0 \\ c_k & -t_k \end{bmatrix}$$

the result becomes

$$\begin{bmatrix} U \\ D \end{bmatrix}_{k+1} = \frac{1}{t_k} \begin{bmatrix} 1 & c_k \\ c_k & 1 \end{bmatrix} \begin{bmatrix} U \\ D \end{bmatrix}_k' \quad (4.4)$$

By substituting the right-hand expression in equation 4.1 into equation 4.4, this yields

$$\begin{aligned} \begin{bmatrix} U \\ D \end{bmatrix}_{k+1} &= \frac{1}{t_k} \begin{bmatrix} 1 & c_k \\ c_k & 1 \end{bmatrix} \begin{bmatrix} 1/\sqrt{Z} & 0 \\ 0 & \sqrt{Z} \end{bmatrix} \begin{bmatrix} U \\ D \end{bmatrix}_k \\ &= \frac{1}{t_k \sqrt{Z}} \begin{bmatrix} 1 & c_k Z \\ c_k & Z \end{bmatrix} \begin{bmatrix} U \\ D \end{bmatrix}_k \end{aligned} \quad (4.5)$$

The matrix in equation 4.5, relating the wavefields at the top of successive layers, is called the layer-matrix. The great advantage of this matrix is that a series of chain relationships can be written down for the upgoing and downgoing waves in the various

layers. This can be seen in a three-layer model (2 interfaces), by substituting equation 4.5 with  $k=1$  into the same equation with  $k=2$ :

$$\begin{aligned} \begin{bmatrix} U \\ D \end{bmatrix}_2 &= \frac{1}{t_1\sqrt{Z}} \begin{bmatrix} 1 & c_1Z \\ c_1 & Z \end{bmatrix} \begin{bmatrix} U \\ D \end{bmatrix}_1 \\ \begin{bmatrix} U \\ D \end{bmatrix}_3 &= \frac{1}{t_2\sqrt{Z}} \begin{bmatrix} 1 & c_2Z \\ c_2 & Z \end{bmatrix} \begin{bmatrix} U \\ D \end{bmatrix}_2 = \frac{1}{t_2\sqrt{Z}} \begin{bmatrix} 1 & c_2Z \\ c_2 & Z \end{bmatrix} \times \frac{1}{t_1\sqrt{Z}} \begin{bmatrix} 1 & c_1Z \\ c_1 & Z \end{bmatrix} \begin{bmatrix} U \\ D \end{bmatrix}_1 \\ &= \frac{1}{t_1t_2\sqrt{Z^2}} \begin{bmatrix} 1+c_1c_2Z & c_1Z+c_2Z^2 \\ c_2+c_1Z & c_1c_2Z+Z^2 \end{bmatrix} \begin{bmatrix} U \\ D \end{bmatrix}_1 \end{aligned} \quad (4.6)$$

Extending this to a model with  $k+1$  layers gives

$$\begin{bmatrix} U \\ D \end{bmatrix}_{k+1} = \frac{1}{\prod_{i=1}^k t_i\sqrt{Z^k}} \begin{bmatrix} F_k(Z) & G_k^R(Z) \\ G_k(Z) & F_k^R(Z) \end{bmatrix} \begin{bmatrix} U \\ D \end{bmatrix}_1 \quad (4.7)$$

where  $F_k^R(Z)$  and  $G_k^R(Z)$  are the reverses of  $F_k(Z)$  and  $G_k(Z)$ , respectively, defined as

$$F_k^R(Z) = Z^k F_k(Z^{-1}) = f_{k-1}Z + \dots + f_0Z^k \quad (4.8a)$$

$$G_k^R(Z) = Z^k G_k(Z^{-1}) = g_{k-1}Z + \dots + g_0Z^k \quad (4.8b)$$

Rewriting equation 4.7 with  $k+1$  replaced by  $k$  and substituting into equation 4.5 yields

$$\begin{aligned} \begin{bmatrix} U \\ D \end{bmatrix}_{k+1} &= \frac{1}{t_k\sqrt{Z}} \begin{bmatrix} 1 & c_kZ \\ c_k & Z \end{bmatrix} \times \frac{1}{\prod_{i=1}^{k-1} t_i\sqrt{Z^{k-1}}} \begin{bmatrix} F_{k-1}(Z) & G_{k-1}^R(Z) \\ G_{k-1}(Z) & F_{k-1}^R(Z) \end{bmatrix} \begin{bmatrix} U \\ D \end{bmatrix}_1 \\ &= \frac{1}{\prod_{i=1}^k t_i\sqrt{Z^k}} \begin{bmatrix} F_{k-1}(Z) + c_k Z G_{k-1}(Z) & G_{k-1}^R(Z) + Z c_k F_{k-1}^R(Z) \\ c_k F_{k-1}(Z) + Z G_{k-1}(Z) & c_k G_{k-1}^R(Z) + Z F_{k-1}^R(Z) \end{bmatrix} \begin{bmatrix} U \\ D \end{bmatrix}_1 \end{aligned} \quad (4.9)$$

By matching the 2 x 2 matrices in equations 4.7 and 4.9, we obtain the recurrence relations

$$F_k(Z) = F_{k-1}(Z) + c_k Z G_{k-1}(Z) \quad (4.10a)$$

$$G_k(Z) = c_k F_{k-1}(Z) + Z G_{k-1}(Z) \quad (4.10b)$$

From the recurrence relations (the polynomial build-up equations) and the left column in equation 4.6, it may be noted that the first coefficients of  $F(Z)$  and  $G(Z)$  are 1 (which is always the case) and  $c_k$  (equal to  $c_1$  for  $k=1$ ), respectively, and the highest coefficients are  $c_1 c_k$  and  $c_1$ , respectively. These may be summarised

$$F_k(Z) = 1 + f_1 Z + f_2 Z^2 + f_3 Z^3 + \dots + c_1 c_k Z^{k-1} \quad (4.11a)$$

$$G_k(Z) = c_k + g_1 Z + g_2 Z^2 + g_3 Z^3 + \dots + c_1 Z^{k-1} \quad (4.11b)$$

Now the reflection impulse response  $C(Z)$  can be obtained by substituting in the general matrix (equation 4.7), assuming that a plane-wave source of unit amplitude impinges at normal incidence on the model earth shown in Figure 4.8. This model earth is exactly the same as Figure 4.7 with the reflection coefficient at the top of layer 1 set to zero, assuming that the incident wave is from below. Thus  $U_{k+1}$  is set equal to unity and  $D_1$  is set equal to zero as no energy returns from the upper half-space in equation 4.7:

$$\begin{bmatrix} 1 \\ C(Z) \end{bmatrix} = \frac{1}{\prod_{i=1}^k t_i \sqrt{Z^k}} \begin{bmatrix} F_k(Z) & G_k^R(Z) \\ G_k(Z) & F_k^R(Z) \end{bmatrix} \begin{bmatrix} T(Z) \\ 0 \end{bmatrix}$$

This pair of equations may be written out explicitly as

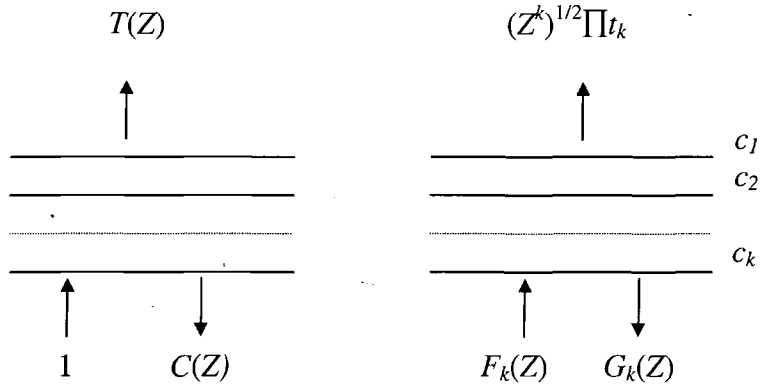


**Figure 4.8.** Reflected and transmitted seismic waves from layered medium confined between two half spaces.

$$1 = \frac{1}{\prod_{i=1}^k t_i \sqrt{Z^k}} \times F_k(Z) T(Z) \quad (4.12)$$

$$C(Z) = \frac{1}{\prod_{i=1}^k t_i \sqrt{Z^k}} \times G_k(Z) T(Z) \quad (4.13)$$

By solving equation 4.12 and equation 4.13 for  $T(Z)$  and  $C(Z)$  the following relation is obtained

$$C(Z) = \frac{G_k(Z)}{F_k(Z)} \quad (4.14)$$

In order to model surface seismic data, with the incident wave from above, the reflection coefficients must be redefined in reverse order with opposite polarity.

### 4.3 Well data available

The well log data used in this study were obtained from well D7-NC149. The well is located 55 m northwest of CMP 1044 (shot point 522) on the experimental line 149V1211-95. It was bottomed in Cambro-Ordovician strata at a depth of 13073 feet

below the Kelly Bushing, which was at an elevation of 18 feet above the ground surface. The actual well data comprise a continuous sonic velocity log, and the check-shot picks. No density log information is available.

The sonic data were supplied in both analogue display form and digital format (ASCII file). The sonic data were edited, and digitised using the Digi-Rat software package with a sampling interval of one foot. The digitised data cover the depth range from 299 feet to 13049 feet below the Kelly Bushing.

#### 4.4 Computing reflection coefficients from sonic log

The computation of the reflection coefficients had to be based on the sonic data alone since the density log was not available. The density was assumed to be constant throughout the section. With this assumption, reflection coefficients are calculated from the knowledge of velocities provided by the sonic log. The reflection coefficient  $c_k'$  for particle velocity (or displacement) when the incident ray is normal to the interface is given by:

$$c_k' = (V_k \rho_k - V_{k+1} \rho_{k+1}) / (V_k \rho_k + V_{k+1} \rho_{k+1}) \quad (4.15)$$

where

$\rho_k, \rho_{k+1}$  are the densities on the incidence and transmission sides of the interface, respectively, and  $V_k, V_{k+1}$  are the velocities on the incidence and transmission sides of the interface, respectively.

With the assumption of constant density, the reflection coefficient becomes

$$c_k' = (V_k - V_{k+1}) / (V_k + V_{k+1}) \quad (4.16)$$

In order to calculate the synthetic seismograms with reference to the same datum as the real data, it was necessary to adjust the sonic data to the same datum (base of weathering at 322 feet below the surface) as the processed experimental line. This was done at an early stage by excluding the top 37 feet from the sonic information before any reflection coefficient computations were carried out (Figure 4.9). A spread sheet program was used to compute the interval velocities (reciprocal of transit-time) and also to calculate the integrated sonic time by summing the interval transit times.

Calibration of the sonic data by correcting the integrated sonic log times according to the well-velocity survey has been neglected, since the calibrated sonic resulted in a non-consistent mis-tie (maximum shift is 70 ms two-way time) between the synthetic seismograms and the processed section. The base of the weathering layer (datum plane) is 78 m above mean sea level, and the sub-weathering velocity is 2150 m/s, these figures having been obtained from five up-holes drilled along the experimental line. As a result, the two-way travel time in the sub-weathering layer above mean sea level should be 73 ms and not 139 ms as shown by the sonic log after calibration with the well velocity survey. This emphasises that there is something wrong with the picked travel times from the well-velocity survey.

The integrated sonic times and the corresponding interval velocities for successive depths at one foot intervals (variable time intervals) were input to the GMT program, sample1d, to sample the interval velocities as a function of time. The program slices the integrated sonic log into layers of equal two-way travel time (2 ms) (Wuenschel, 1960). It is necessary to start sampling from 1 ms two-way time with an increment of 2 ms in order to obtain the reflection coefficient sequence for interfaces beginning at zero time. The reflection coefficient sequence with vertical scale in units of two-way travel time is

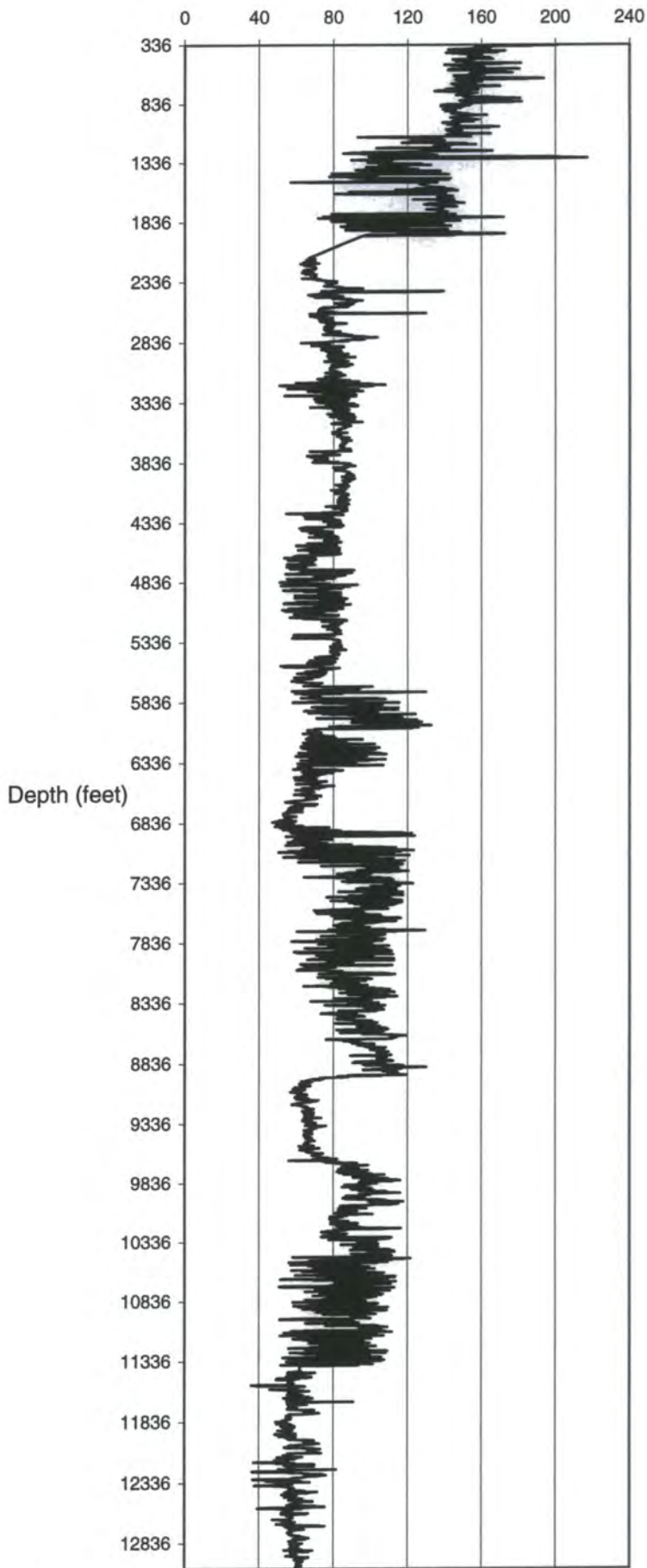


**Figure 4.9.** Sonic log from well D7-NC149. Horizontal scale is in micro-seconds per foot.

shown in Figure 4.2. The first reflection coefficient at  $t = 0$  is zero. These results represent the foundation of the current work.

## 4.5 Seismic source wavelet

A Vibroseis 10 s linear sweep over the frequency band 8-40 Hz with 250 ms tapers was generated, auto-correlated, and sampled at the same time interval as the reflection coefficient sequence (2 ms) by using ProMAX2D. The constructed Klauder wavelet  $w(t)$  (73-points) and the amplitude spectrum of the sweep are shown in Figure 4.5.

## 4.6 Synthetic seismograms

### 4.6.1 Synthetic seismogram without multiples and transmission losses

The computation of a multiple-free synthetic seismogram is particularly simple as it concerns only those events that reflected once from each interface separating layers with different acoustic impedance (i.e. the primaries) without taking into consideration the effects of the transmission losses. This seismogram is actually the convolution of the reflection coefficient sequence  $c$  with the seismic wavelet of Figure 4.5. The whole operation is performed using a Fortran program written for the convolution of two transient signals. The result is shown in Figure 4.10. The same convolution program is used to compute the remaining seismograms for the different input time sequences. The formula for the convolution of the reflection coefficient sequence  $c$  of length  $(m+1)$  with the seismic wavelet  $w$  of length  $(n+1)$  is:

$$x_t = \sum_{s=0}^t c_s w_{t-s} \quad (4.17)$$

where  $x$  is the noise-free synthetic seismogram without multiples and transmission losses, of length  $m+n+1$ , and  $t$  is the time index.

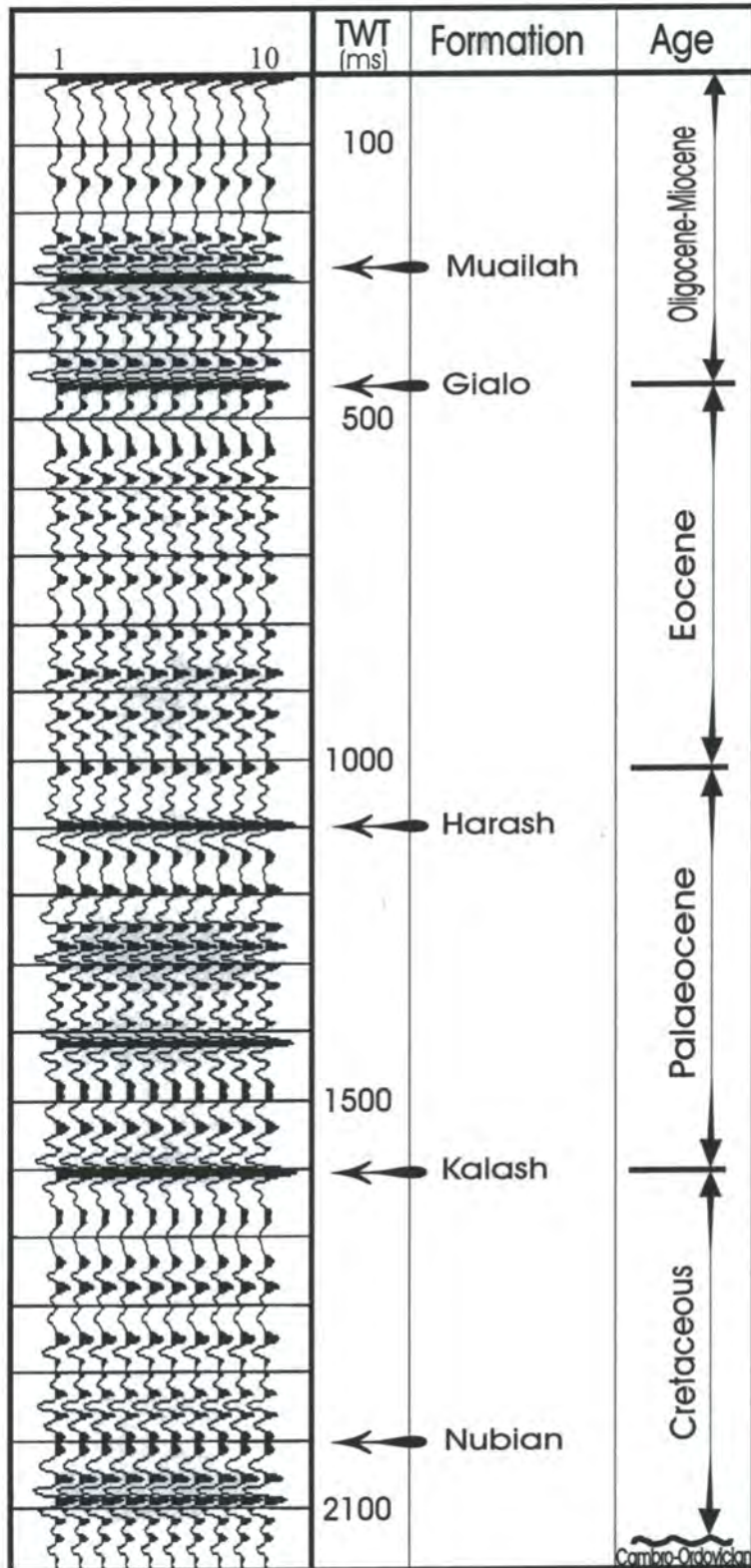


Figure 4.10. Synthetic seismogram with primaries alone.

#### 4.6.2 Synthetic seismogram with primaries and transmission losses

For this seismogram, transmission coefficients are involved in addition to the interface reflection coefficients. The transmission effect takes place when the seismic pulse passes through an interface separating two different rock types, part of the incident energy being lost from the transmitted signal due to reflection at the interface. The transmitted part is partly reflected back from deeper reflectors and on its return path must pass through the same interfaces, and experience more attenuation.

The two-way transmission coefficient for an interface is  $1-c^2$ , where  $c$  is the reflection coefficient of the interface. The two-way transmission coefficient is unaffected by the reflection coefficient sign. The amplitude of a primary reflection event from a particular interface is the product of all two-way transmission coefficients for interfaces above it and its own reflection coefficient. Thus for the  $k$ th interface, the reflected amplitude with transmission losses is given by:

$$r_k = c_k \prod_{i=1}^{k-1} (1 - c_i^2) \quad (2.18)$$

To compute the plane-wave primaries-only impulse response with the transmission effects included, the reflection coefficients were modified as given by equation 2.18. The synthetic trace was then obtained by convolving the impulse response (Figure 4.3) by the same wavelet used in the last section. The result is plotted in Figure 4.11.

#### 4.6.3 Synthetic seismogram with multiples and transmission losses

In this case, primaries, all possible multiples and transmission losses are included Wuenschel (1960). Multiple reflections are divided into two categories based on their periodicities: long period multiples and short period or 'peg-leg' multiples as illustrated by the examples in Figure 4.12. Although all multiples are generally designated as

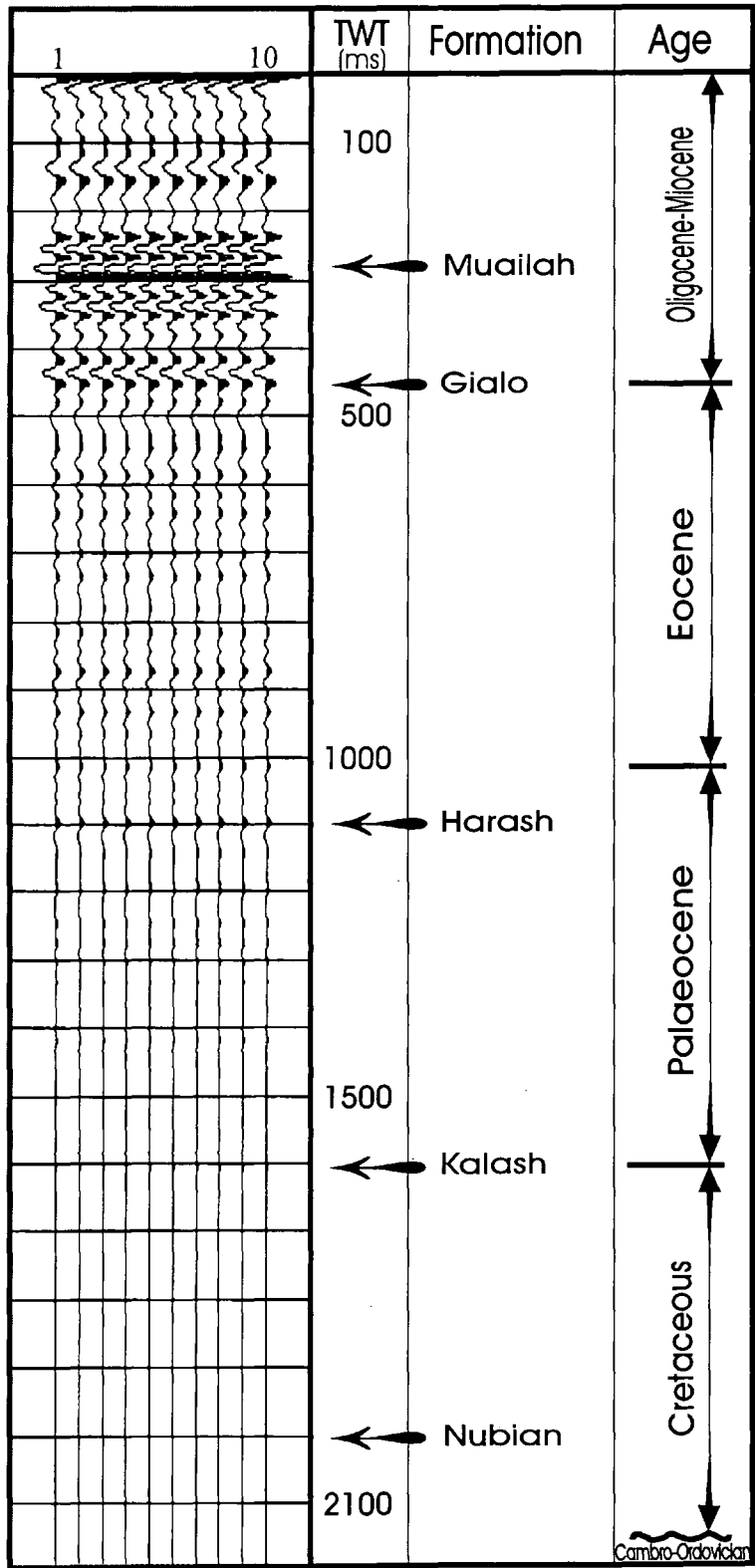
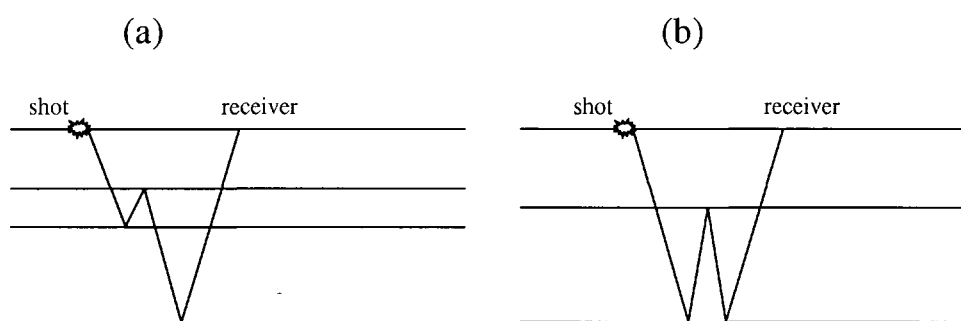


Figure 4.11. Synthetic seismogram with primaries and transmission losses.

noise, short period multiples are useful because of their significant contributions in reinforcing the direct transmitted signal. Without them, primaries would often be undetectable at later travel times due to transmission losses. The composite transmission effect of short period multiple reflections in thin beds is to reinforce strongly, and delay slightly, the primary reflection events, and this effect becomes more pronounced for deeper reflectors (Anstey 1960).

The seismogram shown in Figure 4.13 is the result of the convolution of the earth's plane-wave impulse response (Figure 4.4) with the seismic wavelet. The earth's impulse response  $C(Z)$  is computed using a Fortran program written for the polynomials  $F(Z)$  and  $G(Z)$  (Section 4.2, equations 4.10a and 4.10b), and their ratio (equation 4.14).



**Figure 4.12.** Examples of first order multiples: (a) a short-period raypath; (b) a long-period raypath.

#### 4.6.4 Synthetic seismograms with near-surface included

The synthetic seismograms generated in this step are similar to those in sections 4.6.1 and 4.6.3 except that the contributions of the free-surface and the layering within the zone of weathering are included. Weathering velocities were considered to be constant within each layer in this zone since the near-surface properties were not known in detail. As a result, reflection coefficients are computed for the interfaces which separate the

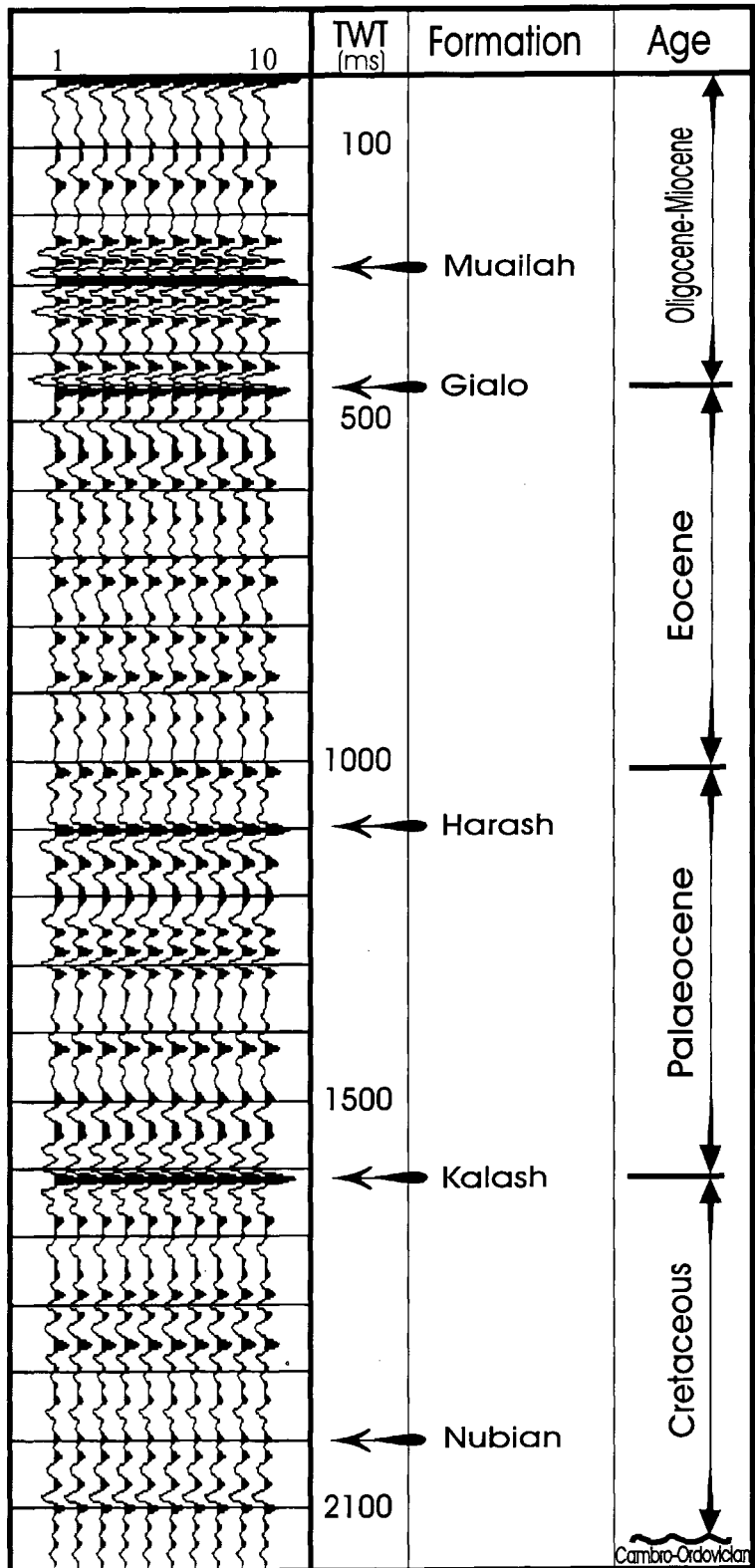
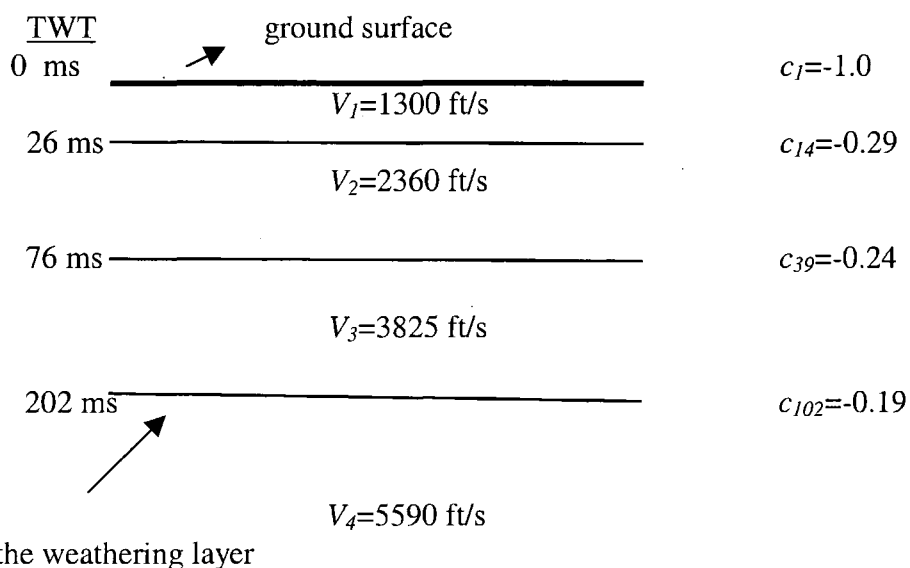


Figure 4.13. Complete synthetic seismogram.

weathering zone layers at the well location using the near-surface information (Figure 4.14) obtained from the nearby up-holes. The obtained reflection coefficients for the near-surface boundaries have then to be added to the reflection coefficient series computed from the sonic data. A value of -1.0 has also been assigned to the reflection coefficient of the air/ground interface.

The earth's impulse response has been computed for the sequence from the ground surface down to the bottom of the well by using Robinson's (1983) program. The program was originally written to compute a synthetic seismogram and, in addition, the upgoing and downgoing waves at each level. In this study I was interested only in computing synthetic seismograms. Therefore, I have removed the part which calculates the upgoing and downgoing waves. Because of the large number of interfaces involved, the second part requires a lot of memory and computer time.



**Figure 4.14.** A simple diagram showing the weathering zone parameters: two-way travel times, velocities and reflection coefficients. Information for interfaces below the base of the weathering zone was obtained from the sonic log.

## 4.7 Results and discussion

### 4.7.1 Effects of transmission losses and multiples

The purpose of these investigations was to evaluate the effect of transmission losses on the primary reflected events, to determine the importance of the multiple reflections in the restoration of those losses, and to understand how the processes of acoustic reflection and transmission affect the recorded seismic reflection data in the Wadi field in general, and from the exploration target in particular.

It is obvious from the comparison of Figures 4.10 and 4.11 that the cascaded transmission effect through numerous interfaces (1095 interfaces) is certainly not negligible. The deepest recognisable event after the transmission effect has been taken into consideration is the one from the Upper Palaeocene (top Harash) at 1100 ms two-way travel time, trailed by minute deflections which gradually decay away to almost nothing in the region between top Kalash and the target zone. The progressive attenuation of the primaries emphasises the importance of multiples in seismic energy transmission through deep layering.

Figure 4.13 shows the combined effects of the transmission losses and all multiple paths on the reflected amplitudes. The inclusion of multiple reflections has introduced enormous changes compared to the synthetic seismogram for primaries with transmission losses (Figure 4.11) with increased amplitudes and progressively large delays for the reflected events corresponding to deeper horizons. These alterations are clearly depicted by the composite plot in Figure 4.15. Transmission losses lower primary seismic signal amplitudes uniformly at all frequencies, and the rate of reduction varies down the geological section. Short-period multiples in thin beds tend to compensate for these losses in a frequency-dependent manner. Each thin bed has a

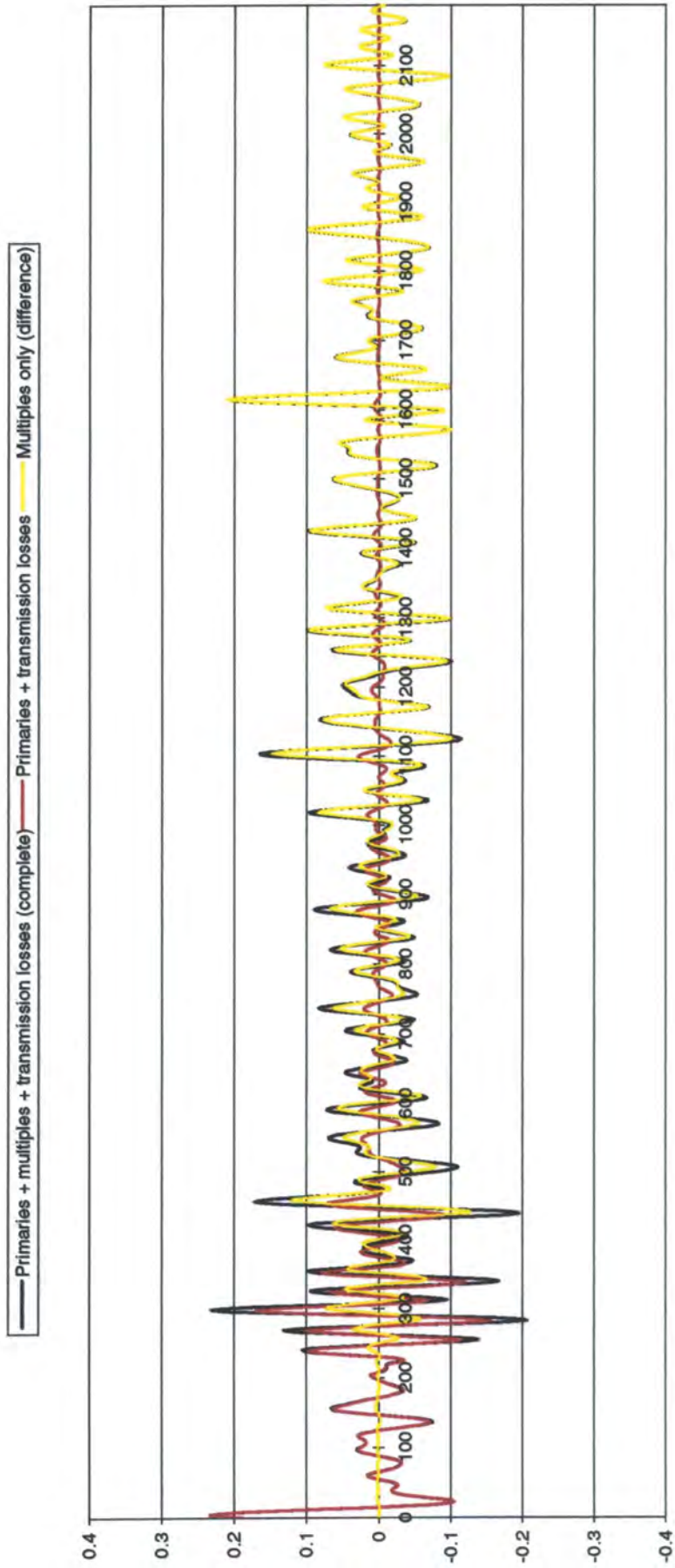


**Figure 4.15.** Composite plot illustrates the effect of the long-period and short-period multiples on the primary reflections.

greater reflection response at high frequencies and a greater transmission response at low frequencies. Consequently, the amplitude spectrum of the complete synthetic seismogram shifts towards lower frequencies with increasing travel time (Schoenberger and Levin, 1974).

The contributions of the multiples to the reflection amplitudes are progressively more important with depth (compare the top Muailah, top Gialo, top Harash and top Kalash events in Figures 4.11 and 4.13). Multiples contribute overwhelmingly to the reflection amplitudes from the vicinity of the target horizon at 2006 ms. In the Tertiary, where the strata comprise thick layers with steady gradations of velocity, the short period multiples have succeeded in getting the top Kalash event to stand out strongly above the background noise (long period multiples). This happened because the reflection coefficients within formations in this section are relatively small, and so are the respective transmission losses. Nevertheless, phase shifts have been caused by the peg-leg multiples that are generated in the thin layers; they increase from zero initially to about 90 degrees at top Kalash.

In the Sirte formation the stratification is a cyclic pattern of sedimentation of thin layers (minimum thickness 2 feet) with a great number of interfaces between beds with alternating high and low velocity. As a result, peg-leg multiples have apparently failed to produce sufficient penetration of signal to the horizons below the top Kalash horizon.

The reflection response from the Nubian formation between 2000 ms and 2100 ms in the complete synthetic seismogram (Figure 4.13) does not match the character of the synthetic seismogram for the primary events alone (Figure 4.10). This observation suggests that the complete synthetic seismogram is dominated by long-period multiples

at the target.

#### 4.7.2 Investigations using the conventional seismic bandwidth

In order to ascertain whether the seismic event from the top Kalash horizon (Figure 4.13) is a real primary event or just long period multiples generated in the sequence above, another synthetic seismogram was computed (middle panel in Figure 4.16). This is the complete one-dimensional synthetic seismogram for the reflectivity sequence from the base of the weathering down to 1550 ms, but not including the top Kalash event itself: i.e., constant velocity from 1550 ms down to the bottom of the hole. All the events in this synthetic below 1550 ms represent multiple reflections which were generated in layers above the top Kalash. To get an estimate of signal amplitude of top Kalash event, this synthetic seismogram was subtracted from the complete synthetic seismogram shown in the same figure. It is quite evident from the difference seismogram (right-hand panel) that the majority ( $\approx 75\%$ ) of the reflected amplitude from the top Kalash horizon is contained in the primary reflections (including peg-leg multiples), and the rest is comprised of long-period multiples which interfere constructively with the primary at the top Kalash two-way travel time as shown in Figure 4.17.

The same procedure was repeated for the top Nubian event. This time the synthetic seismogram (middle panel in Figure 4.18) was computed for the reflectivity sequence from the base of the weathering down to 1950 ms, but not including the top Nubian. The difference seismogram (right-hand panel) represents the primary reflection events with their associated multiples for reflection coefficients with two-way travel time greater than 1950 ms. This is also illustrated by the composite plot in Figure 4.19. It is obvious that the primary event from top Nubian at 2006 ms has much weaker amplitude than the

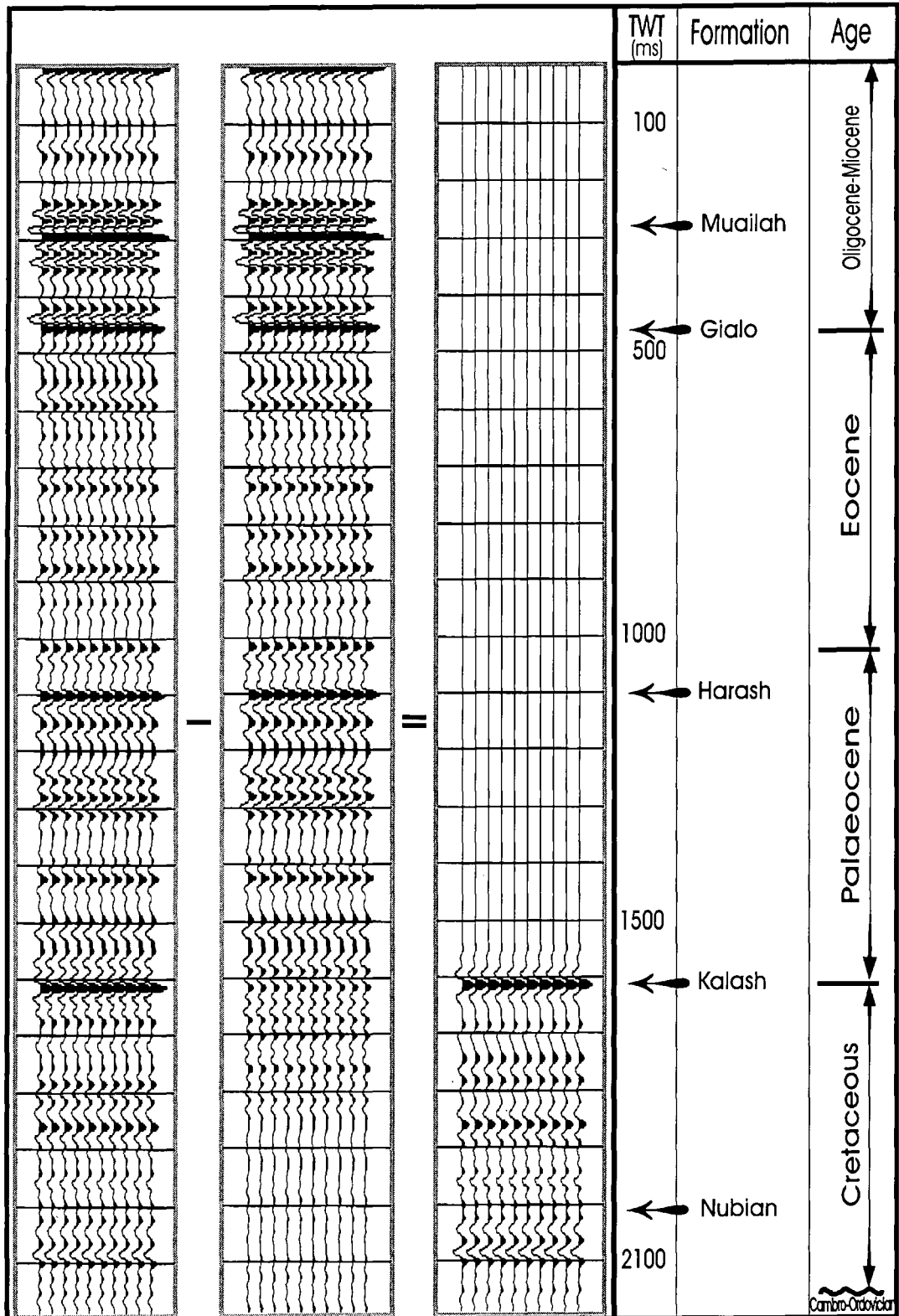


**Figure 4.16.** Left panel is complete seismogram obtained by the convolution of the earth's impulse response with the source wavelet (8-40 Hz), middle panel is complete seismogram down to 1550 ms (interval velocity was assumed to be constant below 1550 ms), and right panel is the difference, which demonstrates the primary seismic event at top Kalash.

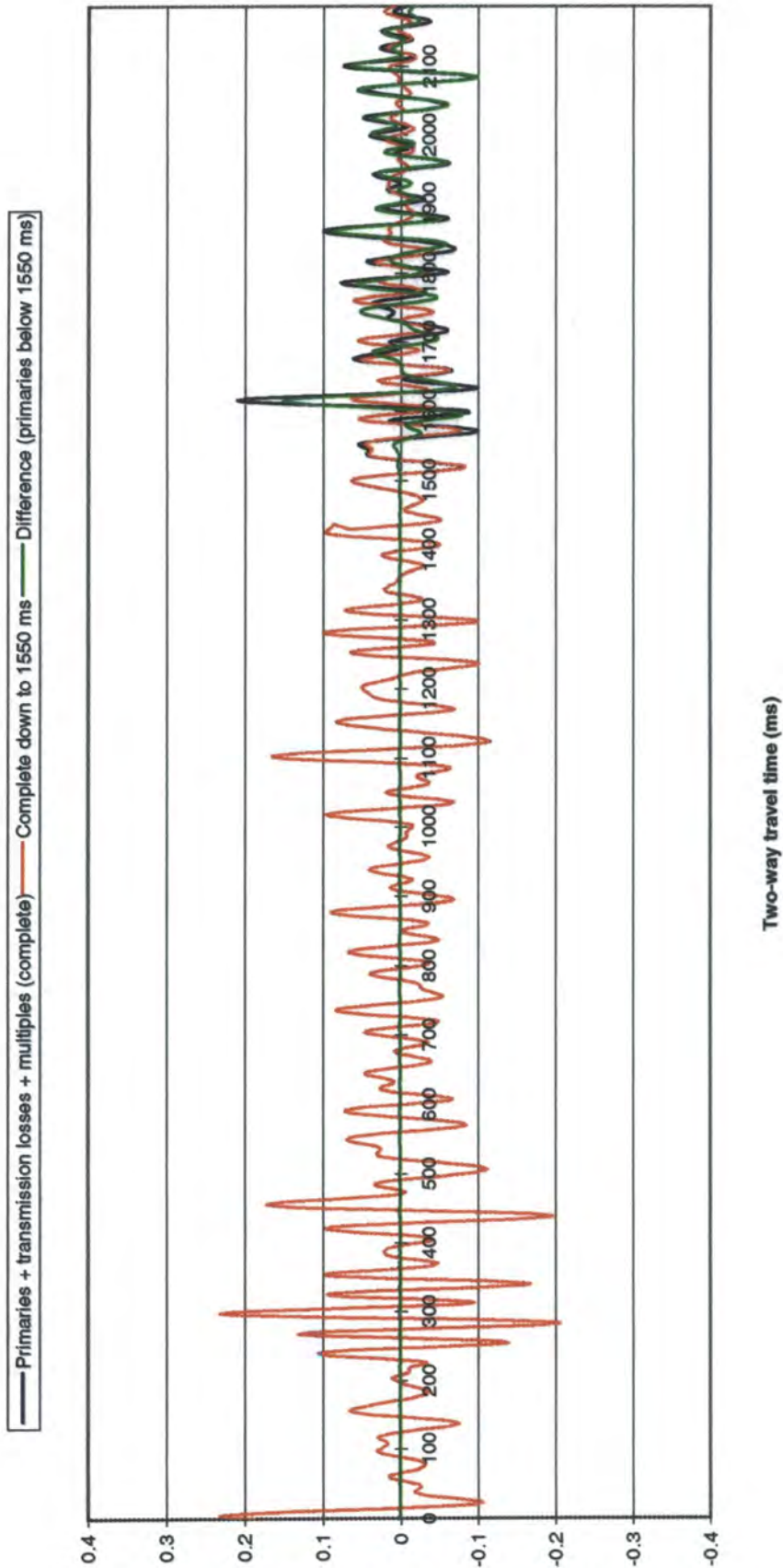


**Figure 4.17.** Composite plot illustrates the effect of the long period multiples on the primary reflection signal from top Kalash. The blue and the orange traces are overlapped in the area above 1550 ms.

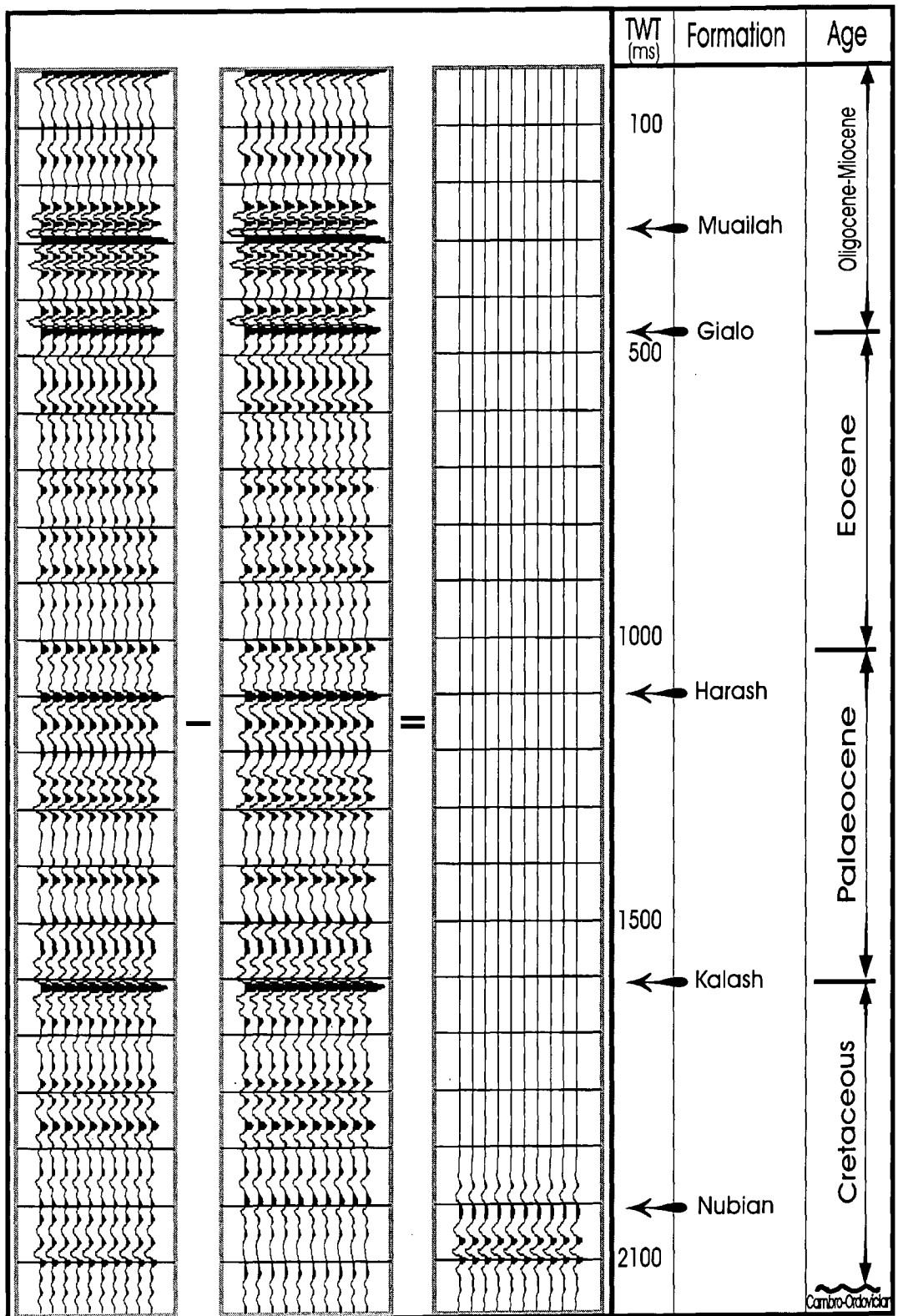


**Figure 4.18.** Left panel is complete seismogram obtained by the convolution of the earth's impulse response with the source wavelet (8-40 Hz), middle panel is complete seismogram down to 1950 ms (interval velocity was assumed to be constant below 1950 ms), and right panel is the difference, which demonstrates the primary seismic event at top Nubian.

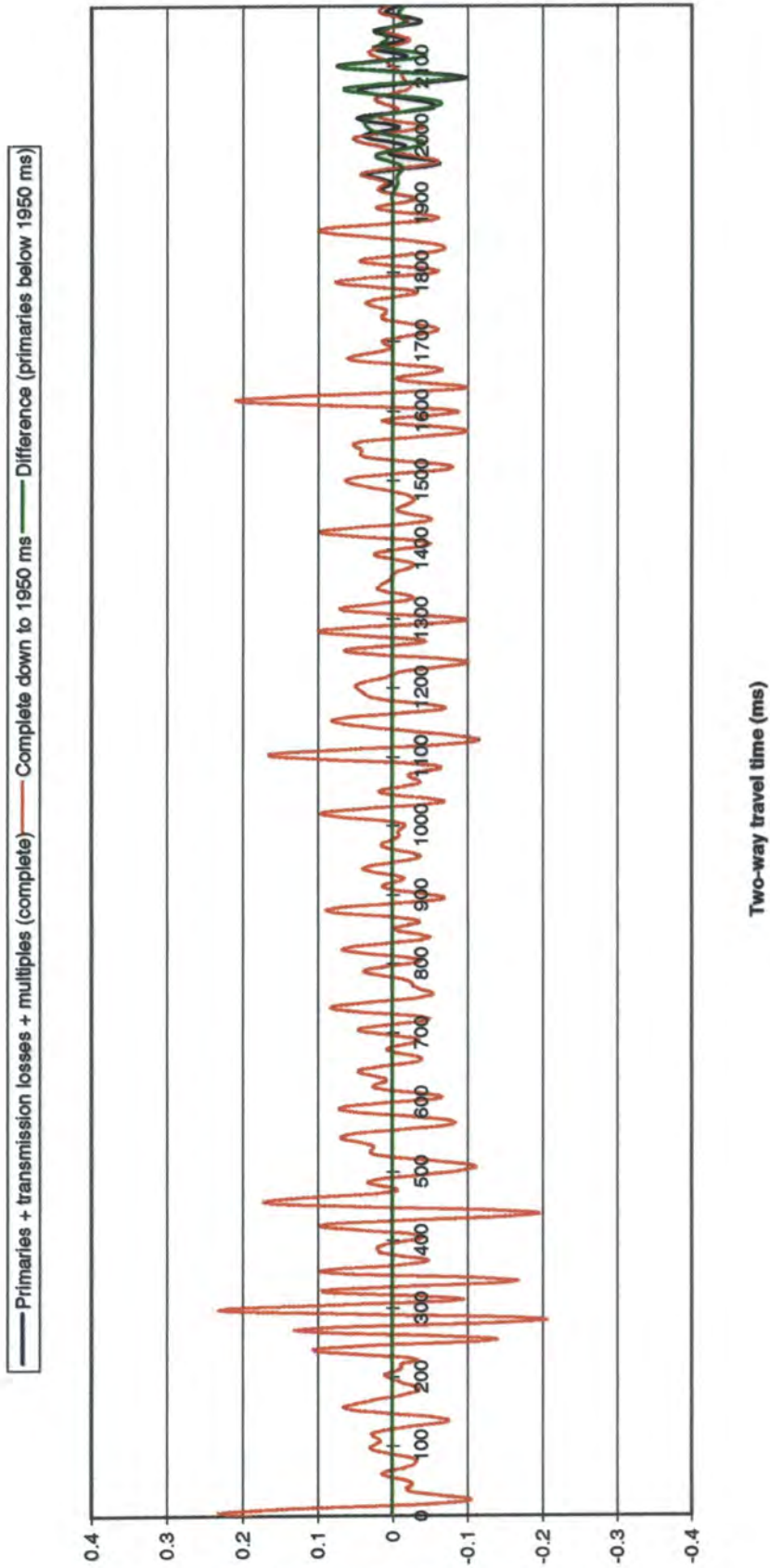


**Figure 4.19.** Composite plot illustrates the effect of the long-period multiples on the primary reflection signal from top Nubian. The blue and the orange traces are overlapped in the area above 1950 ms.

primary event from top Kalash at 1604 ms (compare right-hand panels of Figures 4.16 and 4.18), and consequently suffers more from interference with long-period multiples.

#### 4.7.3 Investigations using lower frequencies

My next step was to calculate the reflection and transmission responses of the Sirte formation at lower frequencies, and compare the outcome with the results obtained by using the conventional seismic bandwidth. The left-hand panel in Figure 4.20 demonstrates the reflection synthetic seismograms obtained by shifting the seismic bandwidth approximately one octave towards the lower frequencies (Figure 4.21). The prominent event of visibly low frequency at 2006 ms shown by the synthetic in the right-hand panel is indeed a primary reflection event which represents the top Nubian horizon. This contrasts with the result of using the original signal bandwidth (Figure 4.18). The large difference in amplitudes suggests that the transmission response of the overlying Sirte formation (cyclic succession of dolomites, shales, and anhydrites) is weak for the original seismic bandwidth, and/or the top Nubian has smaller primary reflectivity at frequencies in that bandwidth.

#### 4.7.4 Analysis in the frequency domain

It is important to determine the useful signal bandwidth for reflected events from the Nubian target horizon. For comparison, this investigation was conducted by computing the amplitude spectra of the composite reflection impulse responses from the top Kalash horizon, as well as from the top Nubian, using a Fortran program written specifically for this job.

The primary reflection coefficient sequence at these two horizons is shown in Figure 4.22. The differences between the complete impulse response (figure 4.4) and the



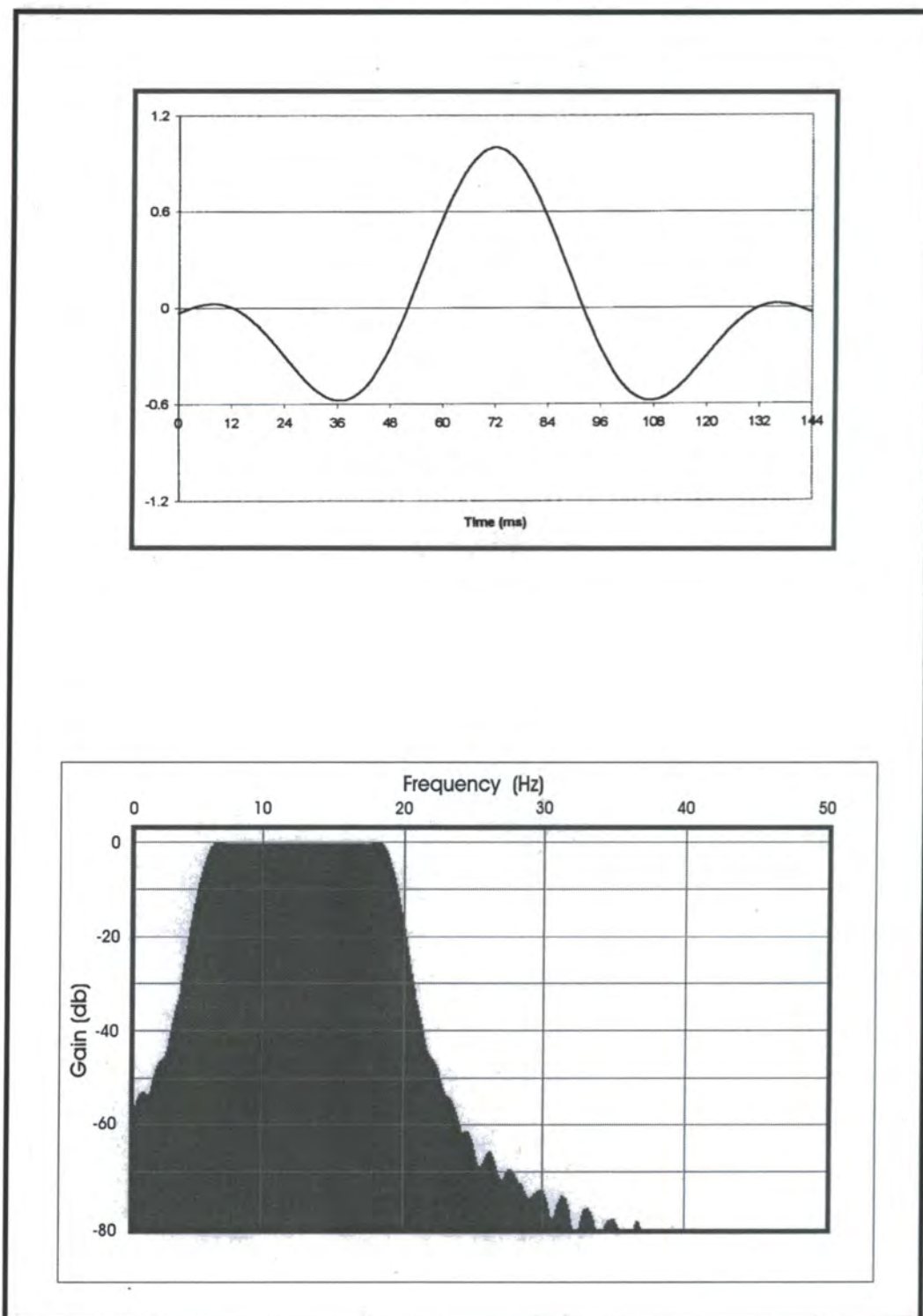
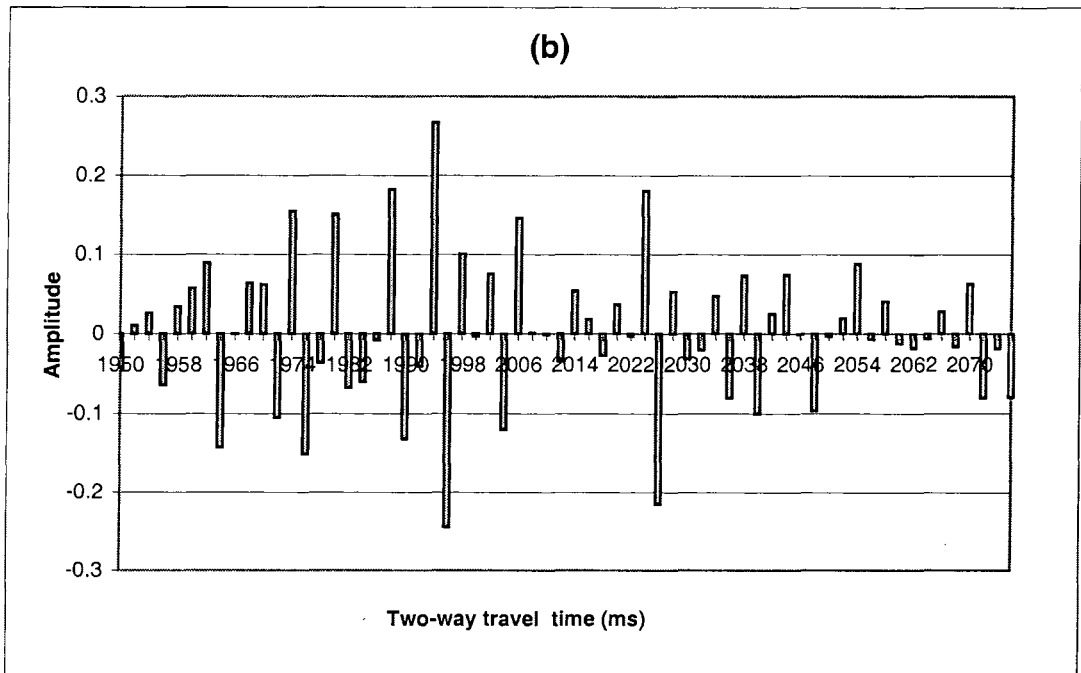
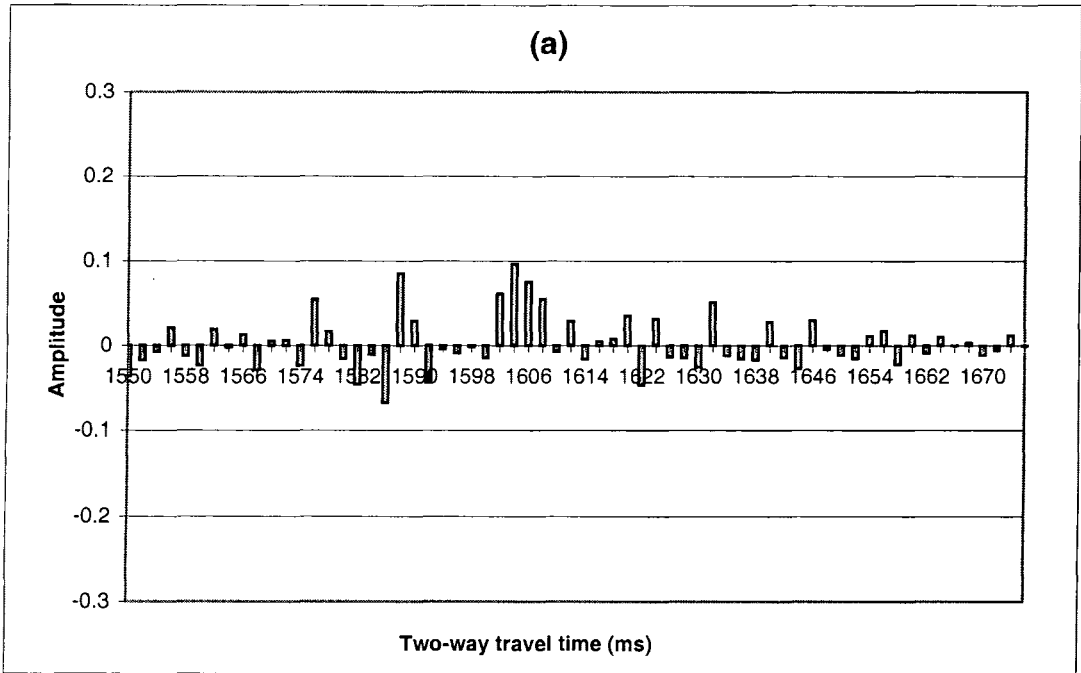


Figure 4.21. Klauder wavelet (5-20 Hz) and the amplitude spectrum of the sweep.

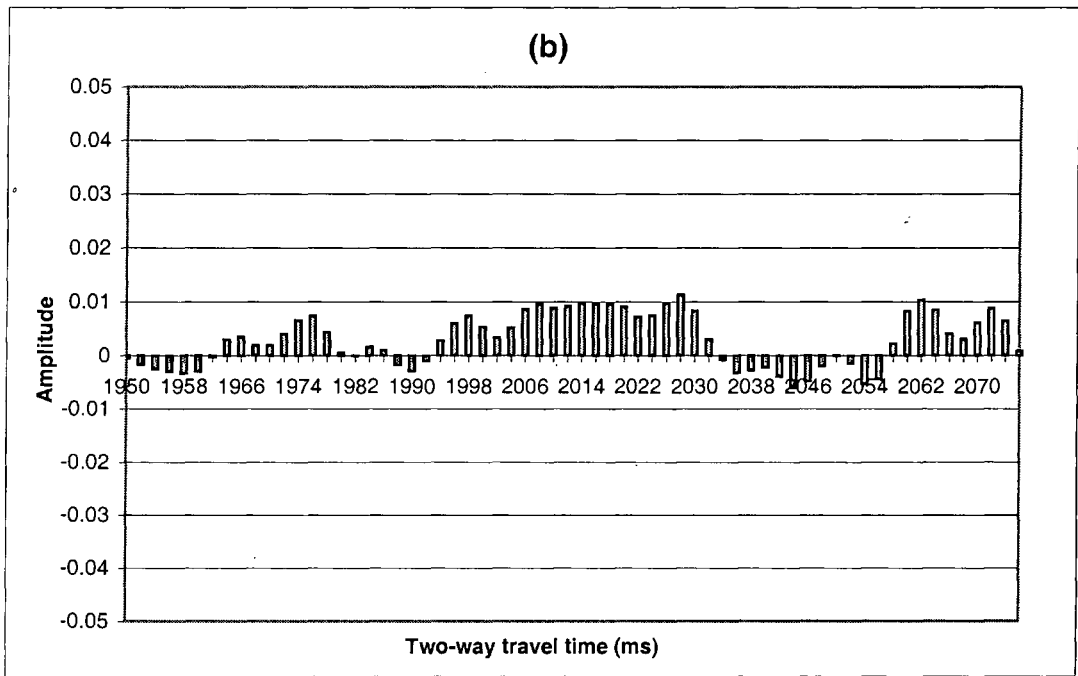
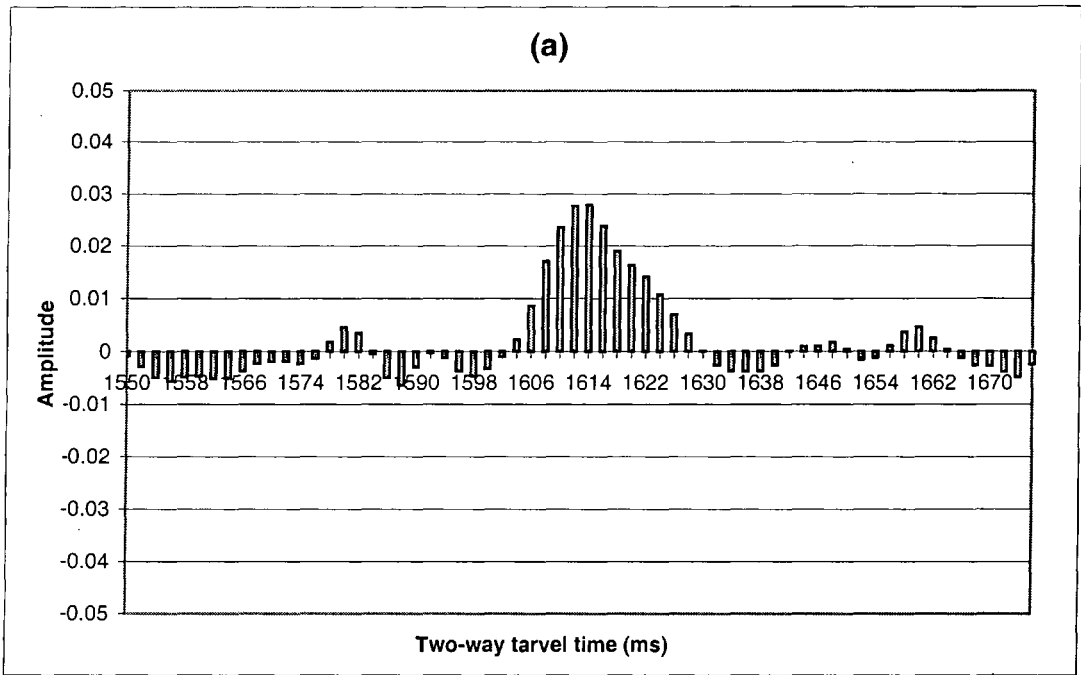


**Figure 4.22.** Primary reflection coefficient sequence from interfaces between 1550 ms and 1676 ms two-way travel time. The top Kalash interface is at 1604 ms. (b) Primary reflection coefficient sequence of interfaces between 1950 ms and 2076 ms two-way travel time. The top Nubian interface is at 2006 ms.

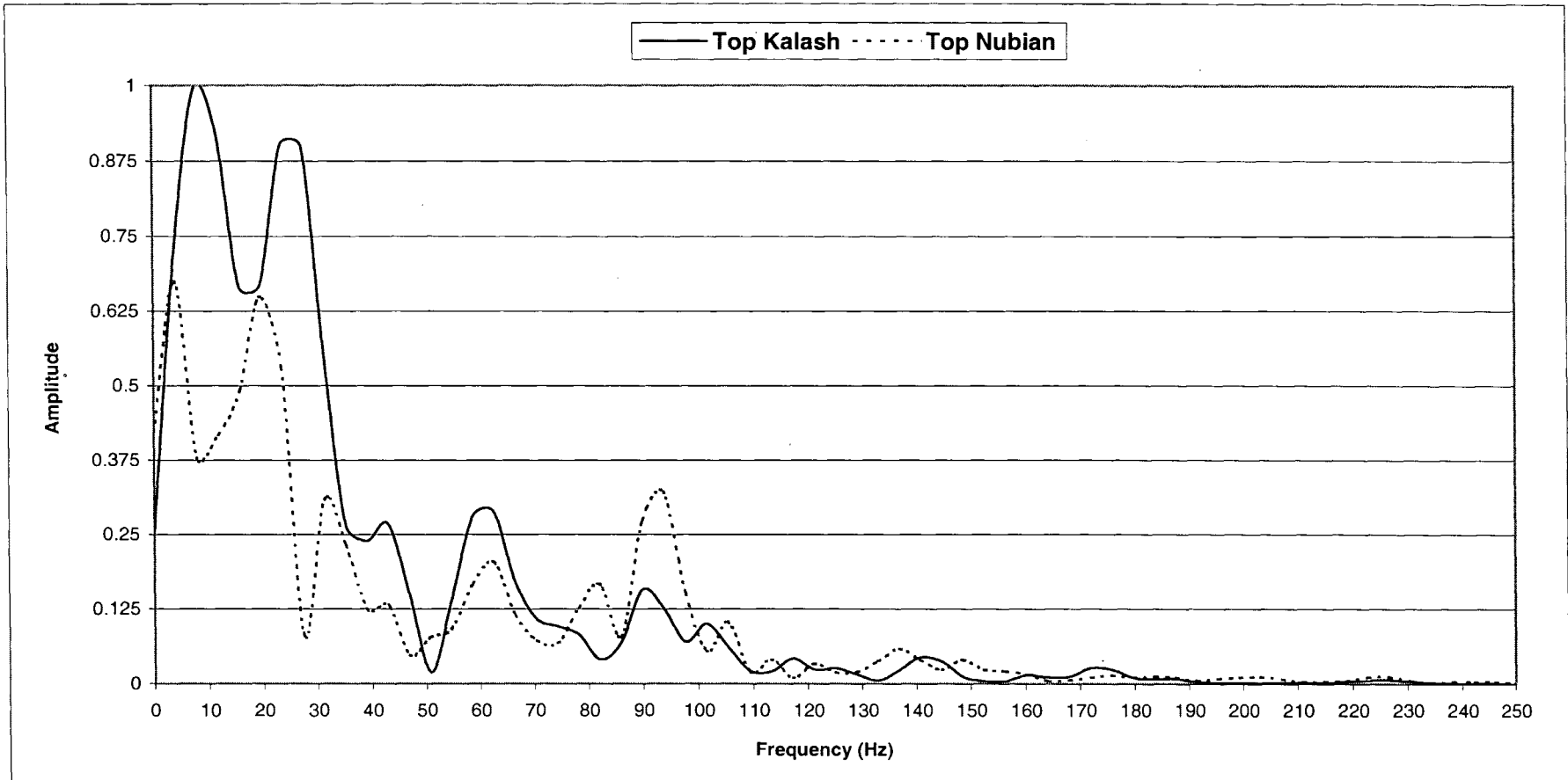
truncated impulse responses used in constructing the synthetics in Figures 4.16 and 4.18 (middle panels) were calculated for windows of 64 samples around the top Kalash and top Nubian horizons. These are referred to here as the composite reflection impulse responses from the respective horizons. The impulse responses were not convolved with any wavelet because the aim was to determine the band-limiting effects of partitioning energy into reflected and transmitted waves at interfaces.

Figure 4.23 shows these composite reflection impulse responses. The primary reflections from top Kalash and top Nubian occur at 1604 ms and 2006 ms, respectively. The only multiples in the composite reflection impulse responses comprise reverberations from primary events for interfaces below 1550 ms and below 1950 ms, respectively. These multiples are not included in the truncated impulse responses. The composite reflection impulse response associated with the top Kalash reflector is a clearly defined, compact, positive peak starting at 1604 ms and covering the next 12 samples (Figure 4.23a). By contrast, the composite reflection impulse response associated with the top Nubian reflector at 2006 ms has a much lower amplitude and longer duration (Figure 4.23b).

The composite reflection impulse responses (Figure 4.23) were then individually input into the forward Fourier transform program to compute their respective amplitude spectra. The length of each wavelet has been extended to 128 samples (the last 64 samples with zero amplitudes) in order to reduce the discretization interval in the frequency domain. The amplitude spectra include transmission effects down to the respective horizons as well as the reflectivity (primaries with their associated peg-leg multiples) which occur in the respective time windows (Figure 4.24). The data above the Sirte formation (top Kalash) are band limited to frequencies of approximately 2-32



**Figure 4.23.** (a) Composite reflection impulse response containing primaries from interfaces below 1550 ms two-way travel time with their associated multiples. (b) composite reflection impulse response containing primaries from interfaces below 1950 ms two-way travel time with their associated multiples.



**Figure 4.24.** The amplitude spectra of the composite reflection impulse responses shown in Figure 4.23, top Kalash (solid) and top Nubian (dashed). Amplitudes have been normalised on the largest value from the top Kalash.

Hz, with a noticeable notch of 4 dB attenuation centred at 18 Hz. At the top Nubian horizon there is a significant reduction in amplitude above 25 Hz. This illustrates the importance of low frequencies in the input seismic signal when trying to get good signal returns from the Nubian, and suggests that the use of frequencies above 25 Hz is a waste of effort.

The differences in response between the top Kalash and top Nubian horizons are due to different reflectivities at these horizons as well as two-way transmission through the Sirte formation: in order to separate these effects, two impulse responses with multiples and transmission losses were computed for the reflectivity sequences from 0 to 1600 ms and from 0 to 2002 ms two-way travel time, after adding a uniform section terminated with an isolated reflector at 3200 ms two-way travel time. The uniform sections were added to diminish the interference of long-period multiples with the direct reflected arrivals. The first 86 ms of the two reflection complexes from the isolated reflector are shown in Figure 4.25. Samples preceding the onset times are high-order multiples. These reflections were padded with 64 samples of zero amplitudes, to maintain the same discretization interval in the frequency domain computations, then input into the forward Fourier transform program. The amplitude spectra are shown in Figure 4.26. The difference between the two spectra indicates that transmission through the Sirte formation thin beds does not have a significant low-pass filtering effect in the seismic bandwidth. The maximum attenuation is only 1.5 dB at approximately 15 Hz; there is less attenuation at higher frequencies up to 40 Hz and above.

Comparison of Figure 4.24 and Figure 4.26 demonstrates that the reduced amplitude of signal above 25 Hz returning from the top Nubian horizon is essentially due to the primary reflectivity, and not due to transmission effects within the Upper Cretaceous.

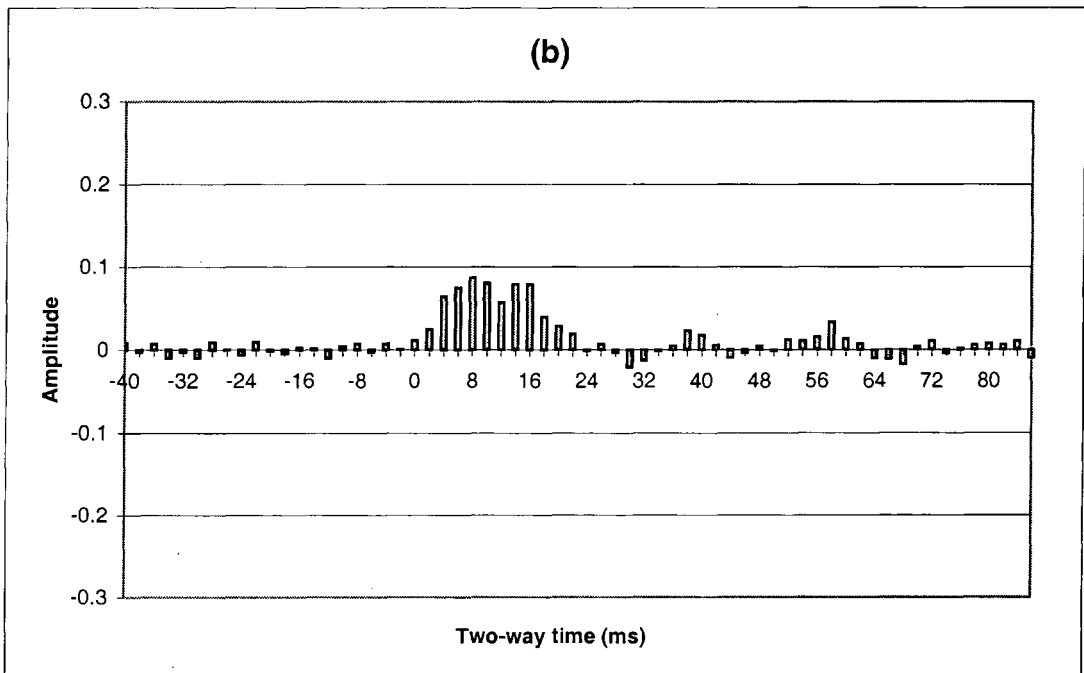
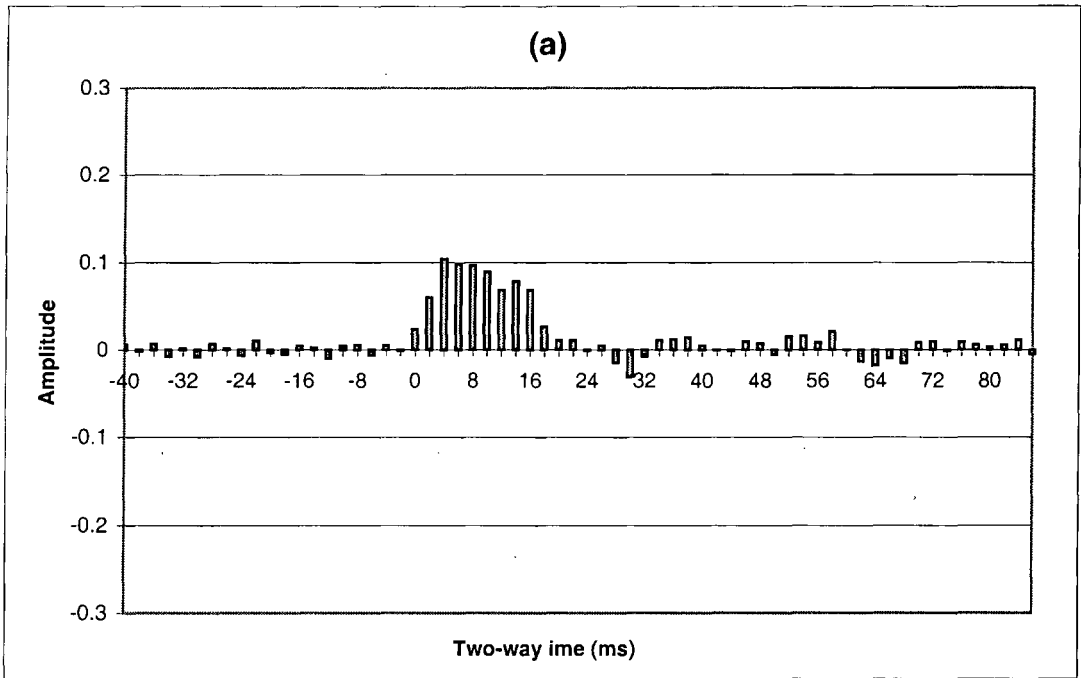


**Figure 4.25.** The reflection complexes from the isolated reflector at 3200 ms TWT. (a) Two-way transmission filtering of the section from 0 to 1600 ms has been included. (b) Two-way transmission filtering of the section from 0 to 2002 ms has been included. The spikes at  $t=0$  are the direct reflected arrivals; spikes preceding  $t=0$  are long-period multiples from shallower interfaces.

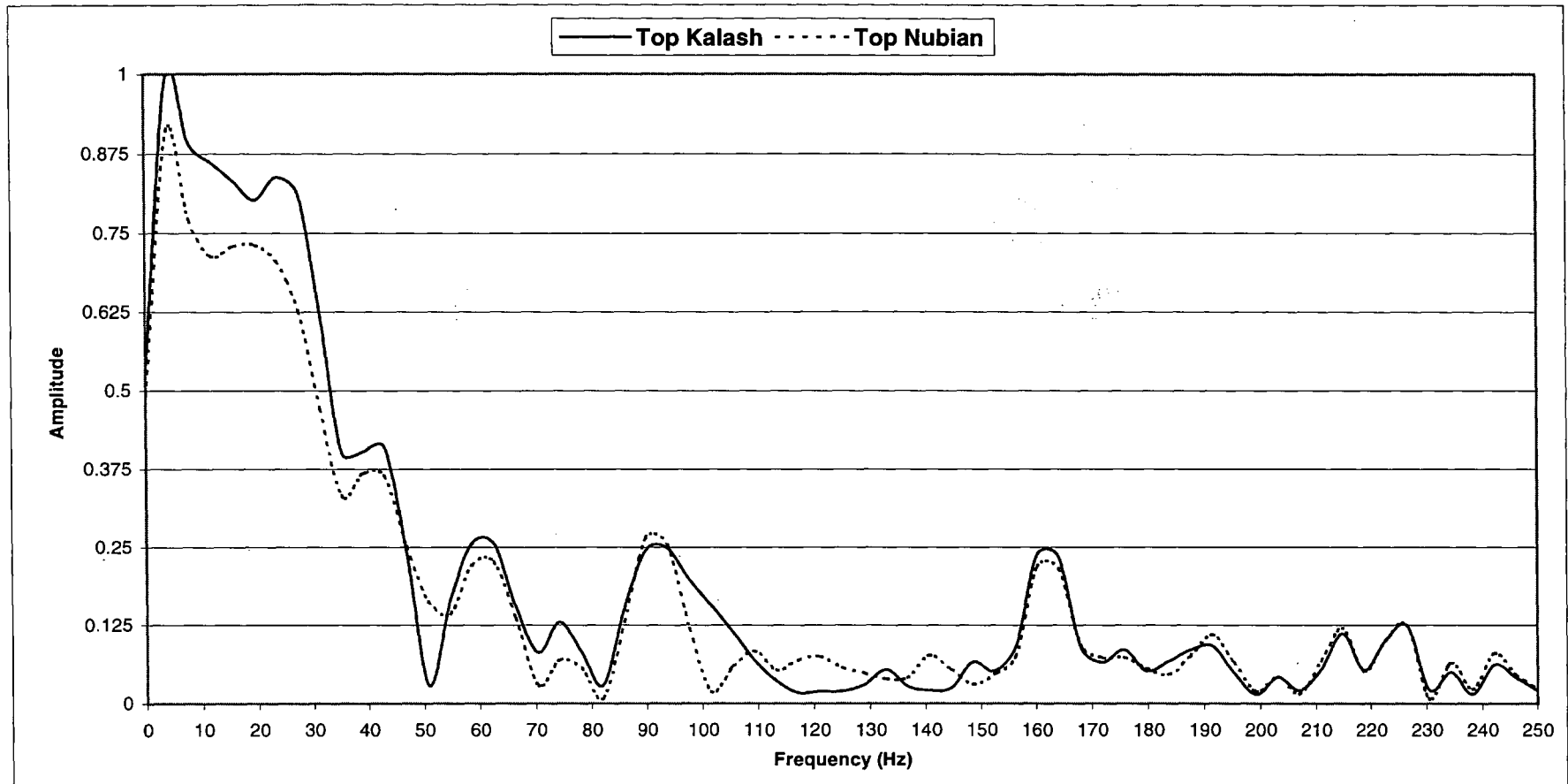


**Figure 4.26.** The amplitude spectra of the reflection complexes shown in Figure 4.25, top Kalash (solid) and top Nubian (dashed). Amplitudes have been normalised on the largest value from top Kalash.

This diagnosis does not affect the conclusion that low frequencies should be used to get interpretable data from the top Nubian.

#### 4.7.5 Geometric spreading and absorption losses within the Upper Cretaceous

In addition to primary reflectivity, transmission losses and multiple reflection effects, two other factors contribute to relative amplitude losses between top Nubian and top Kalash: geometric spreading and anelastic attenuation. Amplitude losses caused by these two factors as the seismic plane wavefront twice traversed the geological section separating the two reflectors, were calculated as follows:

a) For parallel layering at normal incidence, Newman (1973) showed that amplitudes need to be compensated for amplitude decay owing to the spreading out of the wavefront by the factor

$$D_0 = tV_{rms}^2/V_1 \quad (4.19)$$

where  $t$  is the two-way travel time;  $V_{rms}$  is the root-mean square velocity between the surface and the reflector; and  $V_1$  is the velocity in the surface layer.

This effect is frequency-independent. Using this formula, the relative reduction in amplitude of the top Nubian reflector compared to the top Kalash reflector due to geometric spreading is by a factor of 0.73. This result indicates that the reflected wavefront from top Nubian suffers an additional decay in amplitude of less than 3 dB relative to the reflected wavefront from top Kalash.

b) For anelastic absorption, the attenuation is dependent on frequency. Generally, the higher the frequency the greater the loss. The decay of a plane seismic wavefront amplitude due to anelastic effects is computed as a function of frequency using the

relationship derived by Bremaecker et al. (1966) between the wavefront amplitude  $A$  and the distance  $x$  travelled by the seismic wave:

$$A = A_0 \times \exp(-\pi fx / \nu Q) \quad (4.20)$$

where  $A$  and  $A_0$  are the amplitudes at two points a distance  $x$  apart,  $f$  the frequency,  $\nu$  velocity, and  $Q$  is the quality factor.

Sedimentary rocks are generally more absorptive (low values of  $Q$ ) than other rock types (Dobrin, 1988). A constant  $Q$  value of 75 would seem to be a reasonable guess for the sedimentary section between top Kalash and top Nubian reflectors. The relative amplitude due to anelastic effects is plotted versus frequency in Figure 4.27 for different values of  $Q$ . Amplitudes decline linearly with increasing frequency. For the recommended maximum frequency of 25 Hz, the relative attenuation is about 4 dB for  $Q = 75$ , and about 6 dB for  $Q = 50$ .

For low frequencies, losses due to absorption are no worse than losses due to geometric spreading. It is clear that as frequency increases, the relative attenuation due to inelasticity increases and eventually becomes dominant. Over the proposed bandwidth, the combined attenuation effects are estimated as  $-8$  dB at 25 Hz, equivalent to amplitude reduction by a factor of 0.4, and  $-4$  dB at 8 Hz.

#### **4.7.6**      Effect of free-surface on the reflected data

So far, no reflections from the free-surface have been included. All previous calculations were based on acoustic information for the geological sequence from the base of the weathering layer down to the bottom of the well, and the earth model comprised horizontal layers sandwiched between two half-spaces. In order to

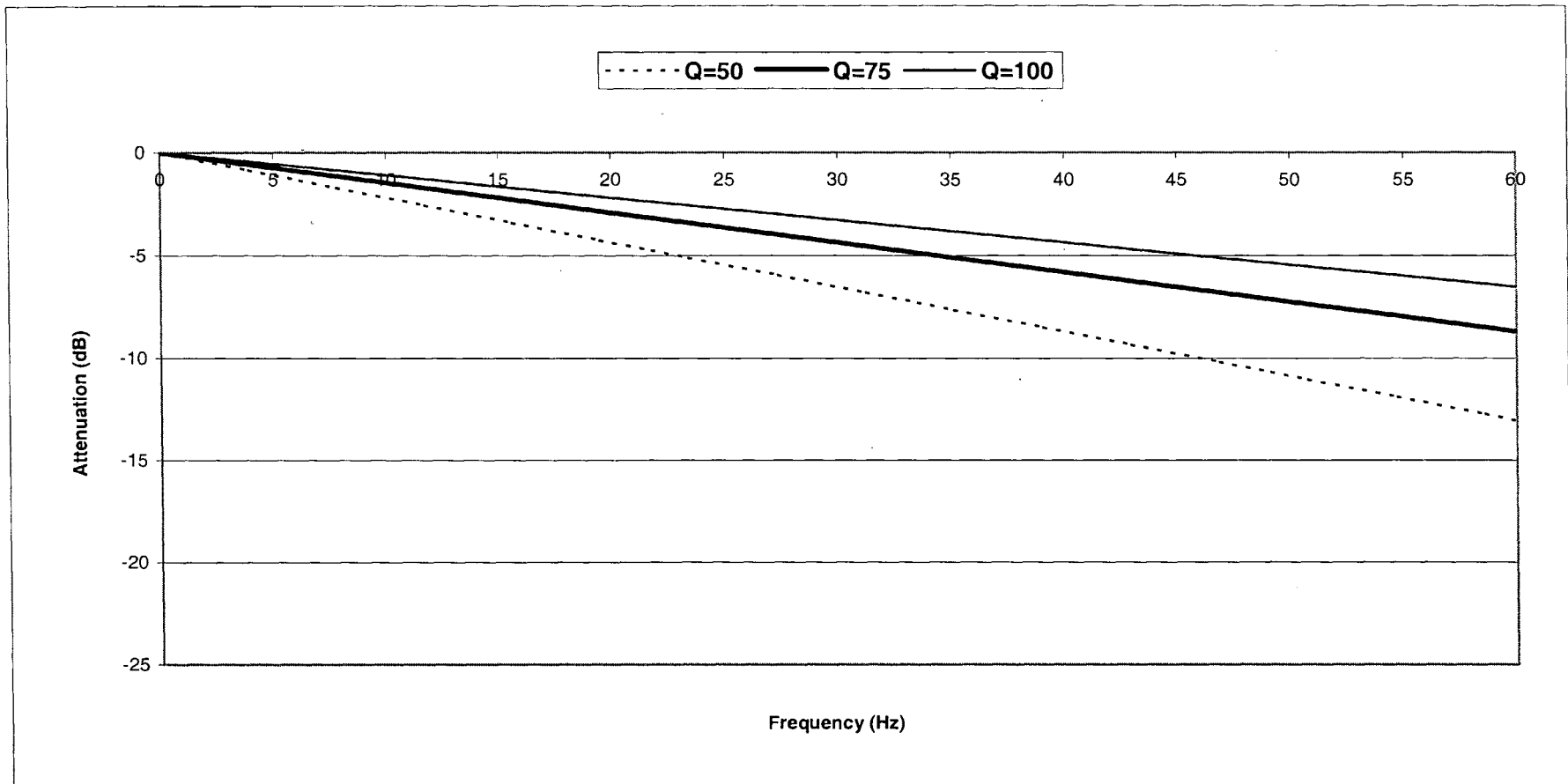


**Figure 4.27.** Amplitude losses due to anelastic effects within the Upper Cretaceous. Average velocity =3725 m/s and thickness=749 m.

understand the near-surface effects on the primaries, two synthetic seismograms (Figure 4.28) have been constructed for the same reflection coefficient sequence with the inclusion of the weathering zone. The depth model of the weathering strata with horizontal reflecting interfaces is shown in Figure 4.14. The primaries-alone seismogram was obtained by convolving the reflection coefficient sequence with the seismic wavelet in Figure 4.21, while the complete seismogram was obtained by convolving the earth's impulse response (computed by using Robinson's program) with the same wavelet. The result depicted by the complete seismogram on the right-hand panel shows a considerable character change in almost all the primary reflections from the major boundaries relative to their counterparts in the left-hand panel. Note the time shift of 200 ms for the reflection events due to inclusion of the weathering.

The overall effects of including the free-surface reflections include destructive interference between multiples involving near-surface reflections and the primaries from top Muailah at 480 ms, top Kalash at 1804 ms and top Nubian at 2206 ms, and constructive interference with the primaries from top Harash at 1300 ms, top Khalifa at 1430 ms and top Meem at 1620 ms. The additional and most prominent reflection at 2320 ms is also produced by constructive interference of multiples involving reflections within the weathering zone. This is supported by its absence from the primaries alone synthetic seismogram (Figure 4.28). It is not possible to identify a single multiple raypath giving rise to this event, so it must result from constructive interference of multiple reflections over the entire range (Dennison, 1960).

To enable more detailed inspection, I constructed a few more complete seismograms for the same sequence, but truncated at various depths. The black trace in Figure 4.29 is a complete synthetic down to the bottom of the hole. The yellow trace in the same figure

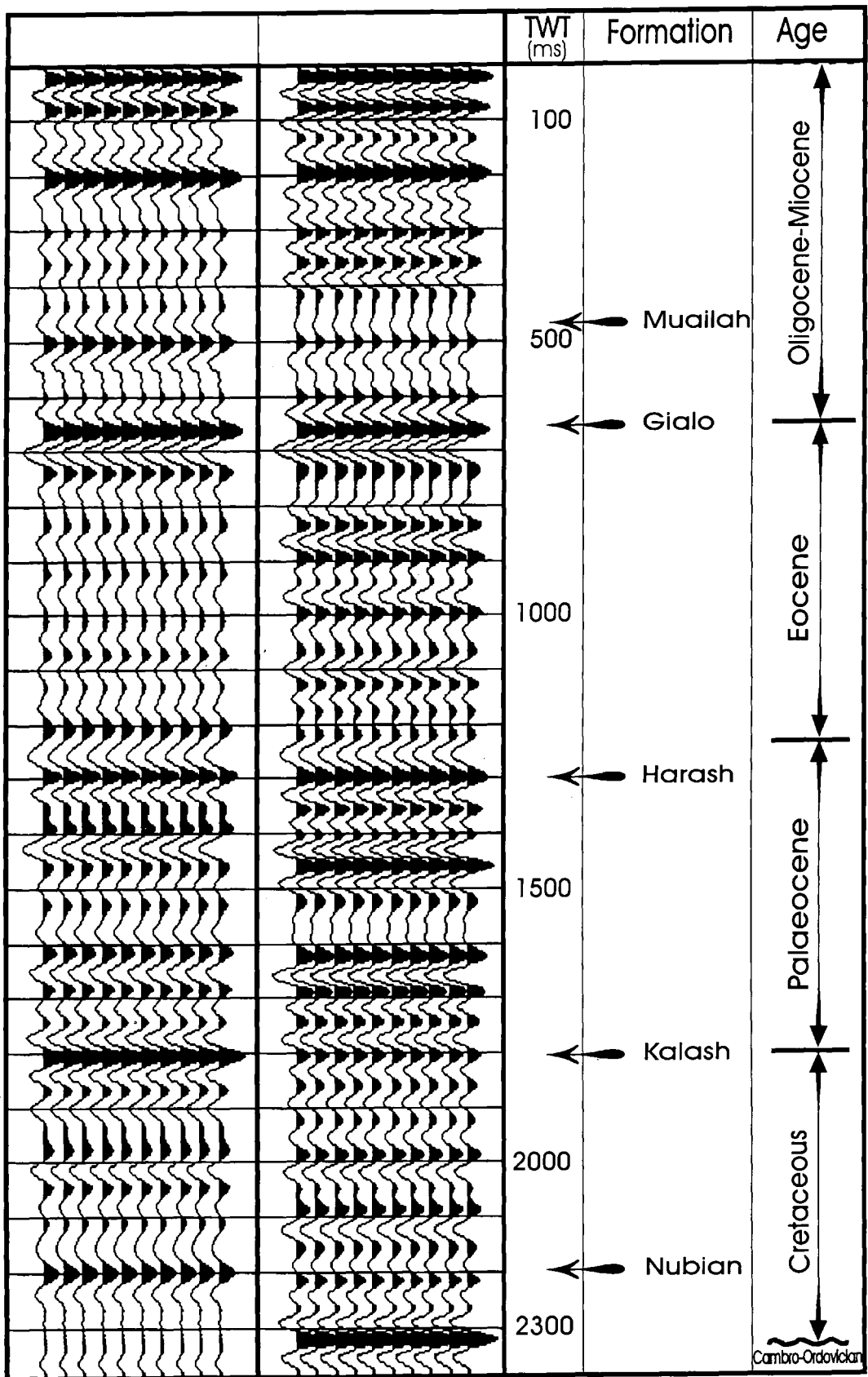
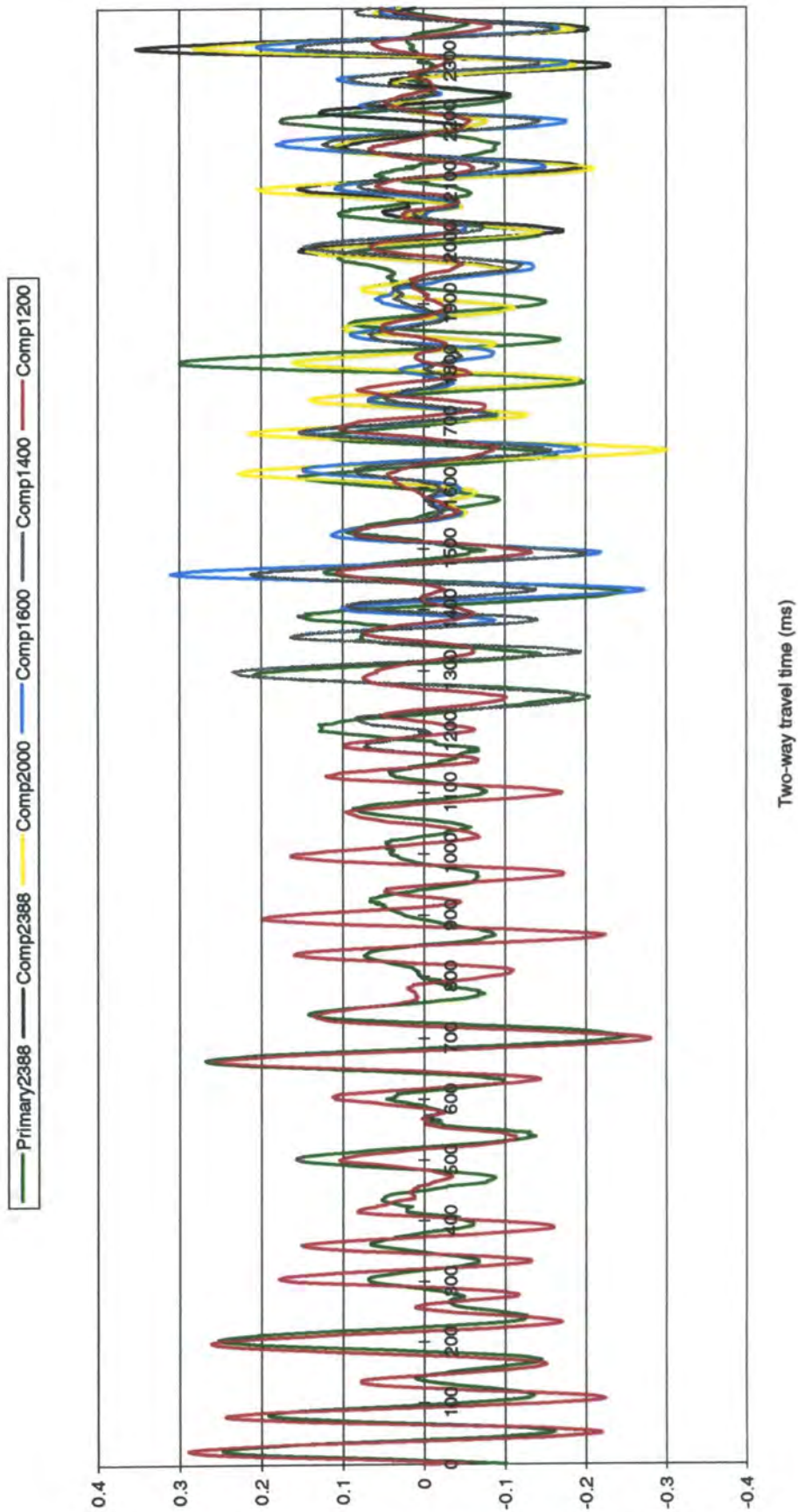


Figure 4.28. Primaries-only and complete seismograms obtained by including the near-surface effects. The base of the weathering zone at 200 ms two-way travel time.



**Figure 4.29.** Seismograms computed with the inclusion of the free-surface. Green and black are primaries-only and complete down to the bottom of the well. The rest are complete with truncated reflectivity as shown in the left panel.

is the first truncated synthetic, computed for the reflectivity from the ground surface down to 2000 ms two-way travel time. A constant velocity was assigned to the segment between 2000 ms and the bottom of the hole: i.e., all events below 2000 ms are multiples from shallower interfaces. The other traces were computed by truncating the reflectivity at 1600 ms, 1400 ms and 1200 ms two-way travel time (Figure 4.29). It becomes obvious from these results that the observed event at 2320 ms is a composite of several reflections from many interfaces including the free-surface, arriving at the same two-way travel time. For example, when the section from 1200 ms downward was excluded, the amplitude of this event was approximately 0.05. It increased to about 0.15 by adding only the segment between 1200 ms and 1400 ms, and continued increasing gradually as more interfaces became involved until it reached its maximum value when the entire sequence was used. The maximum value is nearly seventeen times larger than the primary event at the same two-way travel time. The other significant observation is the visible growth of the side lobe from the top Khalifa at 1460 ms, which is also due to composite multiple interference.

I have not carried out detailed analysis on synthetic seismograms including the near surface for two reasons: the model of the near-surface geology is simplified and the near-surface layers heavily attenuate seismic energy by anelastic absorption and scattering. Also I note that long period multiples should be effectively suppressed by common midpoint stacking.

#### **4.7.7**      Comparison of the real data with the primaries-only synthetic

It is interesting to compare the synthetic seismogram of primaries only with the seismic trace on the processed section at the well location. The comparison of the seismogram

and the processed trace (Figure 4.30) indicates reasonable correlation from the top Kalash upwards, although a few changes have affected the amplitude relationship. The disappearance of the top Muailah event on the seismic trace, which corresponds to the discrete event at 285 ms on the synthetic seismogram, is most likely due to the tight mute function at the near-offset traces, and the omitted source stations on either side of the well head. The strong event at 600 ms on the real data is not a consistent seismic event; it is an intermittent event, which suggests that the mute function may have not been steep enough at this offset. Thus some of the reverberant refracted waves may not have been sufficiently muted out, and leaked through the stack. The real seismic data lack interpretable information below the top Kalash horizon.

The primaries-only synthetic (right-hand panel in Figure 4.30) shows reflectors around 2076 ms which are much weaker on the complete synthetic in Figure 4.13 and are not identifiable at all on the real data. These reflectors are associated with the impermeable shale layer which divides the reservoir into two separate units: Nubian 'A' and Nubian 'B' (Figure 2.1). The obvious reduction in amplitude on the complete synthetic is presumably due to destructive interference of long-period multiples. I have not considered how to optimise the reflection response from this shale layer since it would be a poor seismic marker. This is known from well data which show that the shale has significant lateral changes in both acoustic contrasts and thickness.

Finally, primaries-only synthetic seismograms for the geological sequence from the base of the weathering to the bottom of the well are presented for the original signal bandwidth and the low frequency bandwidth (Figure 4.31). It is quite clear that the predicted primary event from top Nubian stands out much more at lower frequencies than at higher frequencies.

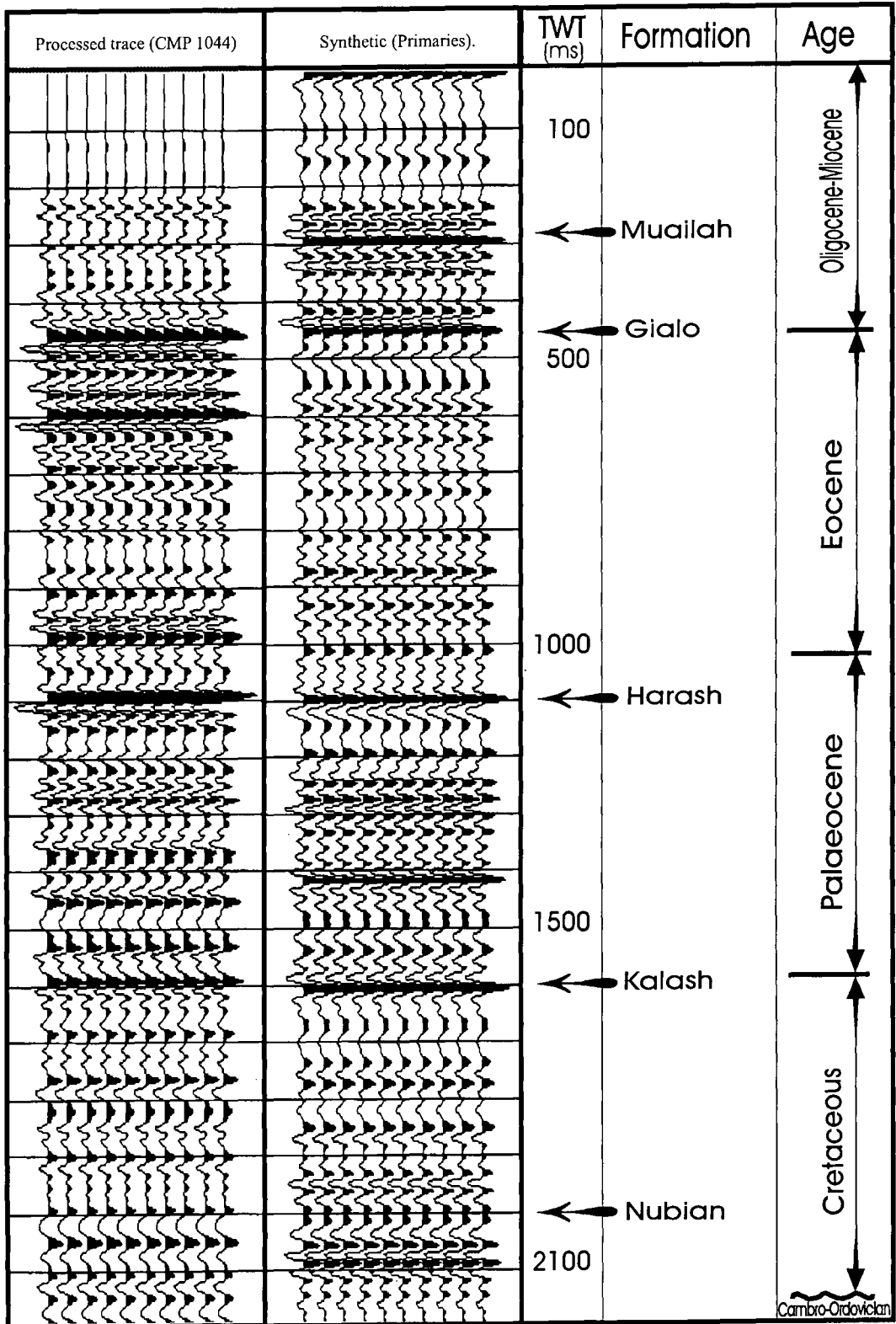


Figure 4.30. Comparison of primaries-only synthetic seismogram and the processed trace (CMP 1044) from the experimental line.

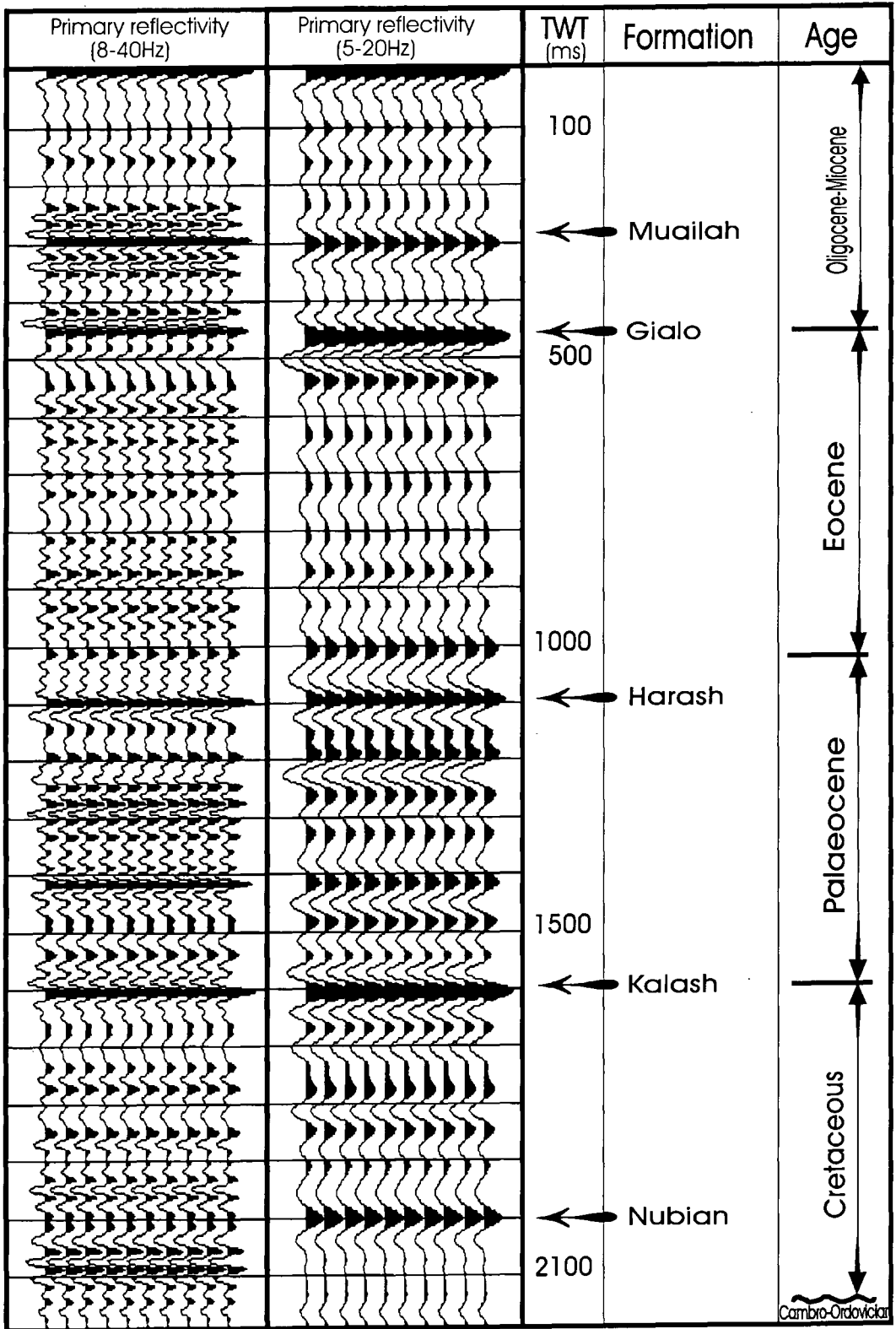


Figure 4.31. A comparison of high frequencies and low frequencies primaries-only synthetic seismograms.



## 4.8 Summary

The failure to detect clear reflection signals from the exploration target using the conventional seismic bandwidth of 8-40 Hz has been investigated using 1-D synthetic seismograms. Composite reflection impulse responses were calculated for the top Kalash and top Nubian horizons from the differences between the full 1-D impulse responses and truncated 1-D impulse responses. They included the primary reflection events from a selected time window around each horizon, as well as short period multiple arrivals associated with those primaries, but they excluded all multiple events associated with primaries outside the window. Amplitude spectra of the composite reflection impulse responses showed that the relative amplitude for the top Nubian response was reduced by a factor of 0.6 (-4.5 dB) compared to the top Kalash response at frequencies up to 25 Hz. The top Nubian amplitude response dropped off sharply above 25 Hz, whereas the top Kalash reflection response remained high up to 30 Hz.

The composite reflection impulse response include transmission effects as well as the reflectivity at the target horizon, so the transmission effects were calculated separately. The maximum relative attenuation of the two-way transmitted pulse for the top Nubian event compared to the top Kalash is -1.5 dB at 15 Hz. Thus the weaker reflectivity at the top Nubian horizon is responsible, on average, for relative attenuation of at least -3 dB compared to the top Kalash horizon at frequencies up to 25 Hz.

The transmission effects of frequency-dependent attenuation (absorption) and geometric spreading within the Upper cretaceous contribute further attenuation, estimated as -8 dB at 25 Hz and -4 dB at 8 Hz. Overall, the combined effects of transmission losses, reflectivity at each horizon, geometric spreading and anelastic attenuation amount to a relative attenuation in the reflection response at the top Nubian horizon compared to top

Kalash horizon of about  $-12$  dB at 25 Hz and about  $-8$  dB at 10 Hz.

Modelling the thick weathering layer has caused suppression of the primary event amplitudes from top Kalash and top Nubian horizons by destructive interference with multiples. Such effects can only be removed, or attenuated, in the processing by common midpoint stacking and deconvolution. However, in practice the weathering layers are likely to be highly attenuating, so it is suggested that the main obstacles to obtaining good reflection data from the Nubian formation have been diagnosed using the synthetics which omitted the weathered zone.

# CHAPTER FIVE

## Conclusions and suggestions for further work

Full discussions of all the processing and the 1-D synthetic seismograms which were carried out during this project have been given in chapter 3 and chapter 4, respectively. The main conclusion points raised and suggestions for further work are summarised below.

### Reprocessing conclusions

- Increasing the number of recording channels to include offsets larger than the depth of the primary target would result in undesirable NMO stretch which in turn degrades the stacking quality. The maximum offset recommended is 4.0 km: based on the reprocessing results it seems to be quite sufficient for recording reflections returning from the target level and even from the basement.
- It has become obvious that the failure of previous seismic surveys, including the present dataset, to image the Wadi Field structure below the top Upper Cretaceous horizon is essentially due to propagation effects in the earth and not due to any fundamental flaws in acquisition or processing parameters.

### 1-D synthetics conclusions

- Build up effects of transmission losses caused by the large number of interfaces is prominent and acts in a frequency-independent manner. The significance of the short-period multiples in restoring these losses is frequency-dependent and depends on the vertical changes of the acoustic impedance. Multiples have provided adequate penetration through the Tertiary to obtain reflection signal returns from the top Kalash horizon when the conventional bandwidth was employed. The

further reduction in amplitude due to two-way transmission through the Upper Cretaceous is not very severe, and is not the most important reason for the poor signal returns from the Lower Cretaceous.

- The composite reflection impulse responses indicate that the lack of interpretable information from the target horizon, at a depth of 3464 m below the surface, is more attributable to the weak reflectivity at frequencies above 25 Hz than to transmission losses within the thin layers of the Sirte formation.
- Geometric spreading and anelastic attenuation also significantly reduce the reflection response from the top Nubian compared to the top Kalash, the last interpretable horizon.
- The total effects due to transmission losses, reflectivity at each horizon, geometric spreading and anelastic attenuation sum to an attenuation in the reflection response at the top Nubian relative to the top Kalash of about  $-12$  dB at 25 Hz and about  $-8$  dB at 10 Hz. At far offsets, there will be some additional relative reduction in amplitude as a result of mode conversions, which are not included in the 1-D synthetic seismograms.
- Destructive interference of multiple reflections involving reverberations within the simplified weathering model with the primary reflections from the top Kalash and the top Nubian could be significant. However, in practice the weathering layers will be highly attenuating, and this factor was not taken into account in the synthetics. Also, common midpoint stacking should be effective in suppressing long-period multiples.

#### Suggestions for future approaches

- It is advisable that the one-dimensional synthetic investigations should be extended to include more wells in the area, so that results may be obtained for several

different wells. Preferably wells should be chosen where density logs are also available, in addition to sonic logs.

- I recommend that Sirte Oil Company should acquire another experimental line with full-fold coverage of several kilometres, using five heavy vibrators sweeping over a bandwidth of 5–25 Hz, a split-spread geometry with 240 recording channels, and source and receiver group intervals of 30/35 m with source stations placed half-way between the geophone stations. As the reflection response of the top Nubian is 12 dB lower than from the top Kalash, at least four times more source effort than previously used is necessary. I recommend that 12 sweeps/vibrator point with sweep duration of 10 s should be used. Geophone groups of 36 geophones/station with a natural frequency of 8 Hz should be quite satisfactory.

The introduction of harmonics due to distortion associated with the ground to base-plate coupling at the low-frequency end of the sweep may result in a quality control problem and thus limit the performance of the source units. This can only be tested on location. If it appears to be serious, then we will be left with no other alternative than to use dynamite as the source.

# CHAPTER SIX

## References

Advance Geophysical Corporation, 1995, ProMAX Reference Manual, Volumes 1 & 2.

Anstey, N.A., 1960, Attacking the problems of the synthetic seismogram. *Geophysical Prospecting* 8, 242 - 259.

Anstey, N. A., 1986, Whatever happened to ground roll? *The Leading Edge* 5(3), 40-45.

Barr, F.T. and Weegar, A. A., 1972, Stratigraphic Nomenclature of the Sirte Basin, Libya. Published by the Petroleum Exploration Society of Libya, Tripoli, Libya.

Bremaecker, J.Cl., Godson, R.H. and Watkins, J.S., 1966, Attenuation measurements in the field. *Geophysics* 31, 562-569.

Claerbout, J.F., 1985, Fundamentals of Geophysical Data Processing with Applications to Petroleum Exploration, pages 144 - 157. Blackwell Scientific Publications.

Clifford, H.J., Grund, R., and Musrati, H., 1980, Geology of a stratigraphic giant: Messla oil field, Libya. In *Giant Oil and Gas Fields of the Decade 1968 – 1978*, Halbouty, M., T., (ed.). Memoir 30, American Association of Petroleum Geologists, Tulsa, 507 - 524.

Conant, L.C., and Goudarzi, G.H., 1967, Stratigraphic and tectonic framework of Libya. *American Association of Petroleum Geologists Bulletin* 51, 719 – 730.

Conybeare, C.E.B., 1979, *Lithostratigraphic Analysis of Sedimentary Basins*. Academic Press.

Dennison, A.T., 1960, An introduction to synthetic seismogram techniques. Geophysical Prospecting 8, 231-241.

Dobrin, M.B., and Savit, C. H., 1988, Introduction to Geophysical Prospecting. 4<sup>th</sup> edition, McGraw-Hill, New York.

El-Jard, M., 1988, Geology of the Wadi Field, Sirte Oil Company. Internal Report No. 228.

Goupillaud, P.L., 1961, An approach to inverse filtering of near-surface layer effects from seismic records. Geophysics 26, 754 - 760.

Gumati, Y.D., and Kanes, W., 1985, Early Tertiary subsidence and sedimentary facies - northern Sirte Basin, Libya. American Association of Petroleum Geologists Bulletin 69, 39 - 52.

Hamid N. Al-Sadi, 1982, Seismic Exploration Technique and Processing. Birkhauser AG.

Hatton, L., Worthington, M. H. and Makin, J., 1986, Seismic Data Processing. Blackwell Scientific Publications, London.

Liu, X., and Goult, N.R., 1999, Comparison of 2-D filters for suppressing noise in common shot gathers. Submitted to First Break.

Marsden, D., 1993, Static corrections – a review. The Leading Edge 12(1), 43-49; 12(2), 115-120; 12(3), 210-216.

McBride, E.F., and Jonas, E.C., 1963, Diagenesis of Sandstone and Shale. Application to Exploration of Hydrocarbons. Department of Geological Sciences, University of Texas at Austin.

Newman, P., 1973, Divergence effects in a layered earth. Geophysics 38, 481-488.

O'Doherty, R.F., and Anstey, N.A., 1971, Reflections on amplitudes. *Geophysical Prospecting* 19, 430-458.

Robinson, E.A., 1983, *Multichannel Time Series Analysis with Digital Computer Programs*. 2nd edition, Goose Pond Press.

Schoenberger, M., and Levin, F.K., 1974, Apparent attenuation due to intrabed multiples. *Geophysics* 39, 278-291.

Selley, R.C., 1968, Facies profile and other new methods of graphic data presentation, application in quantitative study of Libyan Tertiary shoreline deposits. *Journal of Sedimentary Petrology* 38, 553 - 372.

Wiggins, R.A., Lerner, K.L. and Wisecup, R.D., 1976, Residual statics analysis as a general linear inverse problem. *Geophysics* 41, 922-938.

Wuenschel, P.C., 1960, Seismogram synthesis including multiples and transmission coefficients. *Geophysics* 25, 106-129.

Yilmaz, O., 1987, *Seismic Data Processing*. Society of Exploration Geophysicists, Tulsa.

## Appendix A

This appendix contains details and listings of the computer programs that were written during the course of this project. I wrote all the programs in Fortran 77 to run on an HP or a Sun 4 work station, except for program A4 which is a Seismic Unix program (Cohen, J.K., and Stockwell, J.W., (1997), CWP/SU: Seismic Unix Release 30.0: a free package of seismic research and processing, Center for Wave Phenomena, Colorado School of Mines).

The format of the input data files for programs A1, A2, A3 and A5 are shown at the end of each program listing.

**A1** Primaries, primaries with transmission losses and complete synthetic Seismograms program

PROGRAM COMPLETE

\*\*\*\*\*

\*\* This program performs the computations of the primaries-only synthetic seismogram, the primaries  
 \*\* with transmission losses synthetic seismogram, the polynomials F(Z) and G(Z), the product of the  
 \*\* transmission coefficients, the earth's impulse response Cz(Z) (complete reflectivity), the escaping  
 \*\* waves impulse response Tz(Z) (transmissivity) and the complete synthetic seismogram, for a stack  
 \*\* of layers confined between two half-spaces.

-----

- \*\* C = reflection coefficient for a particle velocity
- \*\* LC = total number of interfaces
- \*\* CR = reflection coefficient with reversed polarity
- \*\* RC = redefined reflection coefficient
- \*\* F(LC) = recursively generated polynomial F(Z) for degree N
- \*\* G(LC) = recursively generated polynomial G(Z) for degree M, where M=N.
- \*\* N =M=LC= length of the polynomials F(Z) and G(Z)
- \*\* PF = previous values of coefficients in F(Z)
- \*\* PG = previous values of coefficients in G(Z)
- \*\* Cz = earth's impulse response for LC interfaces = wavefield reflected into  
 to the upper half space (reflectivity)
- \*\* TC = one-way transmission coefficient
- \*\* Tz = escaping waves response (downgoing waves) = wavefield transmitted into  
 the lower half space (transmissivity)
- \*\* S = input source wavelet of length LS samples
- \*\* XP = primaries synthetic seismogram of length LX (LX=LC+LS-1)
- \*\* TWTC = two-way transmission coefficients
- \*\* PTWTC = product of TWTC
- \*\* POWTC = product of one-way transmission coefficients
- \*\* R = reflected amplitude with transmission losses included
- \*\* XPT = primaries with transmission losses synthetic seismogram of length LX
- \*\* CX = complete synthetic seismogram of length LX
- \*\* SI = sampling interval in ms
- \*\* J = one-way travel time in ms
- \*\* JJ = two-way travel time in ms
- \*\* XT = transmitted waves synthetic seismogram of length LX

\*\*\*\*\*

```

DIMENSION C(1095), CR(1095), RC(1095), F(1095), G(1095), PF(1095)
DIMENSION PG(1095), Cz(1095), TC(1095), Tz(1095), S(73), XP(1167)
DIMENSION TWTC(1094), PTWTC(1094), POWTC(1), R(1095), XPT(1167)
DIMENSION CX(1167), XT(1167)
INTEGER LC, LS, Y, J, JJ, SI, M, N
REAL POWTC
  
```

```

PRINT*,INPUT LC'
READ*,LC
PRINT*,INPUT LS'
READ*,LS
OPEN(UNIT=1,FILE='refl.dat',STATUS='OLD')
OPEN(UNIT=2,FILE='wavelet',STATUS='OLD')
OPEN(UNIT=3,FILE='A1 output1')
OPEN(UNIT=4,FILE='A1 output2')
OPEN(UNIT=5,FILE='A1 output3')
OPEN(UNIT=6,FILE='A1 output4')
OPEN(UNIT=7,FILE='A1 output5')
  
```

```

OPEN(UNIT=8,FILE='A1 output6')

M =LC
N =LC
LX=LC+LS-1
LB=((LS-1)/2)+1
LD=LX-LB+1
SI=2
CALL INPUT1(LC,C,CR)
CALL WAVELET(LS,S)
CALL CONVOL1(LC,CR,LS,S,LX,XP)
* Calculate reflection coefficients with transmission losses
R(1)=CR(1)
PTWTC(1)=1-(CR(1)*CR(1))
DO 10 I=2,LC
L=I-1
R(I)=CR(I)*PTWTC(L)

WRITE(10,*) R(I)

IF(I.EQ.LC) GO TO 99
TWTC(I)=1-(CR(I)*CR(I))
PTWTC(I)=PTWTC(L)*TWTC(I)
10 CONTINUE
99 CALL CONVOL2(LC,R,LS,S,LX,XPT)

* Redefine reflection coefficients in reverse order to coincide with Claerbout's notation, incident
* wave is in the upper half-space
DO 20 K=1,LC
RC(K)=CR(LC+1-K)
20 CONTINUE

* Calculate polynomials F(Z) and G(Z)
F(1)=1
PF(1)=1
PG(1)=RC(1)
DO 30 J=2,LC
F(J)=0
PF(J)=0
G(J)=0
PG(J)=0
30 CONTINUE

DO 40 K=2,LC
G(1)=RC(K)
DO 50 I=2,K
F(I)=PF(I)+RC(K)*PG(I-1)
G(I)=RC(K)*PF(I)+PG(I-1)
50 CONTINUE

DO 60 I=1,K
PF(I)=F(I)
PG(I)=G(I)
60 CONTINUE
40 CONTINUE
* Output polynomials F(Z) and G(Z)
WRITE(3,*)(** Polynomials F(Z) G(Z)**)
DO 70 J=1,LC
WRITE(3,5) F(J), G(J)

```

```

5 FORMAT(12X,F9.5,2X,F9.5)
70 CONTINUE

* Calculate product of one way transmission coefficients
TCPROD=1+RC(1)
DO 80 J=2,LC
TC(J)=1+RC(J)
TCPROD=TCPROD*TC(J)
80 CONTINUE
Y=1
POWTC(Y)=TCPROD
CALL POLYCz(M,G,N,F,LC,Cz)
CALL POLYTz(Y,POWTC,N,F,LC,Tz)
CALL CONVOL3(LC,Cz,LS,S,LX,CX)
CALL CONVOL4(LC,Tz,LS,S,LX,XT)

* All outputs commence at zero two-way travel time
* Output primaries only synthetic seismogram
WRITE(4,*)(** Primaries only synthetic seismogram **)
DO 90 I=LB,LD
JJ=(I-LB)*SI
WRITE(4,15) JJ, XP(I)
15 FORMAT(2X,I5,3X,F9.5)
90 CONTINUE

* Output primaries with transmission losses synthetic seismogram
WRITE(5,*)(** Primaries with losses synthetic seismogram **)
DO 100 J=LB,LD
JJ=(J-LB)*SI
WRITE(5,25) JJ, XPT(J)
25 FORMAT(2X,I5,3X,F9.5)
100 CONTINUE

* Output earth's impulse response and one-way transmission response
WRITE(6,*)(* Impulse response one-way transmission responses *)
DO 110 K=1,LC
WRITE(6,35) Cz(K), Tz(K)
35 FORMAT(5X,F9.5,10X,F9.5)
110CONTINUE

* Output complete synthetic seismogram
WRITE(7,*)(** Complete synthetic seismogram **)
DO 120 L=LB,LD
JJ=(L-LB)*SI
WRITE(7,45) JJ, CX(L)
45 FORMAT(2X,I5,3X,F9.5)
120CONTINUE

* Output synthetic seismogram for downgoing transmitted waves
DO 130 M=LB,LD
J=(M-LB)*(SI/2)
WRITE(8,55) J, XT(M)
55 FORMAT(2X,I5,3X,F9.5)
130CONTINUE

CLOSE (UNIT=1)
CLOSE (UNIT=2)
CLOSE (UNIT=3)
CLOSE (UNIT=4)

```

```

CLOSE (UNIT=5)
CLOSE (UNIT=6)
CLOSE (UNIT=7)
CLOSE (UNIT=8)
END

```

\*\*\*\*\*

- \* This subroutine reads in reflection coefficients for a particle velocity from input data file#1, then
- \* reverses the polarity to coincide with the seismic field trace polarity

```

SUBROUTINE INPUT1(LC,C,CR)
DIMENSION C(LC), CR(LC)
DO 1 K=1,LC
READ(1,*) JJ,C(K)
CR(K)=-C(K)
1 CONTINUE
RETURN
END

```

\*\*\*\*\*

- \* This subroutine reads in source wavelet from input data file#2

```

SUBROUTINE WAVELET(LS,S)
DIMENSION S(LS)
DO 2 I=1,LS
READ(2,*) K, S(I)
2 CONTINUE
RETURN
END

```

\*\*\*\*\*

- \* This subroutine Calculates the earth's impulse response

```

SUBROUTINE POLYCz(M,GZ,N,FZ,L,Cz)
DIMENSION GZ(M), FZ(N), Cz(L)
INTEGER S
CALL ZERO(L,Cz)
CALL MOVE(MIN0(M,L),GZ,Cz)
DO 3 I=1,L
Cz(I)=Cz(I)/FZ(1)
IF(I.EQ.L) RETURN
K=I
S=MIN0(N-1,L-I)
DO 3 J=1,S
K=K+1
Cz(K)=Cz(K)-Cz(I)*FZ(J+1)
3 CONTINUE
RETURN
END

```

\*\*\*\*\*

- \* This subroutine Calculates the scaping waves response

```

SUBROUTINE POLYTz(R,POWTC,N,FZ,L,Tz)
DIMENSION FZ(N), Tz(L), POWTC(R)
INTEGER S, R
CALL ZERO(L,Tz)
CALL MOVE(MIN0(R,L),POWTC,Tz)
Tz(1)=POWTC(R)
DO 4 I=1,L
Tz(I)=Tz(I)/FZ(1)
IF(I.EQ.L) RETURN
K=I
S=MIN0(N-1,L-I)
DO 4 J=1,S
K=K+1
Tz(K)=Tz(K)-Tz(I)*FZ(J+1)

```

```

4 CONTINUE
  RETURN
  END
*****
*   This subroutine moves array elements from one location to different storage location
SUBROUTINE MOVE(LX,X,Y)
  DIMENSION X(LX), Y(LX)
  INTEGER LX
  DO 5 I=1,LX
    Y(I)=X(I)
5 CONTINUE
  RETURN
  END
*****
*   This subroutine performs the convolution of the reflection coefficient series with the source
*   wavelet
SUBROUTINE CONVOL1(LC,CR,LW,W,K,X)
  DIMENSION CR(LC), W(LW), X(K)
  CALL ZERO(K,X)
  DO 6 I=1,LC
    DO 6 J=1,LW
      K=I+J-1
      X(K)=X(K)+CR(I)*W(J)
6 CONTINUE
  RETURN
  END
*****
*   This subroutine performs the convolution of the modified (transmission losses included) reflection
*   coefficients with the source wavelet
SUBROUTINE CONVOL2(LC,CT,LW,W,K,X)
  DIMENSION CT(LC), W(LW), X(K)
  CALL ZERO(K,X)
  DO 7 I=1,LC
    DO 7 J=1,LW
      K=I+J-1
      X(K)=X(K)+CT(I)*W(J)
7 CONTINUE
  RETURN
  END
*****
*   This subroutine performs the convolution of earth's impulse response with the source wavelet
SUBROUTINE CONVOL3(LC,E,LW,W,K,X)
  DIMENSION E(LC), W(LW), X(K)
  CALL ZERO(K,X)
  DO 8 I=1,LC
    DO 8 J=1,LW
      K=I+J-1
      X(K)=X(K)+E(I)*W(J)
8 CONTINUE
  RETURN
  END
*****
*   This subroutine performs the convolution of the earth's one-way transmission response with the
*   source wavelet
SUBROUTINE CONVOL4(LC,T,LS,S,K,XT)
  DIMENSION T(LC), S(LS), XT(K)
  CALL ZERO(K,XT)
  DO 9 I=1,LC
    DO 9 J=1,LS

```

```
    K=I+J-1
    XT(K)=XT(K)+T(I)*S(J)
9 CONTINUE
    RETURN
    END
```

\*\*\*\*\*

\* This subroutine sets to zero all initial values in array

```
SUBROUTINE ZERO(LZ,Z)
DIMENSION Z(LZ)
INTEGER LZ
IF(LZ.LE.0) RETURN
DO 10 I=1,LZ
  Z(I)=0.0
10 CONTINUE
    RETURN
    END
```

\*\*\*\*\*

\* Input data file#1 "refl.dat" format

```
* JJ C(1)
* .. ..
* .. ..
* JJ C(LC)
```

\* -----

\* Input data file#2 "wavelet" format

```
* time S(1)
* ... ..
* ... ..
* time S(LS)
```

\*\*\*\*\*

## A2 Complete synthetic with free-surface program

```
PROGRAM ROBINSON
*****
** This program has been adapted from Robinson (1983). Program to calculate synthetic seismogram
** from reflection coefficients with free-surface is taken into account.
**
-----
** C = reflection coefficient for a particle velocity
** LC = total number of interfaces less one (free-surface with C=-1) is already included in the
** program
** Cz = earth's impulse response for LC interfaces
** A = prediction error operator
** V = variance curve
** S = input seismic source wavelet of length LS samples
** X = complete synthetic seismogram with LX samples
** CX = complete synthetic seismogram with polarity reversed in order to coincide with the real data
** SI = sampling interval in ms
** JJ = two-way travel time in ms
*****
DIMENSION C(1194), Cz(1194), A(1194), AP(1194), V(1194)
DIMENSION S(73), X(1267), CX(1267)
INTEGER LC, JJ, SI

PRINT*, 'INPUT LC'
READ*, LC
PRINT*, 'INPUT LS'
READ*, LS
OPEN(UNIT=1, FILE='refl2.dat', STATUS='OLD')
OPEN(UNIT=2, FILE='wavelet', STATUS='OLD')
OPEN(UNIT=3, FILE='A2 output1')

* First interface is the free-surface with C=-1.0
LB=((LS-1)/2)+1
LX=LC+LS-1
LD=LX-LB+1
SI=2

CALL INPUT1(LC,C)

* Calculate earth's impulse response with free-surface included
Cz(1)=C(1)
A(1)=-C(1)
V(1)=1.0-C(1)*C(1)
DO 20 I=2, LC
Cz(I)=C(I)*V(I-1)
DO 30 J=1, I-1
Cz(I)=Cz(I)-A(J)*Cz(I-J)
AP(J)=A(J)-C(I)*A(I-J)
30 CONTINUE
DO 40 J=1, I-1
A(J)=AP(J)
40 CONTINUE
A(I)=-C(I)
V(I)=V(I-1)*(1.0-C(I)*C(I))
20 CONTINUE

CALL WAVELET(LS,S)
```

```
CALL CONVOL(LC,Cz,LS,S,LX,X)
```

```
* Output complete synthetic seismogram with the same polarity as the real seismic data  
WRITE(3,5)
```

```
5 FORMAT('Complete synthetic seismogram')
```

```
  JJ=0
```

```
  CX(1)=0.0
```

```
  WRITE(3,15) JJ, CX(1)
```

```
  DO 50 I=LB,LD
```

```
  JJ=(I-LB+1)*SI
```

```
  CX(I)=-X(I)
```

```
  WRITE(3,15) JJ, CX(I)
```

```
15 FORMAT(1X,I5,2X,F9.5)
```

```
50 CONTINUE
```

```
  CLOSE (UNIT=1)
```

```
  CLOSE (UNIT=2)
```

```
  CLOSE (UNIT=3)
```

```
  END
```

```
*****
```

```
* This subroutine reads in reflection coefficients for particle velocity from input data file#1
```

```
  SUBROUTINE INPUT1(LC,C)
```

```
  DIMENSION C(LC)
```

```
  DO 1 I=1,LC
```

```
  READ(1,*) JJ, C(I)
```

```
1 CONTINUE
```

```
  RETURN
```

```
  END
```

```
*****
```

```
* This subroutine reads in source wavelet from input data file#2
```

```
  SUBROUTINE WAVELET(LS,S)
```

```
  DIMENSION S(LS)
```

```
  DO 2 I=1,LS
```

```
  READ(2,*) K, S(I)
```

```
2 CONTINUE
```

```
  RETURN
```

```
  END
```

```
*****
```

```
* This subroutine performs the convolution of the earth's impulse response with the source wavelet
```

```
  SUBROUTINE CONVOL(LE,E,LW,W,K,X)
```

```
  DIMENSION E(LE), W(LW), X(K)
```

```
  CALL ZERO (K,X)
```

```
  DO 3 I=1,LE
```

```
  DO 3 J=1,LW
```

```
  K=I+J-1
```

```
  X(K)=X(K)+E(I)*W(J)
```

```
3 CONTINUE
```

```
  RETURN
```

```
  END
```

```
*****
```

```
* This subroutine sets to zero all initial values in array
```

```
  SUBROUTINE ZERO(LZ,Z)
```

```
  DIMENSION Z(LZ)
```

```
  IF(LX.LE.0) RETURN
```

```
  DO 4 I=1,LZ
```

```
  Z(I)=0.0
```

```
4 CONTINUE
```

```
  RETURN
```

END

\*\*\*\*\*

\* Input data file#1 "refl2.dat" format

\* JJ C(2)

\* .. ..

\* .. ..

\* .. ..

\* JJ C(LC)

\* -----

\* Input data file#2 "wavelet" format

\* time S(1)

\* ... ..

\* ... ..

\* ... ..

\* time S(LS)

\*\*\*\*\*

### A3 Binary file program

```
PROGRAM BINARY
*****
* This program converts data in ASCII format into an unformatted binary file.
*-----
  DIMENSION X(1095)

  PRINT*, 'NUMBER OF INPUT SAMPLES'
  READ*, LC

* INPUT_FILE = SYNTHETIC SEISMOGRAM DATA
* OUTPUT_FILE = BINARY FILE

  OPEN(UNIT=1, FILE='INPUT-FILE NAME', STATUS='OLD')
  OPEN(UNIT=2, FILE='OUTPUT-FILE NAME', ACCESS='DIRECT', RECL=4*LC)
  DO 10 I=1, LC
  READ(1, *) JJ, X(I)
10 CONTINUE

* output (repeat) the same synthetic trace ten times
  DO 30 J=1, 10
  WRITE(2, REC=J) (X(I), I=1, LC)
30 CONTINUE

  CLOSE(UNIT=1)
  CLOSE(UNIT=2)
  END
*****

* Input data file format

* JJ X(1)
* .. ..
* .. ..
* JJ X(LC)
*****
```

---

### A4 SEG-Y format program

```
*****

#!/bin/sh
# This program adds header information to the unformatted binary file to convert the binary data into
# SEG -Y format data, readable by ProMAX. It is a SEISMIC UNIX program.
#
# INPUT_FILE = BINARY FILE
# OUTPUT_FILE = SEG-Y FORMAT FILE
data=path name/INPUT-FILE NAME
suaddhead < $data ftn=0 ns=$1 > data.su
segyhdrs < data.su
segfwrite tape=OUTPUT-FILE NAME trmin=1 trmax=10 < data.su
```

## A5 Fourier transform program

### PROGRAM FOURIER

\*\*\*\*\*

\*\* This program performs the forward (amplitude spectrum only) and the inverse Fourier analysis for  
 \*\* a given time sequence of  $2^m$  samples, where m is an integer.

-----

\*\* D = input time series of  $2^m$  samples  
 \*\* F = frequency in Hz  
 \*\* DF = frequency discretization  
 \*\* AMP = amplitude  
 \*\* JJ = two-way travel time in ms  
 \*\* DT = sampling interval in seconds  
 \*\* TS = inverse Fourier transform results, by definition, this result should be exactly identical to  
 \*\* the input time series.  
 \*\* FN = nyquist frequency  
 \*\* N = total number of samples

\*\*\*\*\*

DIMENSION AMP(3000)  
 COMPLEX X(3000), Y(3000), TS(3000)  
 REAL A, F, D, JJ

PRINT\*, 'TOTAL No. OF SAMPLES'  
 READ\*, N  
 PRINT\*, 'SAMPLING INTERVAL IN SECONDS'  
 READ\*, DT

OPEN(UNIT=1, FILE='INPUT-FILE', STATUS='OLD')  
 OPEN(UNIT=2, FILE='A5 output1')  
 OPEN(UNIT=3, FILE='A5 output2')  
 OPEN(UNIT=4, FILE='A5 output3')

P=3.141592654  
 DF=1.0/(N\*DT)  
 SI=DT\*1000.0  
 FN=1.0/(2.0\*DT)

\*\*\*\*\*

DO 10 I=1,N  
 READ(1,\*) JJ, D  
 X(I)=CMPLX(D)  
 10CONTINUE

CALL FFT(X,N,P,DF,FN,Y)  
 CALL IFT(Y,N,P,SI)

CLOSE(UNIT=1)  
 CLOSE(UNIT=2)  
 CLOSE(UNIT=3)  
 END

\*\*\*\*\*

\* This subroutine calculates the Forward Fourier transform

SUBROUTINE FFT(X,N,P,DF,FN,Y)  
 DIMENSION AMP(3000)  
 COMPLEX B,G,R(3000),X(3000),Y(3000)

F=0.0

```

DO 30 J=1,N
K=J-1
B=CMPLX(0.0,0.0)
DO 40 I=1,N
M=I-1
A=2.0*P*K*M/N
G=CMPLX(COS(A),-1*SIN(A))
R(I)=X(I)*G
B=B+R(I)
40CONTINUE
Y(J)=B
AMP(J)=ABS(B)
WRITE(2,15) F,AMP(J)
IF(F.EQ.0.OR.F.EQ.FN) GO TO 50
IF(F.GT.FN) STOP
AMP(J)=AMP(J)*2.0
50WRITE(3,15) F, AMP(J)
15FORMAT(3X,F7.3,5X,F9.5)
F=F+DF
CONTINUE
RETURN
END

```

\*\*\*\*\*

\* This subroutine calculates the inverse Fourier transform,. It is used here just as a numerical  
\* checkup.

```

SUBROUTINE IFT(Y,N,P,SI)
DIMENSION TS(3000)
COMPLEX U,G(3000),Y(3000)

```

```

JJ=0.0
DO 60 J=1,N
K=J-1
U=CMPLX(0.0,0.0)
DO 70 I=1,N
M=I-1
A=2.0*P*K*M/N
G(I)=CMPLX(COS(A),SIN(A))
U=U+(1.0/N)*Y(I)*G(I)
70CONTINUE
TS(J)=REAL(U)
WRITE(4,25) JJ, TS(J)
25FORMAT(2X,F7.2,5X,F8.4)
JJ=JJ+SI
60CONTINUE
RETURN
END

```

\*\*\*\*\*

\* Input data file format

```

* JJ D(1)
* .. ..
* .. ..
* JJ D(N)

```

\*\*\*\*\*



